

**Human TATA-Binding Protein Interactions with DNA
Characterized by Stabilized, Axial Optical Trapping**

by

Amanda E. Carpenter

B.S., Louisiana Tech University, 2002

M.S., University of Colorado, 2007

A thesis submitted to the
Faculty of the Graduate School of the
University of Colorado in partial fulfillment
of the requirements for the degree of
Doctor of Philosophy
Department of Physics

2011

This thesis entitled:
Human TATA-Binding Protein Interactions with DNA Characterized by Stabilized, Axial
Optical Trapping
written by Amanda E. Carpenter
has been approved for the Department of Physics

Thomas Perkins

John Cumalat

Date _____

The final copy of this thesis has been examined by the signatories, and we find that both the content and the form meet acceptable presentation standards of scholarly work in the above mentioned discipline.

Carpenter, Amanda E. (Ph.D., Physics)

Human TATA-Binding Protein Interactions with DNA Characterized by Stabilized, Axial
Optical Trapping

Thesis directed by Professor Thomas Perkins

TATA-Binding Protein (TBP) binding to DNA is a critical step in gene expression. In the first step of gene expression, transcription of RNA from DNA, TBP binds DNA and recruits the transcription machinery. TBP binds DNA at a preferred sequence called the TATA box and bends the DNA at $\sim 100^\circ$. In this work we characterized TBP dynamically bending DNA at the single-molecule level using an actively stabilized, axial optical trap.

To perform this characterization, several challenges led us to develop a customized biophysical assay. Nonspecific interactions of TBP with sample surfaces required coating surfaces with polyethylene glycol. A small predicted signal size (~ 5 nm) and slow kinetics ($\sim 10^{-2}$ s $^{-1}$) demanded high stability in our optical trap assay, leading us to implement an actively stabilized instrument. An apparent affinity by TBP for non-TATA box DNA sequences led us to use very short DNA molecules (92 nm) with carefully controlled sequences. This short length of DNA demanded the development of a novel axial trapping and detection technique, which also has the advantage of improved spatiotemporal resolution (integrated noise < 1 nm over 100 s at 0.5 pN, 5 fN/nm trap stiffness, $\Delta f = 0.03$ -3.2 Hz). Our final assay involved custom surface-chemistry, an actively stabilized optical trap, short DNA with carefully engineered sequences, and a novel axial detection method.

Using this novel assay, we measured TBP and TATA-box dependent extension changes of DNA at the single-molecule level. Under optimized conditions (short, carefully chosen DNA; optimized [TBP], [MgCl₂] and [KCl]), we obtained step-wise, consistently-sized TBP-dependent extension changes. By hidden Markov modeling analysis, we quantified the extension changes and rates for bending and unbending, and we performed simulations to verify

our analysis methods. We applied three different forces (0.3, 0.5 and 0.8 pN) to test the affect of force on the extension change and rates. We found a constant extension change of 3 nm, with dynamics on the scale of tens of seconds. The developed assay directly measures dynamic bending of DNA by TBP, and the techniques developed here have potential to be broadly useful for high-spatiotemporal resolution studies of many other DNA-protein interactions.

Dedication

To my Marty, my Mom, and my Dad.

Acknowledgements

To my teachers, colleagues, friends, and family members, thank you for the inspiration and support that made completion of this work possible.

A big thank you to my advisor, Tom Perkins, the source of endless knowledge and ideas. Thank you for your support, for always ensuring that we learn something, and for caring that we get things right.

Thank you to the amazing Perkins Lab postdocs: Lora Nugent-Glandorf, Yeonee Seol, Hern Paik, and Gavin King. Lora got me started in everything from optics to hands-on biochemistry to LabVIEW programming. Yeonee was a major player in building, troubleshooting, and maintaining our instrument, development of the axial detection technique, and biochemical-assay development for the Perkins lab. Gavin was always an inspiration and a cheerleader for me and for science. Hern lent me his expertise for everything from surface chemistry to instrumental trouble-shooting and was an excellent role model for being a logical, analytical experimentalist.

Thank you to the past and present Perkins Lab graduate students: Ashley Carter, Martha Hosotani, Justin Kuczynski, and Allison Churnside. Ashley learned the ropes of biophysics and Ph.D. research with me, sharing countless hours on everything from homework sets to Tuesday night learning sessions with Tom, from training me on optics to letting me train her on biochemistry, and from hearty arguments about science to celebrations of successes. Martha Hosotani, generous, with a creative, analytical mind, was an amazing listener who always asked the hard questions that made me think and helped me in countless

tangible and intangible ways. Justin provided many ideas and much needed energy during a frustrating phase of the project, and Allison was a resource of support and positivity.

Thank you to Wayne Halsey, biochemistry guru. I am eternally grateful for your expertise, for all the DNA that was essential for my project, and for everything that kept our lab running smoothly.

Thank you to other students I've had the pleasure of working with in the Perkins Lab: Betsy Siewert, Tara Turner, Theresa Ulrich, Nicole Kennerly, Jenni Adams, Andy Leifer, Joseph D'Silva, and Jessica Rouge. Special thanks to George Emanuel, who converted the drift-correcting hidden Markov modeling into a user-friendly Igor format.

Thank you to my collaborators: Jim Goodrich, Meredith Betterton, Aaron Hieb, Jinyu Li and Tatiana Kuriabova. Jim and Aaron provided proteins, plasmids, and transcription expertise; and I'm also grateful for help from Jennifer Kugel, Linda Drullinger and Benjamin Gilman in the Goodrich lab. Meredith, Jinyu, and Tatiana provided modeling and theoretical analysis and expertise. Jim and Meredith were not only collaborators, but served as scientific mentors as well.

Thank you to the amazing technical support staff at JILA. Thank you to Hans Green, Blaine Horner, Kim Hagen, Tracey Keep, and Tom Foote, all who had a hand in custom machining of parts for the stabilized optical-trapping instrument; and thank you to David Alchenberger who provided essential training on Keck lab instruments. Thank you to Jan Hall, Terry Brown, Carl Sauer, Mike Whitmore, and Dave Tegart, who each played a role in custom electronics design and development. Thank you to the JILA Computing staff, especially Jim McKown, Mike Page, J.R. Raith and Pete Ruprecht, who kept my computers running smoothly and saved me countless hours of frustration with their tips, tricks, and miscellaneous computer help.

Thank you to the administrative staff at JILA. Special thanks to Agnieszka Lynch, Maryly Dole, Julie Phillips, Brian Lynch, Jeff Sauter, Randall Holliness and past member Ed Holliness for many positive interactions and making JILA a great place to work.

Thank you to my defense committee: Tom Perkins, Jim Goodrich, Matt Glaser, John Cumalat, and Margaret Murnane, for your time and especially for excellent questions and feedback that are guaranteed to improve the quality of our publication on this project. Special thanks to the final readers, Tom Perkins and John Cumalat, for your extra time and for your comments on the text.

I'm grateful for the funding for my work, provided by the NIH Biophysics Training Grant and by multiple other grants through my advisor, Tom Perkins.

Thank you to many teachers along the way. To my undergraduate advisor at Louisiana Tech, Lee Sawyer, thank you for all the time, effort, and heart you put into preparing me and all of your students. Also at Louisiana Tech, thank you to the professors who taught me the essentials: Lee Sawyer, Ramu Ramachandran, Zeno Greenwood, Steve Wells, Natalia Zotov, Neven Simicevic, and John K. Price. At CERN, thank you to my group leader Thomas Meyer and to my advisor/mentor Joachim Baechler for encouragement and for providing an amazing research experience. And thank you to excellent teachers from earlier years: Ms. Gore, Ms. Stocker, Ms. Stanescu, Mr. Gamble, Coach Way and Ms. Mosteller.

Thank you to my friends, not only for providing the support that was so needed to complete my research and thesis, but also for making sure I had fun during the process. Thank you to Colleen Crego, Sara Bellinger Rylander, Allison Fox Swain, Holly Wilkins Johnson, Kathryn Goode McCarty, and Jenny Walling Neville: friends from long before grad school. Thank you to all my Boulder friends, especially Juan Pino, Kirk Ullmann, Zach Walters, Keith and Allison Ulmer, Chris and Carly Keller, John Obrecht, Ashley Carter, Christine Davidson Frank, Erin White, Juli Baumblatt, Sebastian Blatt and Irina, Martha Hosotani, Stephanie Meyer, Lora Nugent-Glandorf, Julie Fiore, and Haemi Lee. Thank you to the Ye Lab, especially the strontium group, for lunch breaks, good conversation, and sharing Marty with me. An extra special thank you to Katarina Cicak and Kevin Moll for giving me not just housing, but an actual home with all the emotional support a true home entails. And another extra special thank you to the friends who took such good care of me

for that last year in Boulder: Martha, Julie, Stephanie, Lora and Haemi. Thank you for being such good friends. Thank you also to my newest California-made friends, especially Stacey Booth, Mike Matthews, and Kristin Zumwalt. You kept me sane, kept me from being completely swallowed by my thesis, and helped keep some non-thesis related fun in my life during this last year.

To my family, thank you for providing the love, perspective, balance, stability, advice, countless hours listening, and understanding that allowed me to successfully undertake this endeavor. You gave me inspiration and motivation when I didn't think I could possibly find any more. Thank you to my mom for talking with me almost every day, always listening sympathetically, and providing encouragement that kept me motivated and grounded. Thank you also to my mom for passing on an analytical bent and penchant for being precise that have served me well in science. Thank you to my dad for compassion and guidance, and for instilling in me a need to question everything and a desire to understand the way things work, two more qualities that have served me well. Thank you to my brothers and my sister, Scott, Matt, and Sarah, and to my siblings' significant others, Robin and Craig. You keep my world wide, help me talk things through, and set examples that always make me strive to be a better person. Thank you to the Boyds and the Boyles, especially Marilyn, Joe, Nancy, Kate, and Scott, and especially for taking excellent care of me and being understanding and encouraging while I worked through this entire past Thanksgiving. Thank you to my Grams, my Grandma Bo, and my extended family for providing encouragement and an extended network of support.

And finally, thank you to Martin M. Boyd. Brilliant, big-hearted and always able to make me laugh. Thank you for being my solid ground, for always believing in me, and for making all burdens bearable. You're the world's best teammate, and I'm so glad your mine.

Contents

Chapter	
1	INTRODUCTION 1
1.1	AN INTRODUCTION TO GENE EXPRESSION 1
1.1.1	Transcription and regulation 2
1.1.2	TBP and the TATA box 4
1.1.3	Architecture of the transcription preinitiation complex 5
1.2	OPTICAL TRAPPING AND SINGLE MOLECULE TECHNIQUES 6
1.3	THESIS OVERVIEW 7
2	EXPERIMENTAL TECHNIQUE 9
2.1	COMPONENTS OF THE INSTRUMENT 10
2.1.1	Lasers for trapping and detection 13
2.1.2	Acousto-optic modulators (AOMs) for intensity control 16
2.1.3	Optical fibers for beam refinement and pointing stability 17
2.1.4	Samplers and photodiodes for intensity stabilization 17
2.1.5	PZT mirrors for beam steering 18
2.1.6	Dichroics for light integration and separation 18
2.1.7	Microscope for optical trapping 20
2.1.8	Piezo stage for sample control 21
2.1.9	Detectors and electronics for visualization and detection 21

2.1.10	Components for passive stabilization	21
2.2	INTENSITY STABILIZATION	23
2.2.1	Nonlinearity of servo response	23
2.2.2	Optimization of fiber coupling at the ideal AOM setting	24
2.2.3	Optimization of servo electronics	26
2.2.4	Optimization for stability and dynamic range of the trapping laser	26
2.3	SAMPLE STABILIZATION	31
2.4	ALIGNMENT, CALIBRATIONS AND CHARACTERIZATION OF THE INSTRUMENT	31
2.4.1	Alignment into the microscope	32
2.4.2	1st-order focal-plane alignment: Aligning laser foci with imaging plane	33
2.4.3	Alignment of QPD axes with stage axes	33
2.4.4	Centering beads and beams	34
2.4.5	Axial alignment by minimizing crosstalk	34
2.4.6	2nd-order focal-plane alignment: Aligning axial detection signals	36
2.4.7	Minimizing trap degradation with depth by eliminating slope of axial voltage oscillations	36
2.4.8	PZT-mirror calibrations	40
2.4.9	Detection sensitivity calibrations	43
2.4.10	Drag measurement	45
2.4.11	Trap symmetry and ellipticity	45
2.4.12	Axial alignment by sensitivity offset vs. height	48
2.4.13	3rd-order focal-plane alignment: Optimizing xy-sensitivity vs. height	48
2.4.14	Laser power measurements	50
2.4.15	Trap stiffness calibrations	52
2.4.16	Stability characterizations	53
2.4.17	Force vs. extension for DNA	56

2.5	SAMPLE PREPARATION	60
2.5.1	Cleaning coverslips and slides	60
2.5.2	Flow cells	61
2.5.3	Antidigoxegenin modification of beads	61
2.5.4	Stuck beads	62
2.5.5	PEG-modification of surfaces	63
2.5.6	DNA-tethering beads to surfaces	65
2.5.7	TBP handling	67
2.6	DATA ACQUISITION	67
2.6.1	Computer, controllers, drivers, and electronics	68
2.6.2	Centering lasers and beads	68
2.6.3	Setting height	69
2.6.4	Detection sensitivity calibrations	69
2.6.5	Measuring trap stiffness and force	69
2.6.6	Centering over DNA tetherpoint	70
2.6.7	TBP and control tether data acquisition: DNA extension vs. time	70
2.7	DATA ANALYSIS	72
2.7.1	PZT calibrations	73
2.7.2	Force vs. extension	73
2.7.3	Stability/noise calculations	73
2.7.4	Simulation: Bead in an optical trap	74
2.7.5	Calculation of axial bead position probability distribution	75
2.7.6	Hidden-Markov modeling analysis of TBP data	82
2.7.7	Simulation: TBP data	82
3	AXIAL CALIBRATION AND DETECTION	83
3.1	INTRODUCTION	83

3.1.1	Geometry constraints in traditional optical trapping	84
3.1.2	Advantages of axial trapping and detection	86
3.1.3	Axial detection in the literature	87
3.1.4	Overview of our technique	89
3.1.5	A conceptual description of axial trapping and detection	90
3.2	MATERIALS AND METHODS	92
3.3	AXIAL CALIBRATIONS	94
3.3.1	Calibration of relative axial displacement	94
3.3.2	Determination of axial trap equilibrium	97
3.3.3	Voltage oscillation corrections	100
3.3.4	Calibration of height above the surface	102
3.3.5	Calibration of axial stiffness	106
3.4	UNCERTAINTY ESTIMATES OF CALIBRATION	114
3.4.1	Uncertainty by measurements on beads fixed to the surface	114
3.4.2	Uncertainty by trapped bead deviations from equilibrium	119
3.4.3	Uncertainty by trap stiffness measurements	120
3.4.4	Uncertainty by DNA force and extension	121
3.5	IMPROVED AXIAL FORCE AND EXTENSION ESTIMATIONS	124
3.5.1	Estimating force from data traces	124
3.5.2	Force estimation by equipartition	126
3.5.3	Force estimation by power spectral density	129
3.5.4	Force estimation by autocorrelation	132
3.5.5	Summary of final force estimates	132
3.6	DECREASED NOISE ON SHORT DNA TETHERS	134
3.7	CONCLUSIONS	135

4	DIRECT MEASUREMENT OF HUMAN TBP BENDING DNA	137
4.1	INTRODUCTION	137
4.2	MATERIALS AND METHODS	139
4.3	TBP AND TATA-DEPENDENT EXTENSION CHANGES IN DNA	142
4.3.1	Data reduction	143
4.4	EXTENSION CHANGES VS FORCE	148
4.5	KINETICS	149
4.6	SIMULATIONS TO VALIDATE ANALYSIS	154
4.7	DRIFT CORRECTING HIDDEN MARKOV ANALYSIS	154
4.8	CONCLUSIONS	157
5	CONCLUSIONS AND FUTURE DIRECTIONS	159
5.1	CONCLUSIONS	159
5.2	FUTURE DIRECTIONS	160
5.2.1	Technique and instrumentation improvements	160
5.2.2	Exploring TBP-induced spikes in DNA extension	161
5.2.3	Angle vs. stability changes for bending of non-consensus TATA boxes	162
5.2.4	Geometry and stability changes with additional PIC proteins	163
	Bibliography	165

Tables

Table

2.1	Detection electronics settings	22
2.2	Intensity servo settings	26
2.3	Laser settings	32
2.4	Typical detector readings without servos	50
2.5	Typical detector readings and laser power with servos	51
2.6	Trapped bead simulation values	74
3.1	Uncertainty estimates of axial calibration	115
3.2	Force vs. extension errors from calibration uncertainties	122
3.3	Force estimation from data	134
3.4	Final force and extension estimates	134
4.1	Transition rates from HMM transition probabilities	153
4.2	Transition rates from dwell time fits	154
4.3	TBP trace simulations	157

Figures

Figure

1.1	Transcription preinitiation complex	3
1.2	Crystal structure of TBP and TATA DNA	5
2.1	Pre-fiber instrument setup diagram	11
2.2	Post-fiber instrument setup diagram	12
2.3	Beam profile	14
2.4	PZT mirror beam steering diagram	19
2.5	Photodiode voltage vs. AOM voltage	25
2.6	Intensity noise of 810 and 850	27
2.7	Intensity noise of 1064	29
2.8	Trap intensity stabilization	30
2.9	x, y scans	35
2.10	z scans with x, y crosstalk	37
2.11	Axial scans to show relative z	38
2.12	Axial scan of a trapped bead	39
2.13	PZT mirror calibration	41
2.14	Verification of PZT mirror calibration	42
2.15	Detection sensitivity of a trapped bead	44
2.16	Drag-force measurement	46

2.17	Trap ellipticity	47
2.18	Sensitivity vs. z	49
2.19	Stiffness calibration	54
2.20	Verification of stiffness calibration	55
2.21	Stability of stuck beads - 1 bead	57
2.22	Stability of stuck beads - 2 beads	58
2.23	DNA force vs. extension	59
2.24	Final assay	71
2.25	Process for simulating trapped bead position traces	76
2.26	Simulation of a trapped bead axial position trace	77
2.27	Theoretical calculation of axial bead position probability distribution	81
3.1	Diagonal vs. axial geometry	84
3.2	Axial intensity signal	90
3.3	Axial detection displacement calibration	95
3.4	Referencing from peak	99
3.5	Correcting for oscillations	101
3.6	Determining trap height relative to the coverslip surface	103
3.7	Peak adjustments	105
3.8	z position vs. x position of a trapped bead	107
3.9	Histograms of trapped bead positions	108
3.10	Histograms of trapped bead positions vs. height	109
3.11	EQP asymmetry vs. height	110
3.12	Axial power spectral densities	112
3.13	Axial trap stiffness calibrations	113
3.14	Accuracy of calibrated axial measurements	116
3.15	Accuracy of calibrated axial measurements for fiducial	118

3.16	Force vs. extension, measured in the axial direction	123
3.17	Three methods for estimating force	125
3.18	Simulation of three methods for estimating force	127
3.19	Histograms of axial bead position	128
3.20	DNA stiffness vs. extension	130
3.21	Power spectral density of highest force data and simulation	131
3.22	Autocorrelation of axial bead position traces	133
3.23	Stability with 92 nm tethers	135
4.1	Final TBP assay	138
4.2	TBP and TATA dependent extension changes in DNA	145
4.3	Common events in DNA extension vs. time traces	146
4.4	Extension changes show long and short dwell times	150
4.5	Exploring force dependence	150
4.6	Histograms of extension changes for three forces	151
4.7	Force vs. extension change, theory and experiment	152
4.8	Transition rates calculated from transition probabilities	153
4.9	Dwell time histograms for three forces	155
4.10	Simulations to verify analysis methods	156
4.11	Drift correcting hidden Markov modeling analysis	158

Chapter 1

INTRODUCTION

1.1 AN INTRODUCTION TO GENE EXPRESSION

The flow of genetic information - from DNA to RNA to proteins - governs biology at the most fundamental, molecular level. DNA contains plans, code, blueprints: the genetic information that directs growth, development, response to environmental stimuli, and disease. This genetic information is encoded in DNA in the form of genes - sequences in DNA that encode for proteins, with RNA as an intermediary. Proteins, the end result of gene expression, are the work horses of molecular biology.

Genetic information is encoded in both DNA and RNA in the sequences of the four bases that compose their structure. The four bases that make up DNA are adenine, cytosine, guanine, and thymine, abbreviated A, C, G, and T respectively. The same four bases make up RNA, except instead of thymine, RNA contains uracil, abbreviated U. In DNA and RNA structure, each of these bases is attached to a sugar-phosphate (deoxyribose in DNA, ribose in RNA). These base-sugar-phosphate subunits assemble linearly to form the structure of a DNA or RNA strand. The sugar-phosphates form the backbone of the molecule; the sequence of the bases encodes the genetic information.

Genetic information is passed from DNA to RNA by pairing of the bases that compose the DNA and RNA structure. The bases pair specifically: A pairs with T (or U); C pairs with G. It is through this base pairing that DNA forms its typical double-stranded structure; the sequence in one strand is complementary (an A for every T, a C for every G, and vice

versa) to the sequence in the other strand. It is also through this base pairing that DNA transfers genetic information to RNA. RNA is synthesized with a complementary sequence to the DNA template sequence. The process of RNA synthesis from a DNA template is called transcription, and is carried out by proteins called RNA polymerases. RNA polymerase is assisted in transcription by other transcription machinery proteins, varying by organism and function, discussed in detail below.

The RNA synthesized in transcription encodes for a specific protein by encoding for a specific series of amino acids. Amino acids string together linearly to form the primary structure of proteins. Different proteins are made up of different combinations of 20 different amino acids. Each of these 20 amino acids is encoded by a different 3 base sequence in RNA. This protein synthesis process, the transfer of genetic information from RNA to proteins, is called translation.

The translated proteins go on to perform functions as diverse as life itself. As a quick sampling of protein functions, proteins catalyze reactions, metabolize energy sources, form signalling pathways. Proteins carry cellular cargo, form and move muscles, carry out cellular reproduction and repair. Bringing the process of gene expression full circle, proteins regulate transcription and form the transcription machinery responsible for expressing the genetic information encoded in DNA.

1.1.1 Transcription and regulation

Human gene expression is intricate, complex and highly regulated. The human genome contains ~ 3 billion base pairs of DNA, with $\sim 40,000$ genes [1]. Genes must be differentially expressed in different cell types, during different phases of development, and in response to different stimuli. Appropriate gene expression from this exquisitely complex genome is accomplished in large part by regulation of transcription.

In humans and other eukaryotes, site specific transcription of genes in DNA to the messenger RNA that codes for proteins is carried out by RNA polymerase II (pol II) plus

several general transcription factors (GTFs), including TATA binding protein, TBP, the protein subject of this thesis. To initiate gene expression, transcription must be initiated at the start-site for a gene, i.e. a promoter, a sequence in DNA that signals a start site for transcription of a gene. Selection of these start sites is where TBP plays a crucial role.

RNA pol II, the polymerase responsible for the physical synthesis of RNA from DNA, lacks the sequence specificity necessary to recognize promoters [2]. Therefore to transcribe genes in a site-specific manner, accessory proteins are critical for recognizing the appropriate transcription start sites. The GTFs fulfill this critical role by recognizing promoter sequences in DNA and recruiting pol II to specific start sites.

The GTFs involved in transcription by pol II are made up of several transcription factors (TFs): TFIIA, TFIIB, TFIID, TFIIE, TFIIIF, and TFIIH. Thomas and Chiang provide an excellent review of each of these GTFs [2]. These GTFs plus pol II form the transcription preinitiation complex (PIC), shown in Fig. 1.1, which initiates transcription at promoter DNA sequences.

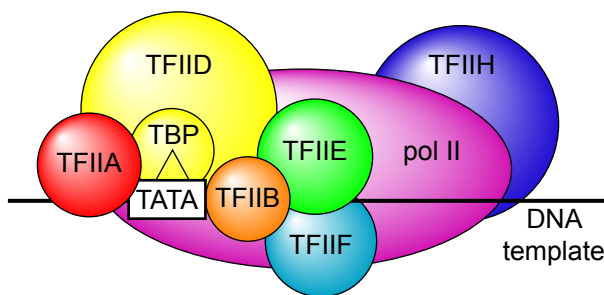


Figure 1.1: The transcription preinitiation complex (PIC), made up of RNA pol II and the general transcription factors TFIIA, TFIIB, TFIID, TFIIE, TFIIIF, and TFIIH is shown bound to promoter DNA. TBP, a subunit of TFIID, is shown bound to the TATA box sequence on the DNA.

1.1.2 TBP and the TATA box

Promoter sequences that are required for functional PIC formation are known as core promoter elements; at least 7 core promoter elements have been identified in eukaryotes [2]. The TATA box is 1 of these 7 core promoter elements. It has a consensus sequence TATA(A/T)A(A/T)(A/G) and is recognized by TATA-binding protein, TBP, a subunit of the GTF TFIID. Of the remaining 6 core promoter elements, 2 are recognized and bound by TFIIB, the TFIIB-recognition elements BREu and BREd. The other 4 elements are recognized and bound by various TAF (TBP-associated factor) subunits of TFIID. These 7 core promoter elements are present in various combinations to specify transcription initiation sites in the genome of humans and other eukaryotes.

Though TBP binds to the TATA box promoter element with some specificity, TBP must also bind to non-TATA DNA sequences. Bioinformatics analyses of the human genome has suggested that $<1/3$ of human gene promoters contain a TATA box (Suzuki et al., 2001 and Gershenzon and Ioshikhes, 2005). Thus, if TBP is a critical component for transcription, it must also bind these non-TATA box promoters, likely as a component of TFIID and stabilized by other proteins.

Binding of TBP to TATA DNA has been studied extensively. Crystal structures of TBP bound to TATA DNA showed DNA bent at a sharp angle ($\sim 100^\circ$ for human TBP structures, Fig. 1.2 [3]). In solution measurements, TBP-TATA complexes have been studied by fluorescence resonance energy transfer (FRET) [4, 5, 6] establishing confirmation of the bend angle as well as kinetic parameters for TBP binding and bending DNA. While exact experimental conditions and measurements varied, these studies typically found very fast association half-times on the order of seconds and very slow dissociation half-times on the order of minutes. In a single-molecule measurement on yeast TBP, video microscopy was used to observe TBP dependent DNA bending [7]. This single-molecule study showed slower association rates than the FRET studies, but similarly stable TBP-DNA complexes with

very slow dissociation rates. This set of solution measurements suggest a highly stable and static complex of TBP bound to TATA DNA.

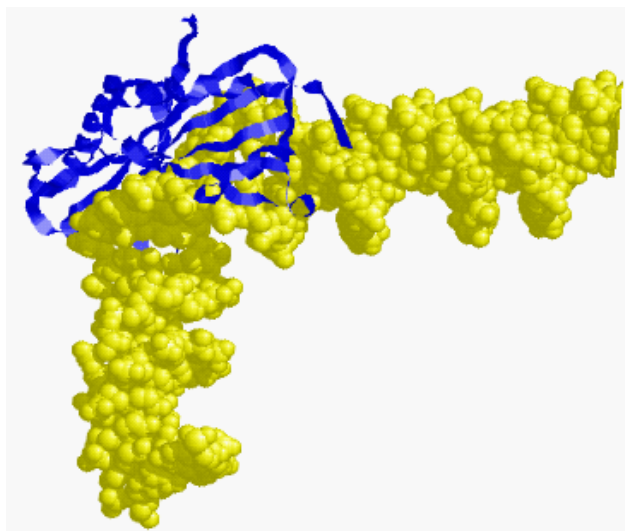


Figure 1.2: Crystal structure of TBP and TATA DNA. Crystal structure of human TBP (*blue*) bending TATA DNA (*yellow*) [3] with DNA extended from original crystal structure by Aaron Hieb [5].

A more recent FRET study by Hieb et al. established a strong KCl concentration dependence of the dissociation rate (k_{off}) of TBP-TATA complexes, finding $k_{off} = 1.3 \times 10^{-2} s^{-1}$ at a KCl concentration of 140 mM, compared with $2.1 \times 10^{-3} s^{-1}$ at 50 mM KCl [5]. The 140 mM KCl concentration is much closer to the physiological monovalent salt concentration in cells than the 50-100 mM KCl used in most other solution studies. This large increase in the dissociation rate at more physiological [KCl] begins to establish a more dynamic picture of TBP binding to TATA DNA *in vivo*, with potentially significant consequences for models describing the function of TBP in transcription regulation.

1.1.3 Architecture of the transcription preinitiation complex

TBP bending DNA is not the only DNA architectural change thought to be important for transcription regulation. Other members of the PIC are thought to induce and/or stabilize bending and looping of the promoter DNA. TFIIA changes the conformation of the

TBP-DNA complex upon binding [5]. Crosslinking studies have suggested other members of the PIC in combination (TFIIB + TBP + TFIIF + pol II) may induce looping of the DNA around pol II and other PIC proteins [8]. Indeed the DNA-protein architecture likely plays a key role in the mechanism of transcription and transcription regulation.

1.2 OPTICAL TRAPPING AND SINGLE MOLECULE TECHNIQUES

The nm-scale changes in DNA extension (distance between the two ends of the DNA) associated with bending and wrapping of DNA around PIC proteins makes the architecture of the PIC an ideal subject for study via optical trapping. In an optical trap, a focused laser exerts forces on small particles, creating an essentially harmonic potential that traps particles at the laser focus. Optical traps are ideal for measuring and manipulating biomolecules at the pN-force scale and the nm-distance scale.

Optical trapping falls into the general category of single molecule techniques. Single molecule techniques involve measurements of the behavior of individual molecules - often molecules of DNA, RNA, proteins. Single molecule studies are in contrast to bulk methods, which observe average behavior of a large population of molecules. A strength of single molecule measurements is the ability to detect time-dependent changes that cannot be synchronized in a bulk population. In addition, the study of individual molecules often allows subsets of populations with heterogeneous behavior to be identified, whereas this heterogeneity would be averaged over the entire population in bulk methods.

Single molecule optical trapping has the potential to elucidate the structure and function of TBP and the PIC. Addressing particular issues, optical trapping could potentially resolve a bending stability vs. bending angle conundrum for TBP bending variant sequences of DNA. Bulk FRET has demonstrated an average angle change for TBP binding to these non-consensus TATA sequences, but the FRET data also suggest a change in stability that could account for or contribute to the apparent angle change (Wu...Parkhurst 2001). In addition, optical trapping could detect individual steps in DNA bending, wrapping and looping

around PIC proteins. This ability to detect time-dependent changes could eventually elucidate pathways for GTF assembly at the promoter, addressing the contrasting models of PIC assembly - sequential assembly of individual transcription factors at the promoter vs. assembly of the proteins in solution before binding DNA (Thomas Crit Rev 2006). Addressing these types of questions via direct measurement of DNA conformational changes would yield exciting contributions to the study of gene expression.

Before these more complicated questions can be answered, a working single molecule assay to study DNA conformational changes by human PIC proteins must be established and proven. Much of this thesis is devoted to this topic, dealing with the challenges presented by the sensitivity and complexity of the human transcription machinery. Ultimately, human TBP bending DNA was chosen for the studies presented, as TBP binding DNA is the first step in PIC assembly, making the TBP-DNA complex the simplest complex for study, as well as a complex of primary importance.

1.3 THESIS OVERVIEW

In this thesis, single-molecule TBP-dependent extension changes of DNA are reported, along with the actively stabilized, axial optical trapping assay developed to measure them. Chapter 2 details the experimental techniques, first discussing the instrument components, alignment, calibrations, and characterization, followed by sample preparation methods, then data acquisition and analysis details. Chapter 3 details the axial trapping and detection technique, discussing improvements on previously developed techniques and a true novel contribution in the form of a method for force and extension measurement that combines the theoretical dependencies of drag coefficients near surfaces and DNA polymer theory. Finally Chapter 4 reports direct measurements of TBP bending DNA.

The major results of this work are two-fold: 1) a stabilized, axial optical trapping method capable of high-resolution measurements on very short DNA and 2) a direct measurement of human TBP bending DNA. The novel method of axial force and extension

estimation allow precision measurements on very short DNA that expands the range of possible biological phenomenon that can be studied by optical trapping. The measurement of human TBP bending DNA is the first single molecule study to my knowledge of a component of the human transcription machinery. The measurement establishes and quantifies TATA box dependent extension changes of DNA, measuring characteristic bending and unbending rates of tens of seconds. The dynamic nature of the TBP-DNA complex measured in this work, while in agreement with the more recent FRET measurement of a faster dissociation at physiological salt concentrations, contrasts with some traditional models of TBP's role in transcription as a stable, essentially static scaffold for recruiting transcription factors. This work suggests a more dynamic role for TBP in transcription regulation.

Chapter 2

EXPERIMENTAL TECHNIQUE

One of the challenges in studying TBP bending DNA at the single-molecule level was the development of a working biophysical assay. The working assay needed to be capable of measuring single DNA bending events on the slow time scale (~ 1 event per 100 s) [5] and small length scale ($\Delta \sim 5$ nm) [9] predicted for TBP. The assay also needed to preserve the activity of the protein, prevent non-specific sticking, and yield an interpretable, repeatable signal. To achieve this working biophysical assay, we built an actively stabilized optical-trapping instrument, implemented customized non-stick surface chemistry, and developed a novel axial trapping and detection technique. Additionally, for data analysis, we adapted a hidden Markov modeling algorithm and developed a drift-correction capability to correct for baseline drift of our data traces. Using this biophysical assay and data analysis technique, we obtained the TBP data and interpretations in this thesis.

This chapter and the next describe the instrumentation and experimental techniques used to obtain and interpret the data in this thesis. The actively stabilized optical-trapping instrument is described and characterized. The customized non-stick surface chemistry and other biological assays are then described, followed by the data acquisition and data analysis. The novel axial detection method is discussed in the next chapter.

2.1 COMPONENTS OF THE INSTRUMENT

An actively stabilized optical-trapping microscope was the key to studying the infrequent, small DNA extension changes caused by TBP. In designing this instrument, based on previous work [10, 11, 12], the goals to be achieved were three-fold: the instrument needed to have 1) a strong, non-biologically-damaging optical trap; 2) precision detection and positioning capabilities; and 3) long-term stability for measurements. The instrument we developed to achieve these goals is shown in the optics diagrams, Figs. 2.1 and 2.2. The figures show three lasers: a high-powered trapping laser (1064 nm) and two lower-powered detection lasers (850 nm and 810 nm). In our experiments, the trapping laser trapped a micron-sized bead attached to DNA; one detection laser detected the position of the trapped object, while the other detection laser detected drift between the laser foci and the sample surface. By both active and passive stabilization techniques, we suppressed pointing, mode, polarization and intensity noise of our three lasers, and actively stabilized the sample position relative to the lasers. Through this stabilization scheme, we achieved a stable optical-trapping instrument capable of precision measurements. The components of this instrument will be described in detail in this section.

Before detailing the components of our instrument, a quick overview of the key elements provides a framework for how each contributes to our goals. Beginning with the lasers, each of the three lasers was guided through an AOM to control the intensity, then coupled through an optical fiber to refine the mode. Next, a beam sampler picked off $\sim 10\%$ of each laser to sample the intensity, detected by a photodiode. The intensity on the photodiode was stabilized by servo-electronics, which controlled the intensity via the AOM. Next, the trapping laser and one detection laser were reflected by PZT mirrors, which steered the beams in the optical-trapping microscope. The three lasers were coupled into the microscope by dichroics. The lasers were focused into the sample plane of the microscope by a high NA objective. A condenser collected the laser light for back-focal-plane detection with

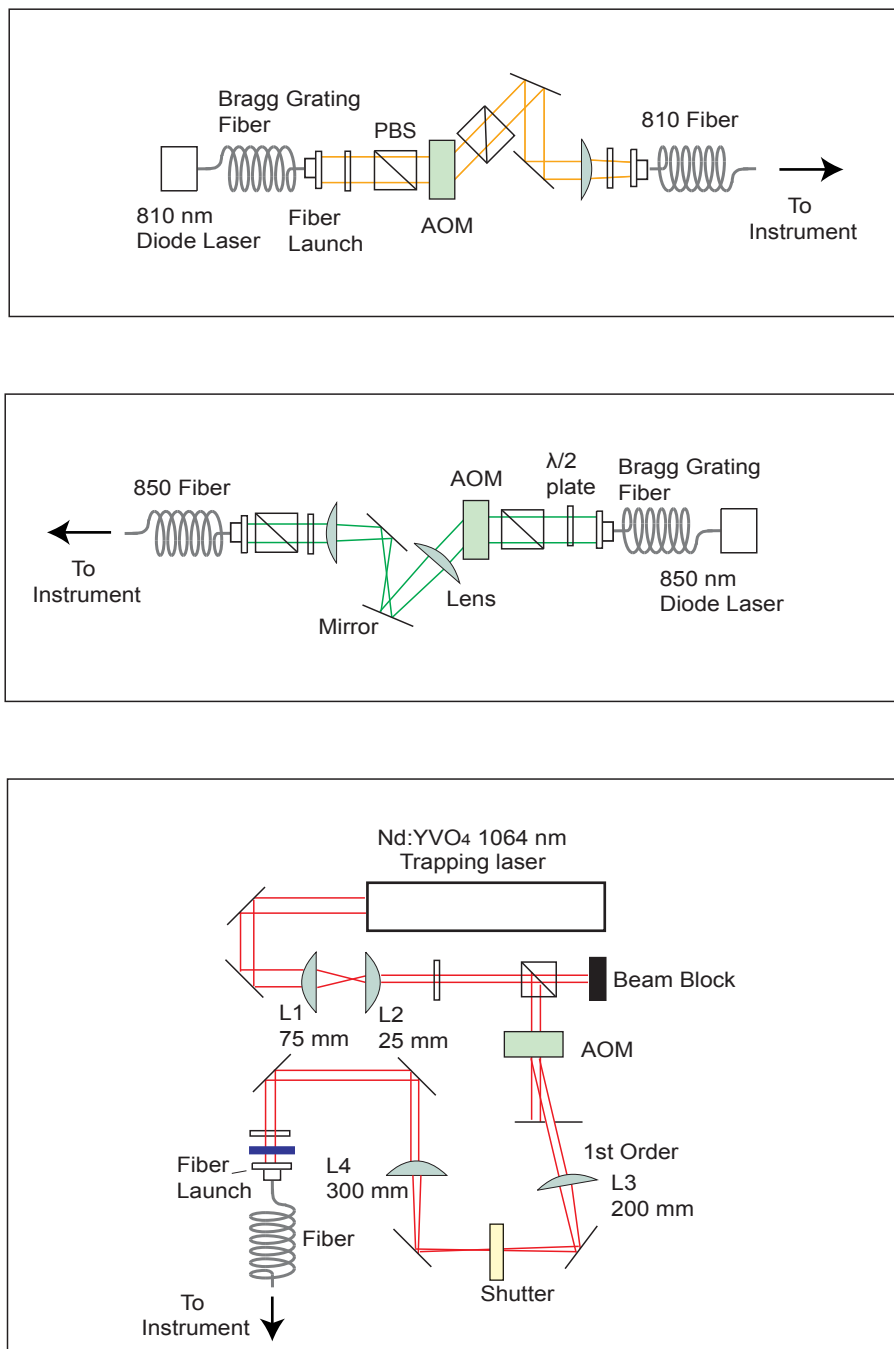


Figure 2.1: Pre-fiber instrument setup diagram. Diagram of the pre-optical-fiber setup of the three lasers in the optical-trapping instrument used in the work in this thesis. Abbreviations in diagram: AOM (acousto-optic modulator), PBS (polarizing beam splitter), L (lens).

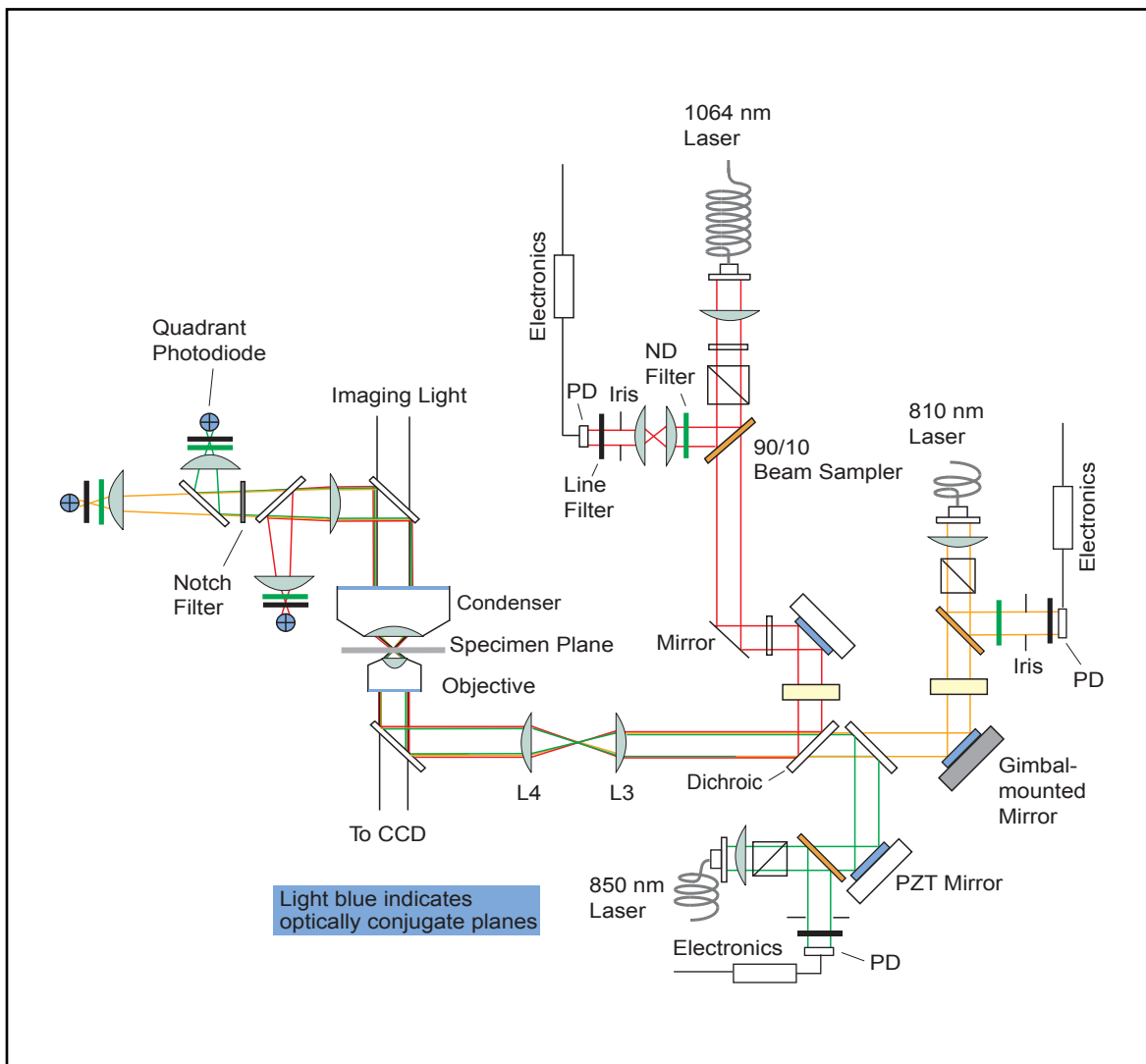


Figure 2.2: Post-fiber instrument setup diagram. Post-optical-fiber diagram of the optical-trapping instrument used in the work in this thesis. Abbreviations in diagram: PD (photodiode), ND filter (neutral density filter), PZT mirror (piezo-electric mirror), L (lens), CCD (CCD camera).

quadrant photodiodes (QPDs), placed in a custom-built detector arm attached to the condenser column of the microscope. Precision movement of the sample was accomplished by a piezo stage. The stabilization of the microscope was achieved by several passive stabilization techniques (described in Section 2.1.10), combined with active laser intensity stabilization via the AOMs and intensity servo electronics and active sample stabilization by the piezo stage and a software-based position servo. Given this framework, the details of these key components follows.

2.1.1 Lasers for trapping and detection

The trapping laser in our optical-trapping instrument was a high-powered, 1064-nm Nd:YVO₄ laser (Spectra-Physics, Millennia IR). This laser was chosen due to commercial availability, high-power, and a desirable wavelength for minimizing biological damage [13]. The laser has a maximum available power of 10 W; we operated at 7.8 W (reading of 7.77 W on the laser controller) to achieve high power and stability. This high power necessitated mirrors, lenses, and other optics in the instrument be chosen with high-damage thresholds, particularly for optics before the optical fiber where the beam diameter is small (~ 2 mm). To improve stability, the cooling system for the laser was modified. Explicitly, the internal fan on the laser head was replaced with an external fan coupled to the laser via air ducts, and the cooling cycle was changed from a modulated cooling cycle to continuous cooling. The trapping laser and optics before the optical fiber are shown at the bottom of Fig. 2.1. This trapping laser provided the high-powered laser needed for creating a strong optical trap in our instrument.

For reference, the trapping-laser beam profile is shown at two different saturations in Fig. 2.3. The beam profiles characterize the shape and quality of the trapping laser, including rings which are visible in the saturating profile. Note that the beam passed through many other optics before passing into the optical-trapping microscope, including an optical fiber that refined the mode, creating a nicely Gaussian beam profile before forming the optical

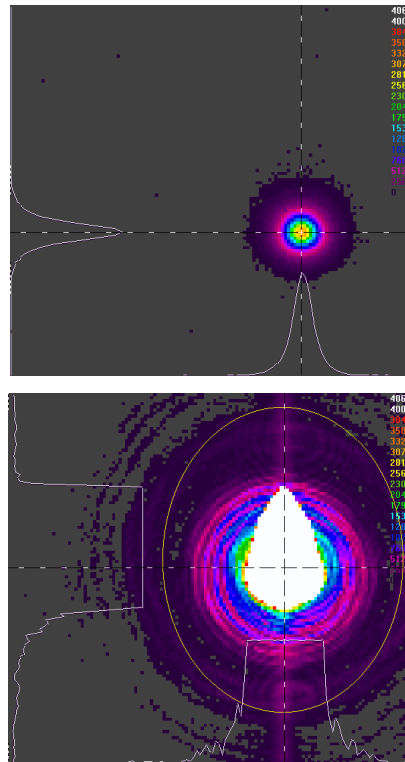


Figure 2.3: Beam profile. Beam profiles taken of the 1064 laser using the Beam Profiler from the Keck lab. The profiles were taken at medium power to be representative of typical running power (typical running power is 7.77 W out of a possible 10 W). The unsaturated profile at the top shows a nicely Gaussian beam. The saturated profile at the bottom shows the rings that become evident further from the Gaussian center of the laser beam. These profiles were in the beam path very close to the laser, before the AOM and fiber.

trap.

The detection lasers in our instrument were diode lasers: an 808-nm diode laser (Lumics, 100 mW) for detection of the trapped object, and an 845-nm diode laser (Lumics, 200 mW) for detection of drift of the sample surface. These lasers are often referred to as the 810 (referring to the 808-nm) and the 850 (referring to the 845-nm) lasers. The laser wavelengths were again chosen to minimize biological damage, and the separation between the wavelengths of the three lasers in the instrument allowed for separating and combining the lasers using dichroics. The detection lasers and optics before the optical fiber are shown in the top two boxes of Fig. 2.1. Both detection lasers were fiber-Bragg-grating stabilized. The Bragg-grating fibers are not polarization-maintaining fibers, and the polarization of the beams at the fiber outputs appeared sensitive to the fiber-coiling geometry and subject to drift over long periods of time (weeks to months). The polarization after the Bragg-grating fiber was purified with polarizing beam splitters (PBS), and the polarization and power could be tuned with half-wave plates ($\lambda/2$). These diode lasers provided the detection for stabilizing our instrument and making precision measurements.

The three-laser scheme in our instrument was one of the keys to achieving an instrument capable of precision measurements with long term stability. In contrast, many optical trapping instruments implement a single laser to both trap and detect. These single-laser systems typically obtain average detection sensitivity calibrations for a given batch of beads, then apply those average calibrations during their experiments. However, detection sensitivity varies with the volume of beads, and in a batch of beads, bead radius actually varies with typical coefficients of variation of $\sim 3\%$ according to manufacturers specifications. This variation in size causes a variation in detection sensitivity of 9% , which is unaccounted for by using average detection sensitivity calibrations as in single-laser systems. On the other hand, implementing a separate laser for detection of the trapped bead allows detection sensitivity calibrations of the individual bead to be measured in each experiment, improving the precision of the detection calibration. As another advantage, a separate detection laser also

allows multiple means of calibrating the stiffness of the optical trap, which not only provides a more trustworthy stiffness calibration, but also provides a diagnostic tool for testing the quality of the trap (see Section 2.4.15 for more details). The third laser in our system was the key innovation for stability of our instrument. This third laser provided the means for detecting the position of the sample relative to the lasers, which was then stabilized via the piezo stage. Using a second laser in our system to detect the position of the trapped bead improved the precision and reliability of our measurements, and using a third laser provided the long-term stability necessary for our measurements.

Because separate lasers were used for trapping, detection, and stabilization, any relative motion of the lasers relative to one another would detract from the stability and precision of our measurements. Thus it was essential that the relative pointing of the lasers be very stable relative to one another. This pointing stability was achieved through several passive stabilization techniques, as discussed in Section 2.1.10.

2.1.2 Acousto-optic modulators (AOMs) for intensity control

Each laser in our instrument passed through an acousto-optic modulator (AOM, Isomet 1205C-2, lead molybdate crystal) to provide intensity control. The AOM alignment was optimized in the procedure outlined in A. Carter’s Thesis [14]. Briefly, the laser was collimated at a 2 mm diameter to maximize the diffraction efficiency through the AOM. As shown in Fig. 2.1, for the trapping laser two lenses collimated the beam. For the detection lasers, diffraction efficiency was less essential, and one lens or no lens was used to adjust the beam collimation before the AOM. The AOM driver (Isomet 232A-2) settings were set to maximum diffraction efficiency (“bias adjust” turned completely counter-clockwise, “power adjust” turned completely clockwise minus 1/4 turn). The AOM was then manipulated via a tip-tilt stage until the power in the 1st-order diffracted beam was maximized, achieving $\sim 70\%$ efficiency.

For the trapping laser, the AOM provided dynamic control of the trap power. Dynam-

ically changing the power via the AOM caused heating of the AOM crystal, which resulted in changes in beam pointing [15, 12]. To minimize the effect of these beam pointing changes, we imaged the center of the AOM crystal onto the fiber-coupling lens (see Fig. 2.1) and optimized the alignment after the AOM at $\sim 50\%$ of the maximum diffraction power (0.5 V “video” input on the AOM-driver). Further optimization, including re-optimization of the fiber alignment at a more carefully chosen AOM control voltage, is included in Section 2.2. The intensity control provided by the AOM allowed stabilization of the laser power for all three lasers, as well as modulation of trap power for the trapping laser.

2.1.3 Optical fibers for beam refinement and pointing stability

Each laser in our instrument also passed through a single-mode, polarization-maintaining optical fiber (Oz Optics). (For a How-To guide on optimizing fiber alignment in a similar setup, see A. Carter’s thesis [14].) The fibers refined the mode of the lasers, ensuring the beams were nicely Gaussian before entering the optical-trapping microscope. The fibers themselves were mechanically stabilized at the fiber output to prevent motion of the fibers that could result in pointing noise after the fiber. Because the fiber-coupling efficiency was very sensitive to beam pointing changes and mode noise before the fiber, the fiber also automatically converted any beam-pointing or mode noise before the fiber into intensity noise after the fiber. After the fiber, the intensity stabilization suppressed this intensity noise. Passing the lasers through optical fibers refined the laser mode and transferred pre-fiber mode and pointing noise into intensity noise to be stabilized after the fibers.

2.1.4 Samplers and photodiodes for intensity stabilization

After the optical fiber, each laser was sampled for intensity stabilization. Each laser first passed through a PBS to purify the polarization, causing polarization noise to be converted into intensity noise. Next a 90/10 beam sampler (Newport) diverted $\sim 10\%$ of the laser onto a photodiode (EG&G Optoelectronics Canada YAG-444A) for intensity detection.

Stabilization of the intensity was performed by servo-electronics, which controlled the intensity via the pre-fiber AOMs. By stabilizing the sampled intensity of each laser, we stabilized the intensity of the our optical trap and detection lasers.

2.1.5 PZT mirrors for beam steering

The 1064 nm and 850 nm lasers were steered in the microscope by PZT mirrors (PI S330.2SL PZT mounts, Thorlabs mirrors). Applying a voltage to the PZT mirrors rotated the mirrors, which resulted in translations of the lasers at the imaging plane. To ensure that rotations of the PZT mirrors resulted in pure translations at the imaging plane, the PZT mirrors were placed at a plane optically conjugate to the back-focal-plane of the objective (see Fig. 2.4). This placement was achieved by using two lenses to form an imaging system that images the PZT mirrors onto the back-focal-plane of the objective.

Determining physical placement of the PZT mirrors involved measuring backwards along the beam path from the effective back-focal plane of the microscope. We estimated 7.8 cm above the center of the dichroic at the base of the microscope as our effective focal plane, half-way between the back aperture and the Nikon-estimated position of the back-focal plane. The lens closest to the microscope was placed its focal length (25 cm) from the effective back-focal plane, which was 17.2 cm from the horizontal midplane of the microscope. The lens closest to the PZT mirrors (focal length=14 cm) was placed a distance of the sum of the focal length of both lenses (39 cm) from the other lens. Each PZT mirror was placed at the focal length behind the lens closest to the PZT mirrors. With this imaging system and placement, the PZT mirrors steered the lasers in the imaging plane of the microscope.

2.1.6 Dichroics for light integration and separation

To integrate all three lasers and the imaging light into the optical-trapping microscope, the lasers and imaging light were combined and split via dichroic mirrors (Chroma). Note that the imaging light coupled into the microscope in the reverse direction from the lasers.

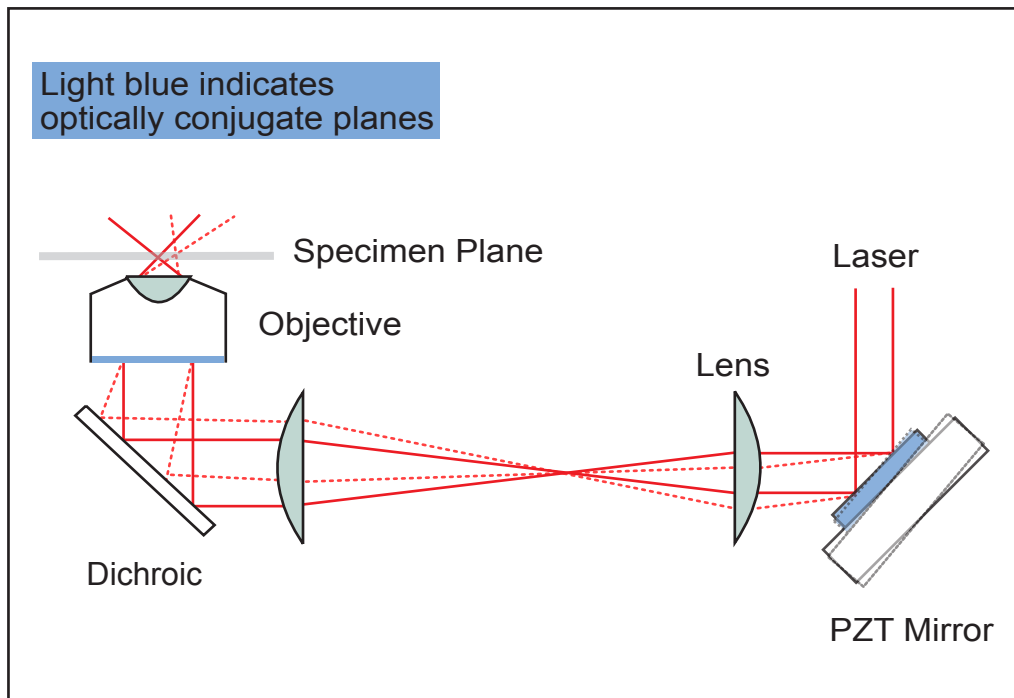


Figure 2.4: PZT mirror beam steering diagram. The PZT mirror is in a plane optically conjugate to the back focal plane of the objective so that pure rotations of the PZT mirror cause pure translations at the sample plane.

Two dichroics before the microscope combined the three lasers into a single beam path. A dichroic in the base of the microscope reflected the three lasers up into the microscope and transmitted the imaging light through to the camera and microscope eyepiece. A dichroic above the condenser also transmitted the imaging light and reflected the laser light into the detector arm of the microscope. Within the detector arm, two dichroics separated the three lasers so that each laser was impinging on a separate detector. The dichroics allowed the lasers and imaging light to be integrated into the microscope and separated for individual detection.

2.1.7 Microscope for optical trapping

The optical-trapping microscope was an inverted Nikon TE2000-S modified to enable stabilized trapping and detection. The microscope had a 1.4 numerical aperture (NA) objective (Nikon CFI Plan Apochromat 100x oil IR, NA 1.4, working distance 0.13 mm) that focused the trapping and detection lasers and collected the imaging light. A Bertrand lens allowed imaging of air bubbles in the immersion oil between the lenses and sample, which were avoided as they degraded the trapping and detection properties of the microscope. The condenser (1.4 Nikon HNA Oil) collected the laser light for detection and passed the imaging light into the imaging plane. The microscope was modified for stability by adding an aluminum plate to stabilize the condenser column and using custom, monolithic holders for the stage and for the objective. The imaging light was coupled via a liquid light guide, with the lamp placed several feet away from the microscope to minimize drift induced by heat from the lamp. The microscope was modified for detection of the laser light by adding a custom-built detector arm to the condenser arm of the microscope. With these modifications, the microscope became a stabilized optical-trapping microscope.

2.1.8 Piezo stage for sample control

For sample control in the microscope, a piezo stage (PI P-517.3CD) was mounted onto the monolithic stage holder. The stage defined the axes for the experiment. The piezo stage allowed for precise (sub-nm) computer-controlled movement of the sample, as well as automated calibrations. Importantly for our instrument, computer control of the stage was the key to active stabilization of the sample position.

2.1.9 Detectors and electronics for visualization and detection

Detection in our instrument was accomplished by quadrant photodiodes (QPDs) and a CCD camera. The CCD camera (DAGE-MTI CCD100S) allowed for visualization of the sample and lasers, while the QPDs allowed for precision laser detection of objects in the microscope. The QPD's were mounted onto the detection arm for back-focal-plane detection [16, 17]. The voltage output from each QPD was digitized, anti-aliased, and converted into x , y , and z voltage signals with custom JILA electronics (see Table 2.1 for typical detection electronics settings). The x and y voltage signals were based on the normalized difference between halves of the QPD, while the z voltage signal was the sum of the four quadrants modified by a separate differential gain amplifier. These detector signals, with the settings listed in Table 2.1 represent the x , y , and z detection voltage signals shown in this thesis.

2.1.10 Components for passive stabilization

To achieve the high level of stability in our optical-trapping instrument, we implemented several other modifications. We mounted the microscope and our optics on floating optical tables (TMC). The experiments were performed in a temperature-stabilized (± 0.2 C), acoustically quiet (NC30) room with a specialized air-venting system to minimize air currents. The noisy, heat-generating pump lasers were in a separate room. All optics before the microscope were enclosed in plexiglass boxes. Most optics mounts after the fiber were

Table 2.1: Typical detection electronics settings.

	1064 ^a	850	810
<i>x-y</i> gain	2 (0.5 in window)	0.5	0
<i>x-y</i> balance	5 in window	5 in window	5 in window
post amp gain ^b	max	×1.5 (looks like 2 on dial)	×2
diff amp gain	×1	×1	×1
antialiasing	DAQ rate/2 ^c	DAQ rate/2	DAQ rate/2
<i>z</i> diff amp gain ^d	×50 ^e	×100	×100

^a We only detected with 1064 for troubleshooting.

^b Optimized for bead size.

^c 1064 antialiasing filter did not filter.

^d Was optimized for bead size.

^e 1064 DC offset amplifier gain was too high even at the lowest setting.

customized, wide-based mounts, and cables and fibers were stabilized with clamps and supports. The post-fiber optics were on an elevated breadboard to minimize the height of the mounts. These extra modifications added stability to our instrument, particularly stabilizing the pointing of the lasers relative to one another, which was critical to our active-stabilization scheme.

2.2 INTENSITY STABILIZATION

Many of the components mentioned in the preceding section combined to provide intensity stabilization of the lasers in our instrument. The intensity stabilization is described in detail in A. Carter's thesis [14]. In brief, AOMs before the optical fibers provided active control of the intensity of each laser. Beam samplers after the optical fiber reflected $\sim 10\%$ of each laser onto a photodiode to measure the intensity. The signal from the photodiode was optimized with ND filters, an iris, and a resistor in the photodiode. The ND filter was chosen to ensure the power onto the photodiode would not overheat the photodiode. The iris ensured unwanted beam reflections were not projected onto the photodiode, and the resistor was chosen so that the desired range of intensities resulted in a photodiode voltage signal between 0-10 V (i.e., not saturating the photodiode range and matching the range available by computer-control). JILA-made servo electronics received the photodiode signal and sent a signal to the AOM to stabilize the intensity on the photodiode. The optics before the intensity measurement were designed to convert various forms of noise into intensity noise: the optical fiber converted pointing and mode noise and the PBS converted polarization noise. By stabilizing the intensity noise after the other noise sources were converted, we stabilized pointing, mode, and polarization noise, as well.

2.2.1 Nonlinearity of servo response

The intensity stabilization required several steps for optimization. In addition to the inherent nonlinearity of a typical AOM response, laser intensity changes via the AOM re-

sulted in thermal changes in the AOM crystal which led to pointing changes in the beam. Because the beam was passed through an optical fiber after the AOM, these pointing changes resulted in changes in the fiber-coupling efficiency (but not pointing changes after the fiber). The changes in fiber-coupling efficiency caused a nonlinearity and even an inversion of the relationship between the applied AOM voltage and the measured photodiode voltage after the fiber, as shown in Fig. 2.5. To optimize the servo performance, operating the instrument near the center of the linear region provided the best intensity stabilization.

2.2.2 Optimization of fiber coupling at the ideal AOM setting

For the detection lasers, which operated at a static AOM voltage, we optimized the fiber coupling at an intermediate AOM voltage ($V_{AOM}=0.3-0.5$ V) and measured the photodiode voltage as a function of AOM voltage. Note that the location of the linear region may depend on the fiber optimization voltage, but a quick check of this dependence by doing the measurement at different fiber optimization voltages showed little to no dependence (data not shown). For the detection lasers, we chose a voltage near the center of the linear region as the static voltage for stabilization.

Once the optimum AOM voltage for stabilization of the detection lasers was chosen, to achieve the desired laser power at the optimized AOM voltage, we had two options. One option was to adjust the diode-laser current-temperature controllers. This option was judged not best because the diode laser stability and other properties may also change with the current and temperature. The second option for controlling the laser power was to adjust the half-wave plates before the PBS cubes in the pre-fiber optics (see Fig. 2.1). We chose this option to dial in the desired laser power. The resulting laser powers (quantified in Section 2.4.14) were low enough power to not trap objects in the microscope, but high enough to provide an ample signal for detection.

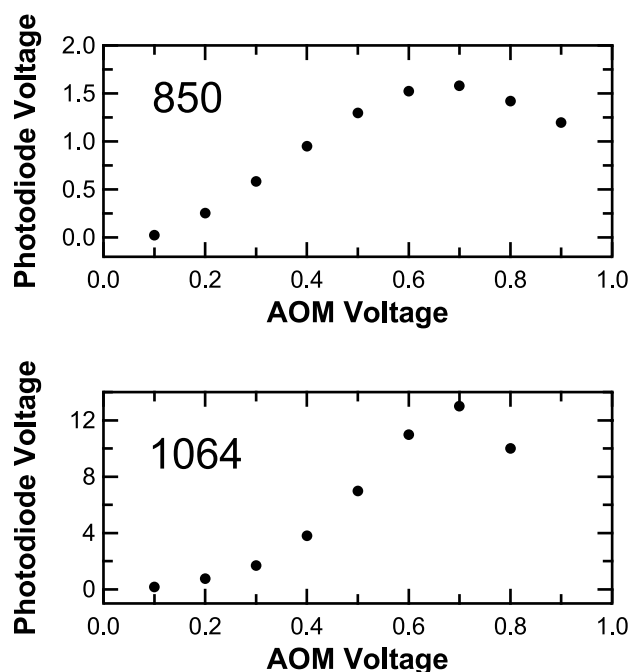


Figure 2.5: Photodiode voltage vs. AOM voltage. The plots show an approximately linear region, as well as highly nonlinear regions. The linear region shows photodiode voltage (power) increasing with applied AOM voltage, as expected. The nonlinear regions are largely due to pointing variations in the beam, which are translated into power variations at the photodiode. The pointing variations are caused by thermal changes in the AOM crystal as the applied voltage changes. The pointing variations are transferred into power variations because the beam is fiber-coupled between the AOM and the photodiode. This fiber-coupling efficiency is highly sensitive to pointing variations. The result is a nonlinear power response recorded at the photodiode, but highly stable beam pointing after the fiber. For maximum power stability, the 850 laser was coupled to the fiber at an AOM voltage in the center of the linear region (0.35 V applied to the 850 AOM). For stability and dynamic range, the 1064 was coupled in the lower half of the linear region, at 0.4 V applied to the 1064 AOM.

2.2.3 Optimization of servo electronics

In the final step of servo optimization for both the diode lasers and detection lasers, the servo electronics themselves were optimized. To optimize the servo electronics, we measured the noise using a Network Signal Analyzer (Stanford Research Systems Model SR780). Plots of the noise vs. frequency are shown in Fig. 2.6. We adjusted the coarse and fine gain on the servo, increasing until the servo began to oscillate, then backing off. We then adjusted the PI corner on the servo. The goal of these adjustments was to push the noise level as low as possible out to as high a frequency as possible. The peak in the noise level on the right hand side of Fig. 2.6 tends to move with the gain and PI corner, and by iterating through adjustments of the gain and PI corners, this peak was pushed to as high a frequency as possible, while also keeping the noise low at lower frequencies. The final settings for the servo electronics are listed in Table 2.2. Fig. 2.6 shows the noise level with the servo on was decades lower than with the servo off, up to around 60 kHz. By this series of steps, 1) optimizing fiber coupling at a mid-range AOM voltage, 2) operating at the center of the linear region of the photodiode vs. AOM voltage response, 3) optimizing the laser power via the pre-fiber half-wave plates, and 4) optimizing the servo gain and PI corner, we optimized the intensity stabilization of the detection lasers.

Table 2.2: Typical intensity servo settings.

Laser	coarse gain	fine gain	PI corner
1064	max - 6 clicks	max - 1 turn	max - 3 turns
850	max - 1 click	no info.	no info
810	max	no info.	no info.

2.2.4 Optimization for stability and dynamic range of the trapping laser

For the trapping laser, stability combined with a dynamic range of trapping powers was required, slightly altering optimization from that of the detection lasers. The important

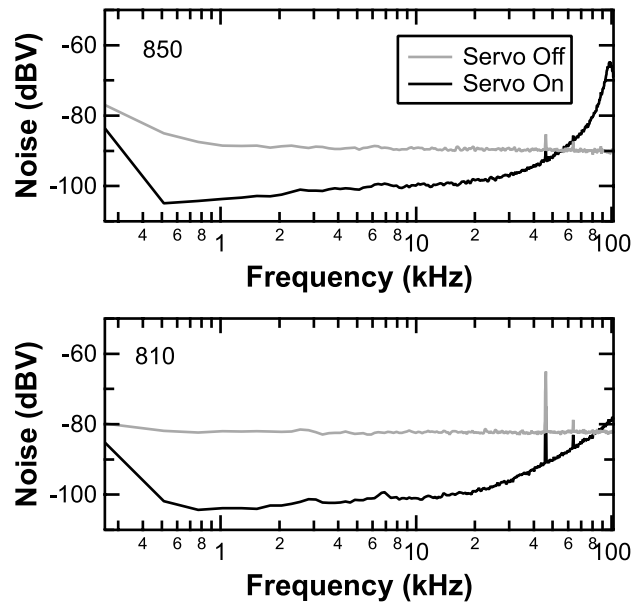


Figure 2.6: Intensity noise of 810 and 850. In-loop photodiode noise vs. frequency for 810 (lower plot) and 850 (upper plot) lasers, as recorded on a Network Signal Analyzer (Stanford Research Systems Model SR780). Lower frequency noise was highly suppressed with the servo on (*black*) compared to with the servo off (*gray*).

difference here between the trap-laser optimization and detection-laser optimization was that for the trap, the AOM was used to dynamically control the trap power, so we could not simply operate the servo at one optimum AOM voltage. Most of the steps in optimization were similar to those for the diode lasers, with the modifications described below.

We optimized the fiber coupling at a mid-range AOM voltage (0.6 V) and measured the photodiode voltage vs. AOM voltage. The center of the linear region was at ~ 0.5 V, but optimizing the fiber coupling at this voltage was difficult because once the system thermally stabilized and the fiber was optimized at that voltage, the photodiode voltage was near saturating. So instead, we optimized the fiber coupling at an AOM voltage of 0.4 V, and then completed the servo-electronics optimization procedure.

We measured the noise using the Network Signal Analyzer at three different servo voltages, low (0.4 V), intermediate (1 V), and high (9 V) as shown in Fig. 2.7. Again, with the servo on, the noise was clearly decreased as compared to with the servo off. As a final check of the servo stability over the range of powers, as well as a check of the dynamic range response, we measured the photodiode voltage vs. time. Fig. 2.8 shows the stability of the photodiode voltage at a low voltage (0.4 V, top) and a high voltage (9.5 V, middle). This figure also shows the dynamic response of the photodiode voltage as the requested locking voltage was oscillated in a square wave between 0.4 V and 9.5 V (bottom). This figure shows the trapping laser intensity stabilization was both stable and capable of fast changes in power.

Over time (several months), the intensity stabilization and/or dynamic range sometimes degraded. The servos completely stopped locking, or unlocked more easily than before. Typically this degradation could be remedied by re-optimizing the fiber coupling, choosing the same AOM voltage for fiber coupling as before. Maintaining the intensity stabilization described was one essential component of our actively stabilized optical-trapping microscope.

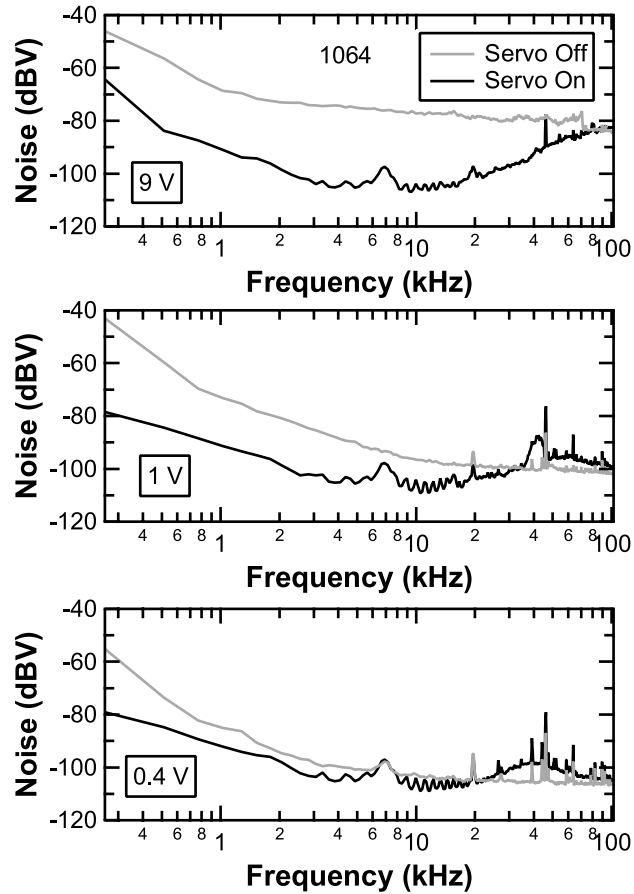


Figure 2.7: Intensity noise of 1064. In-loop photodiode noise vs. frequency for the 1064 laser at 3 different photodiode voltage levels, as recorded on a Network Signal Analyzer (Stanford Research Systems Model SR780). The magnitude of the noise changes with the voltage, but in all cases lower frequency noise is highly suppressed with the servo on (*black*) compared to with the servo off (*gray*).

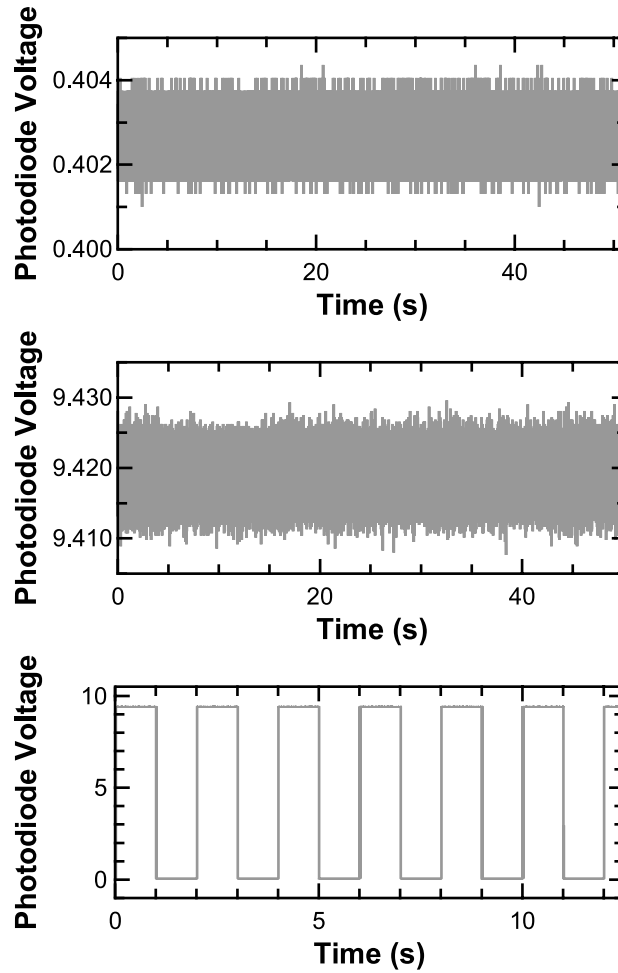


Figure 2.8: Trap intensity stabilization. In-loop photodiode voltage with intensity stabilization and intensity ramping. In the top plot, the servo voltage was set to 0.4 V; in the middle plot, 9.5 V. For the top two plots, we quantified the peak-to-peak noise (max-min/mean) and the average noise (std. dev./mean). The noise for the two plots shown are as follows: at 0.4 V, peak-to-peak noise = 0.8%, average noise = 0.1%; at 9.5 V, peak-to-peak noise = 0.2% and average noise = 0.02%. The plots show the servo is able to remain locked and stable at the low and high end of the available voltage range. The bottom plot shows the in-loop photodiode response to jumps in the servo voltage from 0.4 V to 9.5 V. This plot shows the 1064 nm servo is capable of maintaining stability even while making large, fast jumps in voltage.

2.3 SAMPLE STABILIZATION

The other essential component of actively stabilizing our microscope lay in actively stabilizing the sample position relative to the lasers. To perform this stabilization, we used an old microscopy trick in which a fiducial mark tracks the drift of the sample. In our case, the fiducial mark was typically a micron-sized bead, fixed to the sample surface. We detected this fiducial with the second detection laser in our system (845 nm), and we actively stabilized the fiducial's position using the piezo stage and a software-based servo. The software-based servo was written in LabVIEW. The position signal from the QPD was read into LabVIEW, an error signal was generated as the difference between the current position and the desired position, and proportional gain was applied to generate a correction signal to move the stage and maintain the desired position. By actively stabilizing the sample position relative to the second detection laser, combined with all of the active and passive stabilization described above, we achieved a stable optical-trapping microscope.

The preceding sections describe the individual components of our actively stabilized optical-trapping instrument, as well as details of our intensity and sample stabilization. As a reference, the typical detector settings (Table 2.1), servo settings (Table 2.2), and laser settings (Table 2.3) are listed in table form. With this instrument, we achieved our instrumentation goals: a strong, non-biologically damaging optical trap capable of precision positioning and detection, with excellent long term stability.

2.4 ALIGNMENT, CALIBRATIONS AND CHARACTERIZATION OF THE INSTRUMENT

Careful instrument characterization was essential to making precision measurements with our instrument, as well as understanding the limitations of these measurements. This section outlines the steps taken to align our optics, calibrate our measurements, and quantify our instrumental stability.

Table 2.3: Typical laser settings.

Laser	Controller Setpoint	AOM voltage for fiber alignment	Servo Voltage
1064	7.77 W setpoint (7.78 W on indicator)	0.4	-4 ^a
850	-275 mA, Tcoarse 26 Tfine 0 on dial, 10 in window	0.35	Manual setting 71 on dial
810	-235 mA, Tcoarse 23 Tfine 0 on dial, 10 in window	0.3	Manual setting 9 on dial

^a subject to change for desired trap stiffness

2.4.1 Alignment into the microscope

Aligning the three lasers into the microscope was a somewhat iterative process. The first step of the process began with careful alignment of each laser as it exited the optical fiber. The beam quality needed to be excellent (look like a perfect Gaussian by eye) at the fiber exit. If it was not, polishing the fiber often improved the beam quality, but if fiber-polishing failed, we replaced the fiber with a new one. After exiting the fiber, each laser was partially collimated by a short focal length (6-8 mm) aspheric lens (OFR). These lenses often introduced rings or other beam imperfections; we typically tried multiple lenses until we found one that did not mar the beam quality. Next, the laser passed through a 2nd lens to complete the collimation at the desired beam size. Collimating the beam and ensuring it projected straight and level at the desired height (12.09 cm from the breadboard) after the fiber exit provided the appropriate starting point for aligning into the microscope. The alignment was checked to ensure the beam remained level after encountering the other mirrors before entering into the microscope.

Once the lasers were coupled into the microscope (via the system of mirrors, dichroics, and lenses in Fig. 2.2), the lasers could be visualized on the CCD camera. A typical sample (microscope slide with a coverslip affixed via double-sided tape) was inserted into the microscope with the coverslip on the bottom. The microscope was aligned (objective moved

to focus on coverslip surface, condenser aligned for Kohler illumination). The lasers reflected slightly off the coverslip surface, and with appropriate filters and camera adjustments, enough light leaked through to the CCD camera to visualize the laser foci. The laser foci were made to appear symmetric, and alignment was adjusted to ensure the laser spots remained symmetric even when moved via the PZT mirrors. If the spots were not symmetric, the beams were checked for misalignment, clipping, or degradation somewhere in the beam path. Visualization of the lasers via the CCD camera was the first step in fine-tuning the alignment into the microscope.

2.4.2 1st-order focal-plane alignment: Aligning laser foci with imaging plane

The laser spots were also made to be visible at approximately the same imaging plane as objects in the microscope sample. If the spots were not visible at the imaging plane, the laser collimation was adjusted by adjusting the position of the fiber at the fiber launch. In practice, we found aligning the laser spots at the imaging plane of the microscope as visualized on the camera resulted in a less-than-optimum trap quality (possibly due to differences in wavelength of the imaging light and laser light). We therefore offset the camera so that the camera visualized an imaging plane that coincided with the laser foci at a point that optimized trap-quality (Note: this alignment was only possible after iterating through later steps in the alignment process to determine the alignment that optimized trap quality). Having the imaging plane and laser foci aligned is not essential for performance, but is very convenient for the user. Characterization of the laser spots in our instrument is available on video [AEC VHS video]. This video shows all three lasers on a sample of beads fixed to the coverslip surface.

2.4.3 Alignment of QPD axes with stage axes

The next step in aligning the instrument was aligning the axes of each QPD with the piezo-stage axes. First, the QPDs were “zeroed,” i.e. centered with the laser paths. This

centering was accomplished with a sample on the microscope with nothing in the beam path. Then x and y micrometers on the QPDs were translated until the x and y output voltages read 0 V. (This QPD centering was performed at least daily to guarantee precise centering of the QPDs and lasers.) After QPD centering, the alignment of the QPD axes with the stage axes was characterized by scanning a bead fixed to the sample surface through the lasers in the x and y axes, using the piezo stage. Typical scans are shown in Fig. 2.9. Alignment of the QPD with the stage axes was performed by rotating the QPD until the crosstalk amplitudes of the non-moving axes were minimized.

2.4.4 Centering beads and beams

Once the QPD axes were aligned with the stage axes, scans like those in Fig. 2.9 could be used for centering a laser over a bead or centering a bead under a laser. In combination, these centering routines could also center two lasers over the same bead, thus aligning the lasers with each other. This alignment was accomplished through an automated centering routine written in LabVIEW. First, a bead was scanned in x and y through one laser via the stage to obtain signals like those in Fig. 2.9. The on-axis signals were fit to the derivative of a Gaussian, the symmetry point was determined, and the stage was moved so that the symmetry point was centered under the laser. Once the bead was centered via the stage under one laser, the 2nd laser was centered on top of the bead via the PZT mirror moving the 2nd laser. The alignment was similar to that via the stage, except now the 2nd beam was moved over the bead while the stage remained motionless, and the beam was moved so that the symmetry point was under the center of the beam. Through these centering routines, one or more lasers were centered over a bead and/or aligned with another laser.

2.4.5 Axial alignment by minimizing crosstalk

The vertical alignment of the lasers within the microscope and detection system was the next step in alignment. To characterize this alignment, we performed axial (z) scans of

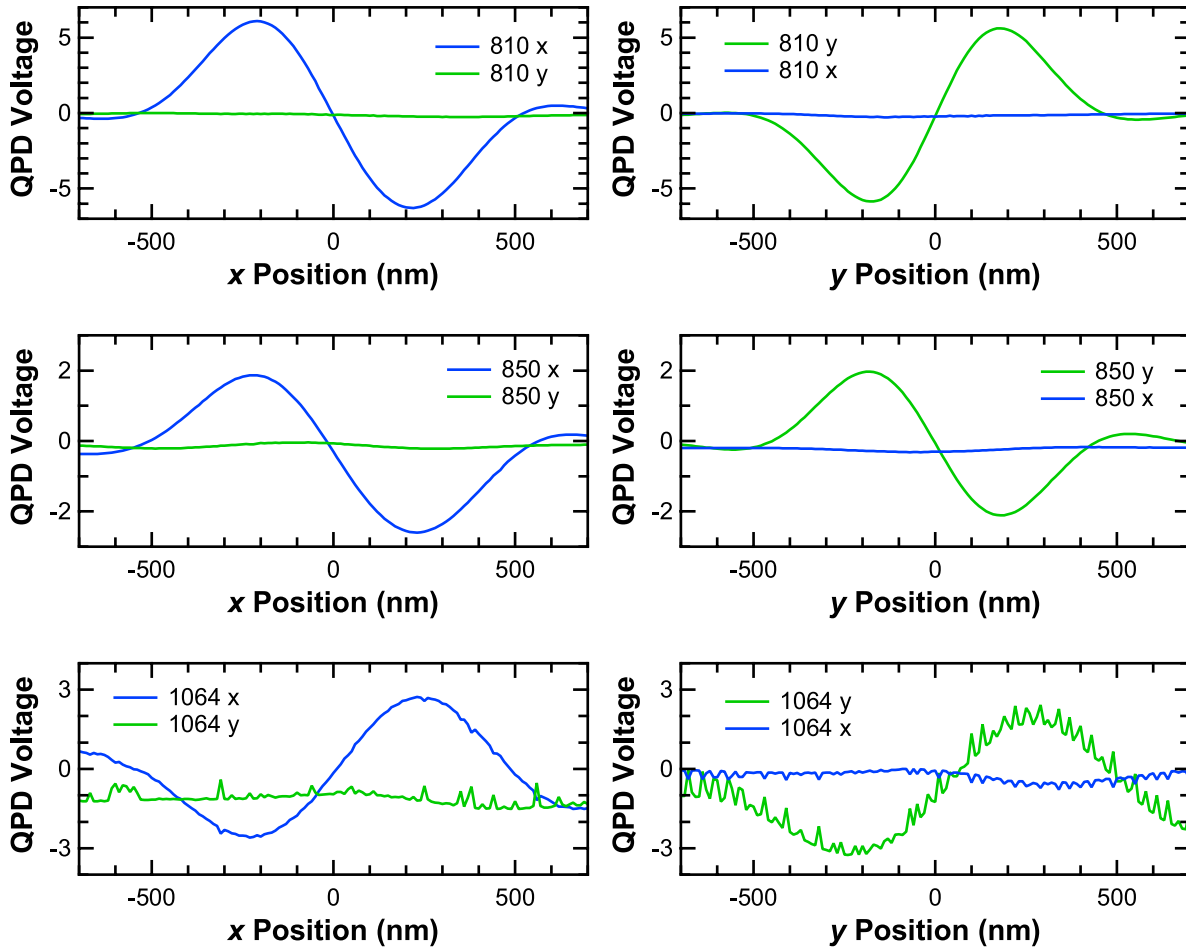


Figure 2.9: x , y scans. The x (blue) and y (green) QPD voltage response is plotted for x and y scans of a 330 nm dia. bead through each laser. The shape of the QPD response on the axis of motion approximates the derivative of a Gaussian. The off-axis response shows little change, demonstrating the alignment of the QPD axes with the stage axes. The plots of the 1064 laser show the noise problems associated with the 1064 laser in our system. Note that this noise is not evident in the x and y power spectra of trapped beads detected via the detection lasers (data not shown), and thus appears not to hinder our measurements via the detections lasers.

a stuck bead through the lasers via the stage (see Fig. 2.10). Optimum vertical alignment occurred when the x and y crosstalk-signal amplitudes were minimized. This alignment was typically adjusted by moving the 3D translation stage holding the fiber mount. However, other optics in the system may also affect this alignment, including optics in the detector arm itself.

2.4.6 2nd-order focal-plane alignment: Aligning axial detection signals

Next in the alignment process came the relative alignment of the foci of the three lasers. As mentioned previously, the 1st-order alignment of the foci was performed using visualization of the laser spots on the CCD camera (all three laser spots were made visible at approximately the imaging plane of the microscope). In this step, a more precise 2nd-order alignment was performed by scanning a stuck bead through multiple lasers simultaneously using the stage. First the lasers were precisely aligned with each other in x and y and centered over a bead. Once the lasers were aligned in x and y over the bead, the bead was scanned in z via the piezo stage and the axial signals were recorded. Characterization of these signals is shown in Fig. 2.11. To align the foci, the inflection points of the axial signals were aligned. Again, this alignment was typically adjusted by moving the fiber tip in the fiber-exit launch.

2.4.7 Minimizing trap degradation with depth by eliminating slope of axial voltage oscillations

The positions of the laser foci were governed by the laser collimation. Another important impact of the laser collimation for the trapping laser was the trap quality. The trap quality is optimum at the coverslip surface. When the trap is moved further into the sample, the trap is degraded due to spherical aberrations. This degradation is inevitable, but seems to be minimized by adjusting the laser collimation. A true test of this effect is to test the trap stiffness as a function of height, which we show later, but at this point in the alignment

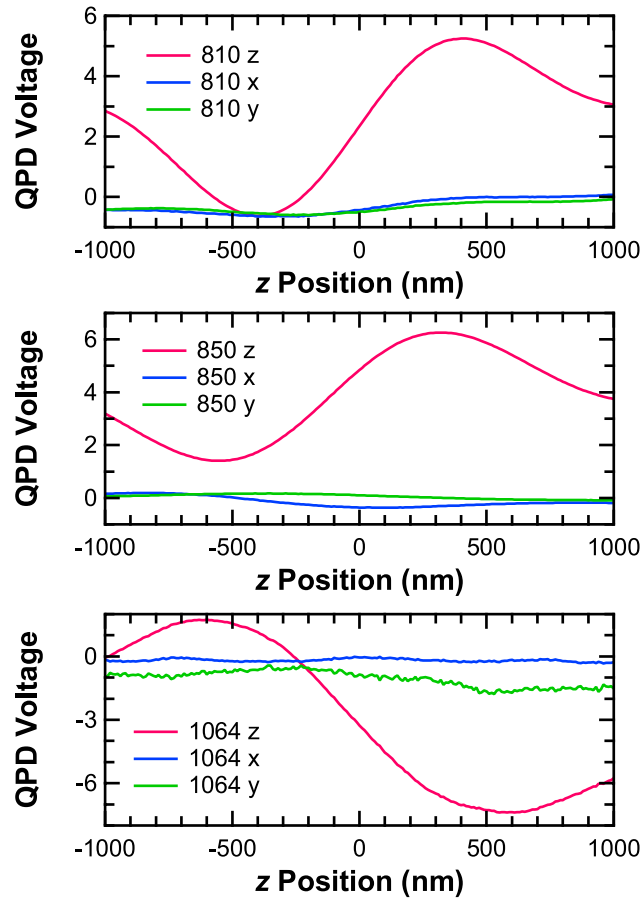


Figure 2.10: z scans with x , y crosstalk. The x (*blue*), y (*green*), and z (*red*) QPD voltage response is plotted for z scans of a 330 nm dia. bead through each laser. The shape of the axial signal is ascribed to the interference pattern that occurs as the bead passes through the focus of the laser, where a Gouy phase shift occurs [18]. The minimal changes in the voltage response of the x and y axes demonstrate the alignment between the laser path and the z axis of the stage. In other words, low crosstalk indicates the laser is vertically aligned in the microscope.

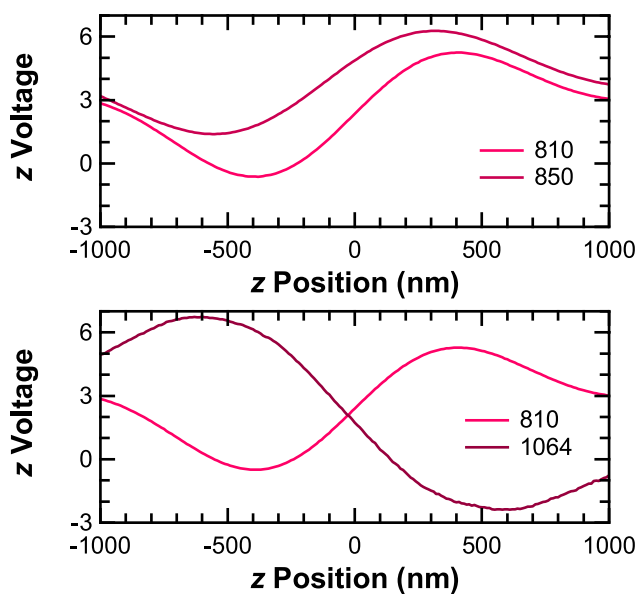


Figure 2.11: Axial scans to show relative z . The axial detection voltage is plotted for axial scans of the same bead (acquired simultaneously) for two different lasers in each plot. The relative axial alignment of the curves is an indication of the relative axial alignment of the 3 lasers. Note that these plots are also sensitive to the collimation of the laser, and thus these plots alone should not be used for optimizing the relative axial alignment of the lasers. Note: 1064 sum voltage is offset to more easily show relationship between two signals.

process, we found a quick characterization was helpful. This quick characterization involved trapping and detecting a free bead while moving the stage axially. The signal obtained is shown in Fig. 2.12. We found adjusting the collimation to make a line drawn through the oscillating region as flat as possible provided the desired laser collimation. It is also possible that collimation of the detection laser affects the flatness of this signal, though I have not verified this personally.

The iterative nature of the alignment steps becomes clear with the previous step. Here, the trap collimation was adjusted to optimize the trap quality with depth, but in order to measure the trap quality, we had to perform all of the previous alignment steps. However, in this step, if the trap collimation was changed, the trap focus position changed, and the other lasers needed to be adjusted to follow. This step is also the point where the camera was moved so that the imaging plane was coplanar with the laser foci. Once these changes were made, the axial signal of a trapped bead was checked again, to ensure the oscillations remained flat, reflecting the optimum laser collimation.

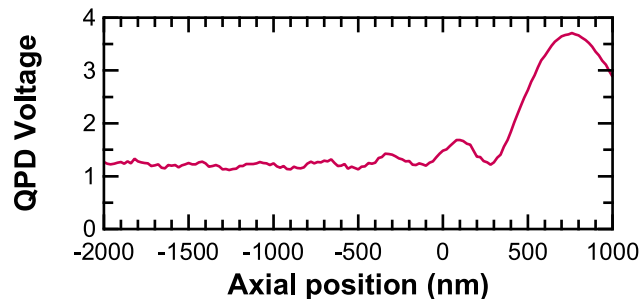


Figure 2.12: Axial scan of a trapped bead. The axial detector voltage response is plotted for a trapped bead as the stage is scanned axially. The bead was trapped by the 1064 laser. When the stage was high (+1000 nm), the bead was pushed upwards in the trap and detection lasers, above the foci. As the stage was lowered, the bead followed the stage until the bead reached the trap equilibrium point (at approximately +400 nm in this plot.) As the stage continued to be lowered, the bead remained at trap equilibrium, and the detector voltage response oscillated. This oscillation is credited to the bead-coverglass distance changing, and acting as a Fabry-Perot cavity [19]. Minimizing the slope of these oscillations is one method we use to minimize trap degradation with depth.

2.4.8 PZT-mirror calibrations

Moving from alignment characterizations to a calibration, calibration of the PZT mirrors was next in readying the instrument for precision measurements. To calibrate the PZT mirrors, voltages were applied to move the PZT mirrors such that the laser moved in a grid-like pattern. To follow the laser, a bead fixed to the sample surface was moved via the stage (which is factory calibrated with sub-nm precision). The stage precisely centered the bead under the laser at each position via the automated process previously described, and a correspondence was recorded of PZT voltages (V) to stage positions (nm). Lines were fit to each nm vs. V cross-section, and the average of the slopes of these lines yielded the $nm(V)$ calibration in x and y , as well as the crosstalk terms. A plot of this calibration is shown in Fig. 2.13. The grids represent the stage positions recorded at each laser position, thus each point on the grid also has a corresponding PZT mirror voltage. The calibrated quantities obtained include $x(nm/V)$, $y(nm/V)$, $x(nm)/y(V)$, and $y(nm)/x(V)$.

In using the PZT calibration, we accounted for both the on-axis calibration and the crosstalk using the equation

$$\Delta V_x = \frac{\Delta x(nm)/x(nm/V)}{1 - \frac{x(nm)/y(V)}{y(nm/V)} * \frac{y(nm)/x(V)}{x(nm)}}, \quad (2.1)$$

for motion requested on the x axis, and

$$\Delta V_y = -\Delta V_x * \frac{y(nm)/x(V)}{x(nm/V)} \quad (2.2)$$

to correct for the cross-talk on the y axis. Here, ΔV_x represents the change in voltage to apply to the PZT mirror in the x axis to move the requested distance, $\Delta x(nm)$. ΔV_y represents the voltage to apply in the y axis to correct for the crosstalk that will occur. By switching x and y in both these equations, motion along the y axis can be requested. With this calibration and these equations, we could precisely position the laser in our sample using the PZT mirrors.

We also verified the PZT mirror calibration to ensure the calibration was repeatable

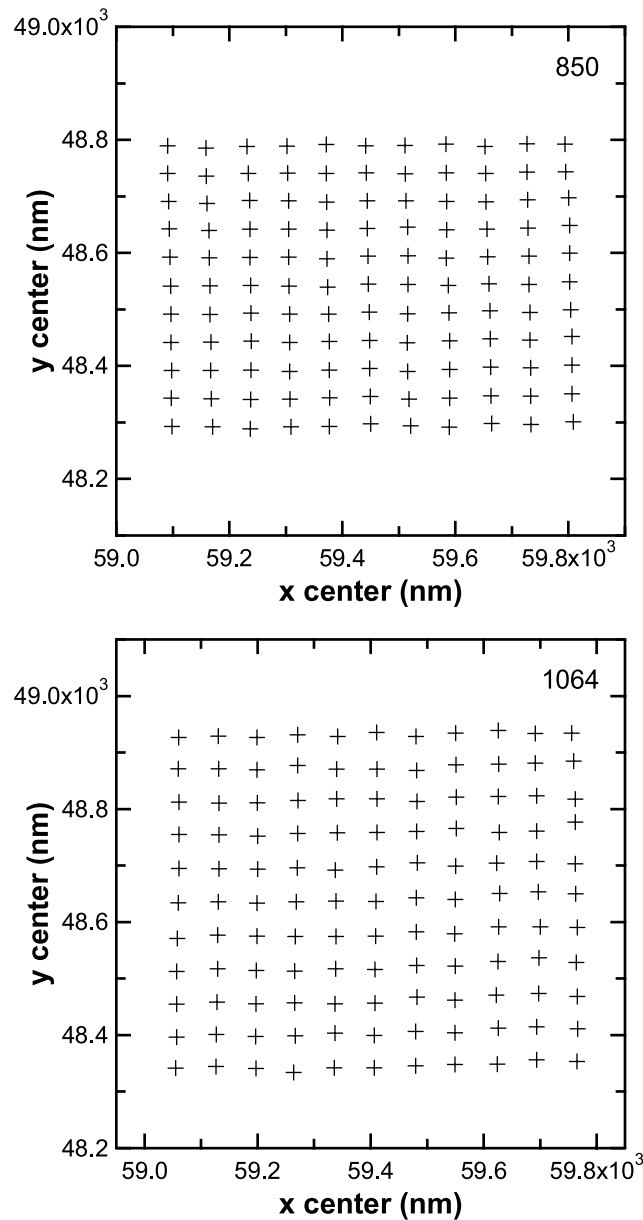


Figure 2.13: PZT mirror calibration. The laser position to PZT mirror voltage correspondence for each PZT mirror was calibrated by moving the mirrors in a grid pattern of voltages. An automated program applied the voltages (hence moving the laser) then centered a stuck bead via the stage under the laser. These x, y stage positions are plotted. Using the corresponding applied voltages, the distance moved per applied voltage (nm/V) was calculated in each axis. Crosstalk terms were also calculated.

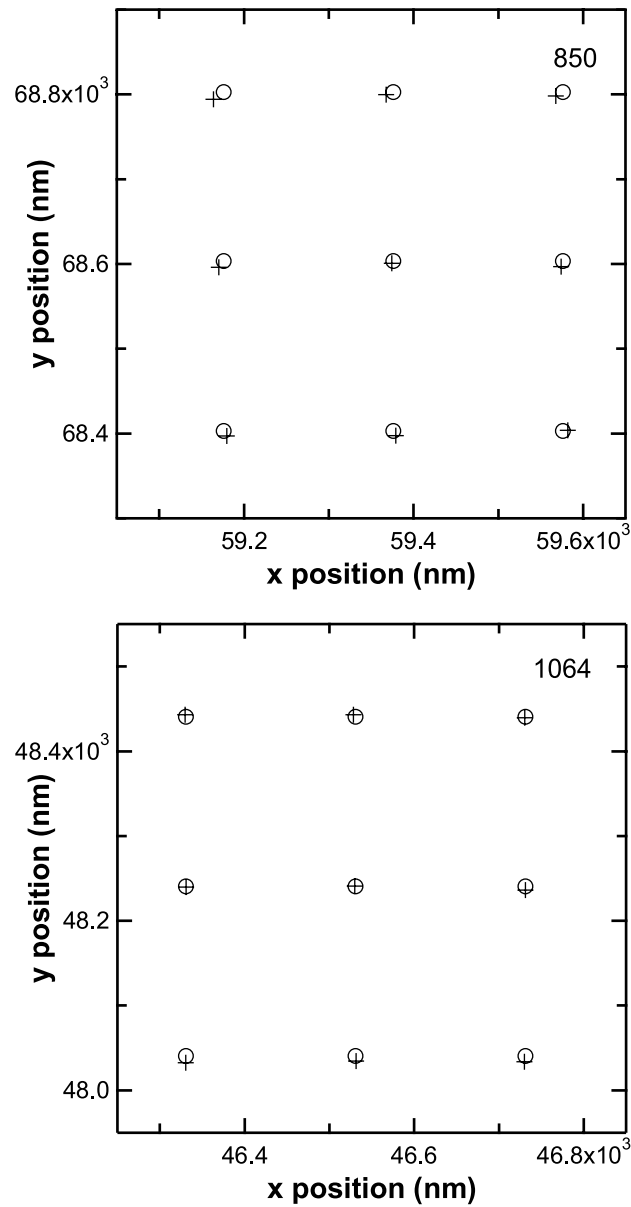


Figure 2.14: Verification of PZT mirror calibration. To check the accuracy of the PZT mirror calibrations, the calibrations were used to move the PZT mirrors in a grid-pattern of positions. A stuck bead was then centered under the laser via the stage to provide a measured position. The measured positions (*plus sign symbols*) have an average percent error of 1.9% (std. dev. 1.5%) in each axis from the requested mirror positions (*open circles*).

and that our automated software correctly read and applied the calibration. The PZT calibration verification program worked similarly to the original calibration program, but instead of moving the PZT mirror in a grid of requested voltages, the mirror was moved in a grid of requested positions, converted to voltages by the calibration described above. The stage, with a bead fixed to the sample surface, again followed the laser and precisely centered under the beam at each position. The obtained data is represented in Fig. 2.14, where the requested positions are represented by open circles, and the measured positions are represented by the plus sign symbols. The average percent error in requested vs. measured motion was 1.9%, verifying our PZT mirror calibration.

2.4.9 Detection sensitivity calibrations

Using the PZT mirror calibrations, we calibrated the detection sensitivity for a trapped bead in the x and y axes. Detection sensitivity calibrations could also be done with beads fixed to the sample surface which was useful when making measurements on stuck beads. However, obtaining the calibration of a trapped bead allowed calibration of the actual bead to be measured in the experiment at a height in the beam similar to the measurement height. For these reasons, detection sensitivity calibrations with a trapped bead provided for more precise measurements. To obtain sensitivity calibrations with a trapped bead, the bead was trapped and scanned through the detection laser in each axis using the calibrated PZT mirror. The QPD voltages in x and y were recorded and plotted vs. the requested bead position, as shown in Fig. 2.15. To obtain the desired calibration, each plot was fit to a 7th-order polynomial with the axes reversed such that a calibration function, $nm(V)$ was obtained.

For precise sensitivity calibrations, several factors were optimized. The amplitude of the voltage signal were maximized within the detection range of $\pm 10V$ using the adjustable gain on the detection electronics (custom JILA electronics). The curve was acquired such that it appeared smooth with enough data points to provide for a good fit, as in the figure.

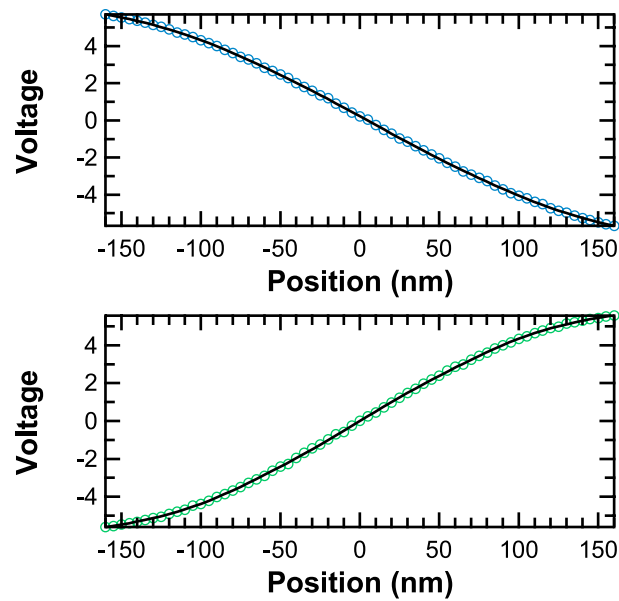


Figure 2.15: Detection sensitivity of a trapped bead. For x , y detection sensitivity calibrations of a trapped bead, the bead was trapped by the 1064 laser, then swept through the 810 detector laser using the 1064 PZT mirror. The resulting detector voltage for a 330 nm bead is plotted here (*open circles*) vs. the bead position. The x axis is shown in blue, the y axis in green. Plots like these, with the axes switched to plot position vs. voltage, were fit to a 7th order polynomial to provide the $nm(V)$ detector sensitivity calibration for each bead.

Also, the range of motion was chosen so that the curve did turn over at the maximum and minimum (as that would create a non-function when the axes are reversed). However, the range was large enough that the curve did extend to near the maximum and minimum so that the 7th-order polynomial would have real curvature to fit rather than trying to fit noise in the curve. Care was also be taken to perform these calibrations quickly to minimize drift of the system during the calibration. These sensitivity calibrations were automated in LabVIEW, with easily adjustable data acquisition parameters so that the calibration could be optimized.

Importantly, these sensitivity calibrations could also be acquired on a tethered bead. With a short tether the validity of the calibration depended on ensuring the bead was centered in the trap throughout the calibration. This was accomplished by moving the sample and the laser together during the calibration, such that the short tether did not pull the bead out of the center of the laser. Using these calibration methods, the detection sensitivity in x and y were obtained for each bead to be measured.

2.4.10 Drag measurement

Next in the steps of characterization was an essential calibration and alignment check for optical traps: the drag measurement. In the drag measurement, a bead was trapped and the sample was oscillated, creating a drag force to pull the bead out of the trap center. The drag force was calculated based on the velocity of the sample oscillations, and the bead position was measured. A drag force (F) vs. bead displacement (x) measurement is plotted in Fig. 2.16. This plot demonstrates the linearity of the trap. The slope of this plot also provided a measurement of the trap stiffness (k), since for an optical trap $F = -kx$.

2.4.11 Trap symmetry and ellipticity

Next, another important trap symmetry check was made by plotting the x and y positions of a trapped bead. A plot of x vs. time, y vs. time, and x vs. y is shown in

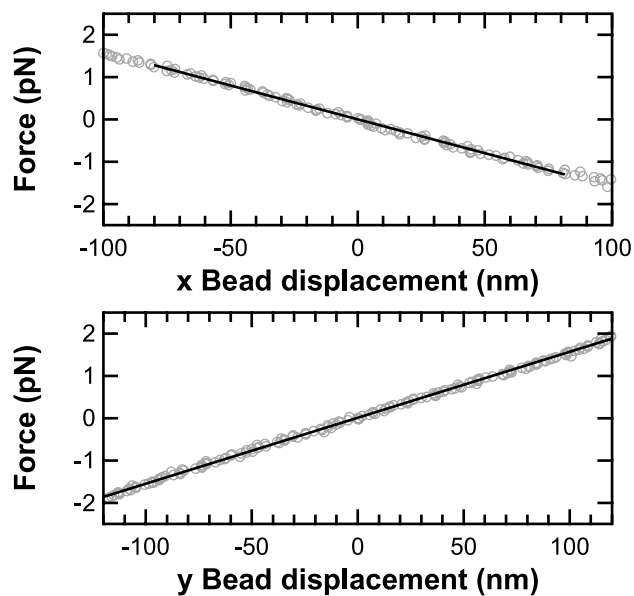


Figure 2.16: Drag-force measurement. A 330 nm bead was trapped at 1 V on the intensity servo, and the stage was oscillated to create a drag force on the bead. The force on the bead was calculated as the drag multiplied by the stage velocity. This force is plotted vs. the measured bead displacement, for x in the top plot, and y in the bottom plot. The trap stiffness at this voltage is the slope of a linear fit to these plots.

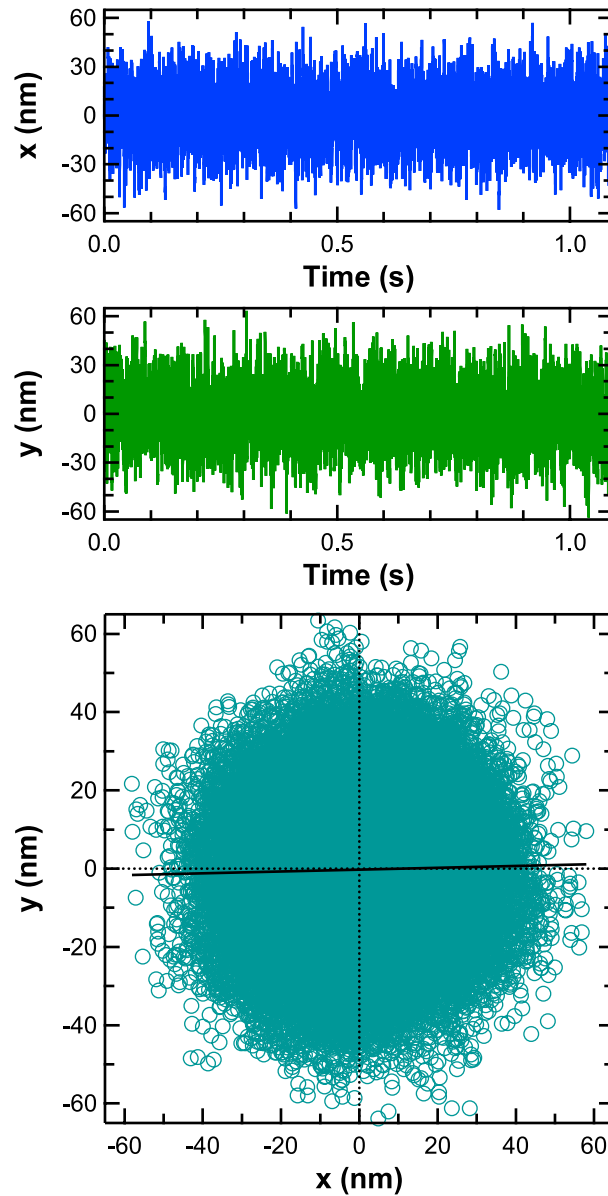


Figure 2.17: Trap ellipticity. Plots of bead position for a trapped bead. The top 2 plots shows the x and y positions of a trapped bead vs. time. At the bottom, the (x, y) position is plotted for each data point to show the shape of the optical trap. A line was fit (*black, solid*) to find the slope of an ellipticity of the trap shape. The slope for this fit was 0.02. The average slope for 5 plots with voltages 1-5 V was 0.0053.

Fig. 2.17. Typically the x vs. y plot for a trap is somewhat elliptical, and for simplification of calibrations and measurements, the axes of this ellipse should align with the x and y detection axes. To determine the ellipse axes, we fit the x vs. y plot to a line. The slope of the line represents one axis of the ellipse. The mean slope from fitting 5 plots was 0.0053. This close alignment with the detection axes was accomplished by tuning the post-fiber half-wave plate in the pre-microscope optics. This measurement ensured the trap ellipse was aligned with the detection axes and that the general shape of the trap was symmetric.

2.4.12 Axial alignment by sensitivity offset vs. height

Next was a third and final characterization and optimization of the axial positions and alignment of our lasers. For this characterization, we scanned beads on short DNA-tethers through the trapping and detection lasers. We scanned the tethered beads in x and y at a series of axial positions, obtaining sensitivity calibrations at each axial position. As a characterization of the axial alignment, we plotted the offset term (a_0) vs. stage height (z_{stage}). A flat a_0 vs. height curve represented an optimally vertical trap. Fig. 2.18 shows the a_0 terms in x and y for our instrument.

2.4.13 3rd-order focal-plane alignment: Optimizing xy-sensitivity vs. height

For a final optimization of the axial position of the detection laser foci relative to the trap position, we plotted the first-order term (a_1) of the 7th-order polynomial x and y detection sensitivity calibration curves. The a_1 sensitivity term was roughly parabolic as a function of height, with a flat peak near the laser focus, and with decreased sensitivity further from the focus. For precision in our experiment, we wanted to ensure that when we performed a sensitivity calibration of a trapped bead, the calibrated sensitivity would be the same as when we actually performed our measurements. Typically, sensitivity calibrations occurred with the bead near trap equilibrium. Measurements were performed with the bead pulled down in the trap (to exert force), below trap equilibrium. To optimize the precision

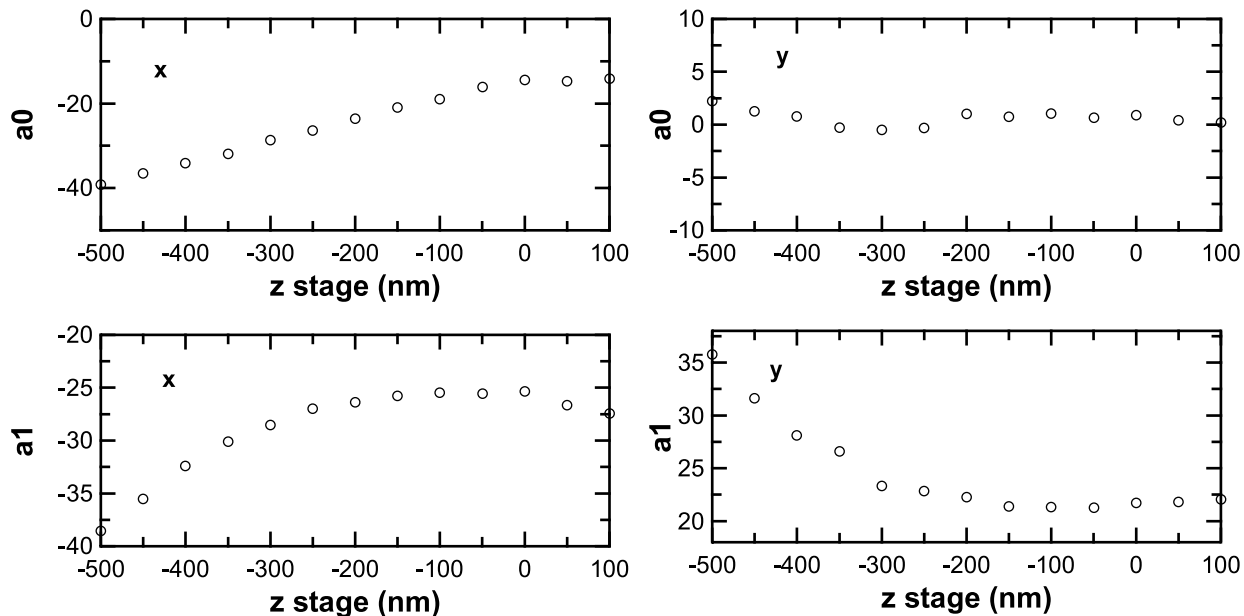


Figure 2.18: Sensitivity vs. z . The x and y detector sensitivity, $nm(V)$, was obtained for a bead on a short tether at several different heights. The sensitivity at each height was fit to a 7th order polynomial. Here, the a_0 and a_1 terms are plotted for each height for the x and y axes. The flatness of the a_0 terms as a function of height (*top*) indicates the vertical alignment of the lasers, detectors and piezo stage axes. The a_1 terms (*bottom*) represent the steepness of the slope of the sensitivity curves. For accurate sensitivity calibrations, the final measurement should occur at a height with similar sensitivity to the calibration height. We satisfy this requirement by setting the focus of the detection laser such that a bead traps at the high end of the flat region during calibration, and at the low end of the flat region during the measurement. z stage = 0 is the approximate stage position where the tethered bead is sitting at trap equilibrium. At z stage > 0 , the stage is pushing the bead up in the trap, and at z stage < 0 , the stage is pulling the tethered bead down from trap equilibrium.

of our measurements, we moved the detection laser focus such that the trap equilibrium point occurred near the top of the flat-peak region of the a_1 vs. height curve. Thus when we calibrated at trap equilibrium and when we measured slightly below trap equilibrium, the calibration would be as valid as possible. Fig. 2.18 shows a_1 as a function of height in our instrument.

2.4.14 Laser power measurements

Measurements of laser power were intrinsically important, as well as providing diagnostic tools for checking instrument functionality. We measured laser power at several points in the beam path, using both photodiodes and a power meter (see Tables 2.4 and 2.5). The in-loop photodiodes (which sampled each beam just after the optical fiber) provided a good reference voltage for a properly functioning instrument. As another reference, we also measured the power via the QPD sum voltage. Both these sets of photodiodes provided quick reference voltages to ensure the instrument was behaving consistently from day-to-day. We also obtained true measurements of the power via a power meter placed just before the microscope (between the last two pre-microscope lenses). From this power measurement, we estimated the power at the sample plane within the microscope.

Table 2.4: Detector voltages without servos.

Laser ^a	VAOM ^b (V)	QPD sum ^c (V)	In-loop PD (V)
1064	0.4	-1.92	7.72
850	0.35	0.4	0.76
810	0.3	0.648	0.485

^a with typical laser settings from Table 2.3.

^b Voltage directly from computer to AOMs, bypassing servos.

^c with no bead in beampath

The power at the sample plane (P_{sample}) was calculated from the power measured

Table 2.5: Laser Power with servos on.

Laser ^a	QPD sum ^b (V)	In-loop PD (V)	pre-microscope ^c (mW)	At sample plane ^d (mW)
1064	-1.03 ^e	3.963	421.3	146.6
850	0.367	0.675	0.313	0.173
810	0.721	0.518	0.516	0.290

^a with typical laser settings from Table 2.3, except as noted.

^b with no bead in beam path

^c Measured between last two lenses before microscope.

^d Calculated as described in the text.

^e at 1064 V_{servo} = -3.87 V

between the two lenses before the microscope ($P_{premicroscope}$) as follows

$$P_{sample} = P_{premicroscope} * T_{lens} * T_{dichroic} * T_{objective} (*T_{overflow}), \quad (2.3)$$

where T is the transmission coefficient for each component. The subscripts for each transmission coefficient correspond as follows: *lens* - last lens before the microscope (Linos NIR Doublet), *dichroic* - the dichroic in the base of the microscope (Chroma), *objective* - the microscope objective (CFI Plan Apochromat 100x oil IR). For the trapping laser (1064), the laser overfills the objective back aperture, leading to an additional transmission coefficient multiplier with subscript *overflow* - the overflow factor. We estimated the transmission coefficients for each component and used the above equation to calculate the final power at the sample plane listed in Table 2.5.

Estimates for the transmission coefficients came from various sources. We used estimates from the manufacturers for the lens and dichroic: $T_{lens} = 0.96$, and $T_{dichroic} = 0.96$. We estimated the wavelength dependent $T_{objective}$ as 0.59 for the 1064, 0.60 for the 850, and 0.61 for the 810 [13]. For $T_{overflow}$, we calculated the transmission coefficient by measuring the diameters of our Gaussian beams and calculating the transmission through the objective back aperture diameter (5 mm). The beam diameters at the point where the intensity had decreased to $1/e$ of the maximum intensity were 4.5 mm for the 810 and 850 lasers and 7 mm for the 1064 laser. We estimated $T_{overflow}$ as follows: 1 for the 810 and 850, and 0.64 for

the 1064. Details of the calculation are below.

To calculate $T_{overfill}$, we assumed a Gaussian intensity profile (I) in cylindrical coordinates, $I = A * exp(-(p/w)^2)$, where A is the amplitude, p is the radial cylindrical coordinate, and w is the A/e beam radius. The power P within a radius R is given by

$$P_R = \int_0^{2\pi} \int_0^R I(p, w) p dp dw = \pi * A * w^2 (1 - exp(-(R/w)^2)) \quad (2.4)$$

The total power, evaluated at $R = \infty$, is then $P_{total} = \pi * A * w^2$. Substituting into the equation above:

$$P_R = P_{total} * (1 - exp(-(R/w)^2)) \quad (2.5)$$

Using this equation we calculated the transmission of the 1064 laser through the back aperture of our objective ($R = 2.5$ mm), using $w = 3.5/sqrt(2)$ for our 1064 laser with an A/e^2 radius of 3.5 mm. We found the power within a radius of 2.5 mm, $P_{2.5} = P_{total} * 0.64$, i.e. $T_{overfill} = 0.64$ for the 1064 laser.

Following the above methodology, we measured $P_{sample} = 146.6mW$ at a servo voltage (V_{servo}) of 4 V. Generalizing this measurement to provide the relationship between V_{servo} and P_{sample} , we obtain $P_{sample} = 36.65(mW/V) * V_{servo}$.

2.4.15 Trap stiffness calibrations

After the previous careful alignment and calibration procedures, we were ready to perform our trap stiffness calibrations. We calibrated the trap stiffness by three different methods, equipartition theorem (EQP), power-spectral density (PSD), and drag. In the EQP method, $\frac{1}{2}k_B T = \frac{1}{2}k_{trap} \langle x^2 \rangle$, where $k_B T$ represents the thermal energy (4.1 pNm at room temperature), k_{trap} is the trap stiffness in a single axis, and $\langle x^2 \rangle$ is the variance in the position of a trapped bead. In the PSD method, the power spectrum of a trapped bead is recorded and fit to a Lorentzian. The trap stiffness is calculated by $k_{trap} = 2\pi\gamma f_0$ where γ is the drag coefficient and f_0 is the corner frequency of the Lorentzian fit. γ for a bead in fluid is given by $\gamma = 6\pi\eta r_{bd}$ where η is the fluid viscosity (0.001kPa * s for water at room

temperature) and r_{bd} is the bead radius. Because most trapping is done near the sample surface, the drag coefficient must be corrected using Faxen's Law [13]. The drag measurement provided the third method of trap stiffness calibration, and has been previously discussed. These three methods provided independent means of calibrating the trap stiffness.

With automated stiffness calibration programs in LabVIEW, we acquired simultaneous acquisition of the PSD and EQP stiffness calibrations for several different trap powers. We typically acquired these calibrations on 5-10 beads, and an average calibration from these beads was calculated. For drag, typically one set of measurements over a similar power range was acquired as a confirmation of the EQP and PSD measurements. Plots of the stiffness calibrations for our instrument are shown in Fig. 2.19. Agreement between the three methods was better than 5%. The k_{trap} calibrations were valid for months at a time, typically only needing to be redone if a change was made in the instrument.

Besides providing stiffness calibrations, these measurements also provide a diagnostic check of overall instrumental quality [20]. If all three trap stiffness calibrations agree, the trap is performing according to physical theory, which increases the likelihood that the alignment is excellent; assumptions about height, temperature, and viscosity are correct; and PZT and detector calibrations are working as they should. If the three methods do not agree, something about the instrumentation or the assumptions is not correct.

We also verified the stiffness calibrations and the software that would use the stiffness calibrations. We used the above stiffness calibrations to request a stiffness, then measured the stiffness, again by EQP and PSD. This verification is shown in Fig. 2.20. We obtained a mean percent error of 5.8%.

2.4.16 Stability characterizations

Because instrumental stability was of utmost importance in our measurements, we also characterized the final stability. We actively stabilized the instrument on a bead stuck to the sample surface and measured the residual noise with the other detection laser. We measured

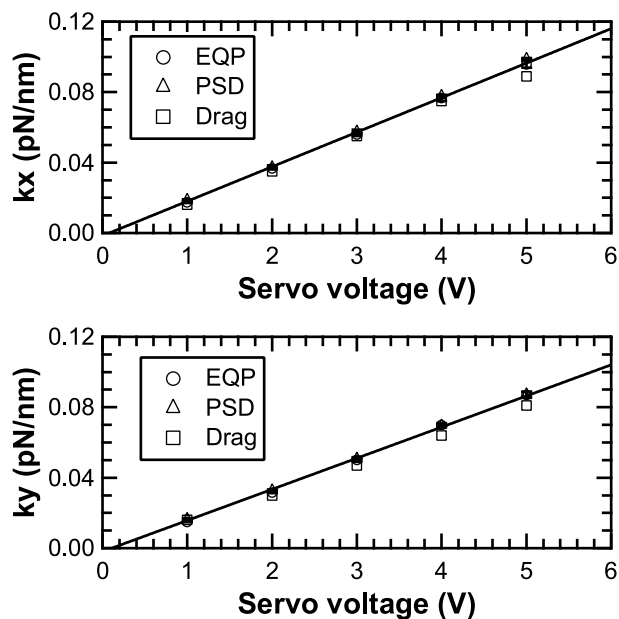


Figure 2.19: Stiffness calibration. The trap stiffness was measured by three different methods, equipartition theorem (EQP), power spectral density (PSD) and drag. The measured stiffness is plotted vs. the applied servo voltage. For EQP and PSD, the data points represent the mean measurements on 5 different beads, with error bars representing the standard error. For drag, the data points represent 1 measurement at each voltage. The line shown represents the calibration used during subsequent data acquisition. This calibration was obtained by fitting the servo voltage as a function of the trap stiffness for EQP and PSD separately, then averaging the obtained slopes and intercepts.

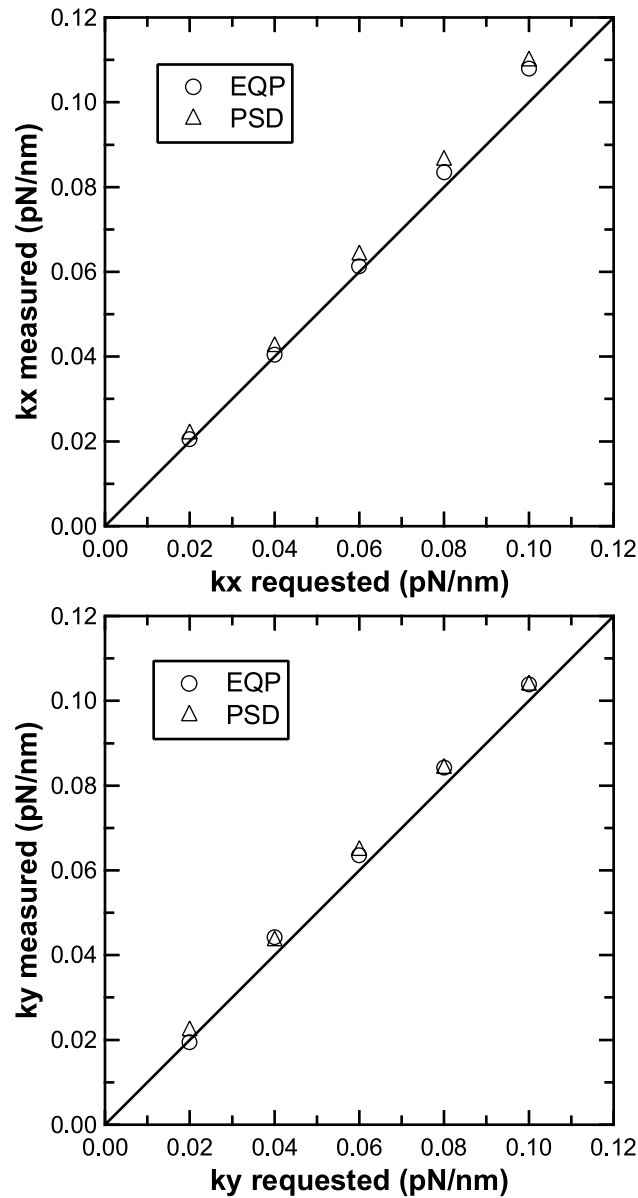


Figure 2.20: Verification of stiffness calibration. To check the stiffness calibration, k_x and k_y were requested and set via the stiffness calibration. The experimental stiffness was measured with the equipartition theorem (EQP) and the power spectral density (PSD) as described in the text. The line in the plots is drawn through the values that would indicate a perfect match between requested and measured stiffness; the markers show the actual measured values. The mean percent error for the measured values was 5.8%.

on the same bead (Fig. 2.21), and on a separate bead (Fig. 2.22). We obtained excellent stability for both the single bead (means of 17 traces, integrated noise in x, y, z of 0.13, 0.063, 0.092, $\Delta f = 0.03$ -2.5 Hz) and the separate bead measurements (means of 8 traces, integrated noise in x, y, z of 0.14, 0.067, 0.10, $\Delta f = 0.03$ -2.5 Hz) as is demonstrated by the position vs. time plots, the PSD plots, and the integrated noise plots (the PSD noise integrated up to each frequency).

When characterizing and optimizing the stability, a few recurring factors tended to impact the stability. Very noisy traces with large (>2 nm) jumps tend to be caused by loose or bad cables and connectors. Replacing or stabilizing these cables and connectors was essential for instrumental stability. Instability can also be caused by the servo electronics themselves, either by failure to optimize the servo electronics, or electronics that may fail over time. Another common culprit of instability is failed or mal-adjusted cable and fiber stabilizers. These should be firmly stabilized, but without pulling or torquing. Finally, the floating table is very important to stability; if the table runs out of air, the noise increases dramatically. Though many other factors can cause noise, these factors tended to be the most common culprits of increased instrumental noise.

2.4.17 Force vs. extension for DNA

As a final check of the instrumental alignment and calibrations, we obtained force vs. extension curves of DNA. We stretched 2013 nm DNA in the x and y axes, obtaining curves like those shown in Fig. 2.23. We obtained 6 traces (on 3 molecules). We calculated the geometry-corrected force and extension [21] and fit the curves to a modified worm-like chain [22]. The average persistence length was 42 nm, and the average contour length was 2060 nm. The accepted value for the persistence length for this DNA was 45-50 nm [[23, 24, 21, 22, 25]], and the accepted contour length was 2013 nm. These numbers provided a reference estimation for the measurement uncertainties that remain in our instrument.

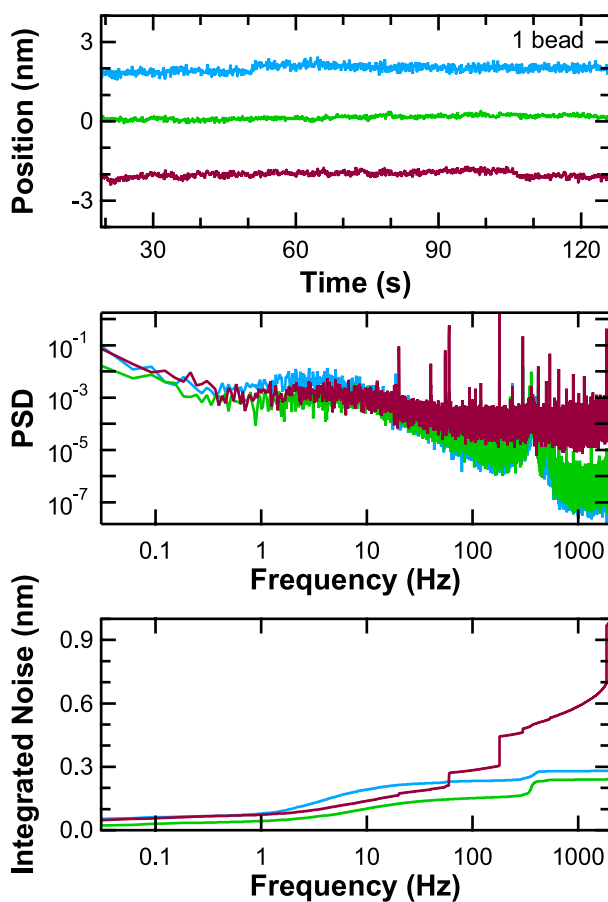


Figure 2.21: Stability of stuck beads - 1 bead. The x (*blue*), y (*green*), and z (*red*) residual noise during active stabilization are plotted. Both detection lasers were aligned on the same 490 nm dia. bead. One laser actively stabilized the position signals while the second laser monitored the residual noise. The top plot displays the x , y , and z position trace vs. time, smoothed to 5 pts/sec. The middle plot shows the calculated power spectral density (PSD) vs. frequency. The bottom plot shows the integrated noise vs. frequency. These traces most closely represented the mean noise from 17 individual traces (13 different beads).

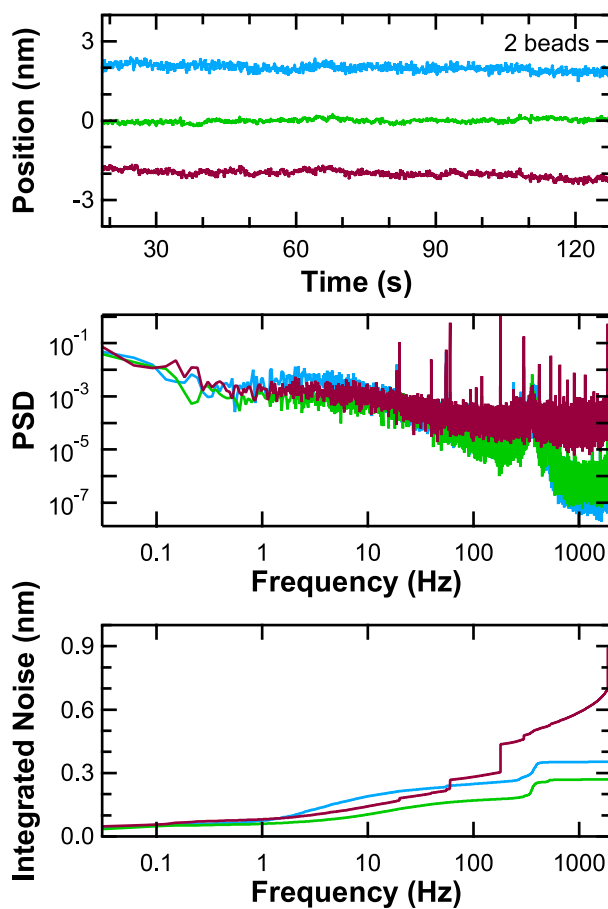


Figure 2.22: Stability of stuck beads - 2 beads. The x (*blue*), y (*green*), and z (*red*) residual noise during active stabilization are plotted. Each detection laser was aligned on a different 490 nm (dia.) bead. One laser actively stabilized the position signals while the second laser monitored the residual noise. The top plot displays the x , y , and z position vs. time, smoothed to 5 pts/sec. The middle plot shows the calculated power spectral density (PSD) vs. frequency. The bottom plot shows the integrated noise vs. frequency. These traces most closely represented the mean noise from 8 individual traces (8 different pairs of beads).

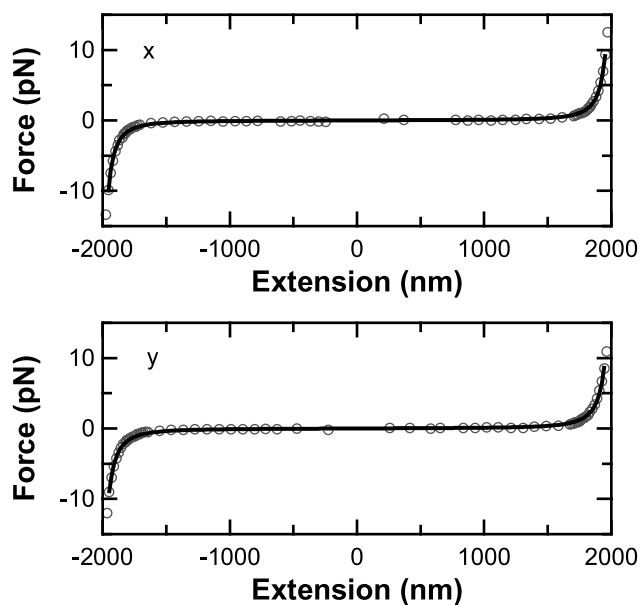


Figure 2.23: DNA force vs. extension. The force vs. extension curves for 2013 nm DNA. A 330 nm dia. bead was tethered to the coverslip surface via 2013 nm DNA. The DNA was stretched in the positive and negative directions in the x and y axes. The geometry corrected force and extension were calculated from the bead and stage positions and the calibrated stiffness [21]. The curves were fit to a modified worm-like-chain model [22], which returned a persistence length (P) and contour length (L) for each trace. For 6 traces (on 3 molecules), the means were $P = 42$ nm and $L = 2060$ nm. The traces shown most closely matched the means.

2.5 SAMPLE PREPARATION

For studying TBP bending DNA, several sample preparations were necessary. For many instrumental calibrations and characterizations, we prepared samples with beads fixed to the coverslip surface. For TBP experiments, to prevent protein sticking to the surface, we prepared samples with customized polyethylene glycol (PEG) surfaces. We fixed beads to these PEG surfaces to enable stabilization, and we attached DNA tethers to these surfaces to study TBP bending the DNA. For the TBP experiments, the protein was very sensitive to conditions (time, temperature, pipetting, storage buffer). This section details the sample preparations and protein handling used in acquiring the data in this thesis.

2.5.1 Cleaning coverslips and slides

Cleaning the microscope coverslips (and sometimes slides) was essential for most of our sample preparations. We cleaned by two different processes: KOH cleaning and plasma cleaning. Sometimes both processes were used, other times only one process was used.

For KOH cleaning, we soaked slides and coverslips for 3 minutes in 5.7 M KOH (Mallinckrodt) in ethyl alcohol (Mallinckrodt, Completely Denatured) solution while sonicating in a bath sonicator (Bransonic Ultrasonic Cleaner 5200). (Note: KOH solution is extremely caustic and must be handled with care.) We rinsed with two 3-minute soaks in beakers of double filtered, double deionized water (diH₂O), also placed in the bath sonicator. After each soak, we also rinsed with diH₂O from a squirt bottle. We performed a final rinse with ethyl alcohol. We dried the slides and coverslips by placing them in a microwave oven for 1.5 minutes. We placed the slides and coverslips in closed containers to preserve cleanliness.

For plasma cleaning, we cleaned slides and coverslips with oxygen plasma in a Reactive Ion Etch (RIE, PlasmaSTAR AXIC). The slides and coverslips were placed in a metal holder in the RIE. An automated program pumped the system down to vacuum ($<10\text{mT}$), then

pumped in O_2 . A voltage was applied to create the oxygen plasma for 180 s. Then the chamber was pumped down to vacuum again to remove the impurities. In detail, the mass flow controller was set to 100 sccm, the Power to 550 V, the runtime to 180 sec, and the venting to 1x. The automated program is titled "Amandaash" on the Keck Lab RIE at JILA, and the settings should be listed as MFC2 Setpoint 100 sccm, Power 550 W, Runtime 180 s, Vent 1x. After plasma cleaning for 180 s, the metal holder was rotated and the process repeated to clean for another 180 s. Again, the slides and coverslips were stored in closed containers to preserve cleanliness.

2.5.2 Flow cells

All samples were assembled on clean flow cells. A flow cell consisted of a microscope coverslip (Corning No. 1 1/2, 22 x 40 mm) fixed to a slide (Corning Micro Slides plain 2947, Pre-Cleaned, 75 x 25 mm) with double-sided tape (3M Scotch Permanent Double-Sided Tape, 136, 1/2 in. wide) and 5-minute epoxy (Devcon). The tape was sliced in half along the length, and each half of the tape was placed near the center of the slide, leaving an ~ 5 mm channel between the two tape halves running across the slide along the narrow dimension. The coverslip was then fixed to the slide such that the long dimension of the coverslip was perpendicular to the long dimension of the slide. Pressing the coverslip into the tape provides added stability. Five minute epoxy was then mixed and quickly applied along the edges of the coverslip. The fluid epoxy flowed into the space between the slide and coverslip, providing added stability. Once this seepage occurred, additional epoxy was applied to the four corners where the slide and coverslip are joined. The edges of the coverslip overhang the slide, conveniently allowing for fluid to be pipetted through the flow cell.

2.5.3 Antidigoxegenin modification of beads

For many DNA-tethering experiments, we modified latex beads (Invitrogen/Interfacial Dynamics/Molecular Probes Surfactant-Free White Aldehyde/Sulfate Latex) by attaching

antidigoxigenin. To modify these beads, we started by passivating two 1.5 mL plastic tubes for 2 hours with 1.2 mL 2 mg/ml acetylated BSA (acBSA) in PBS buffer. The tubes were rinsed twice with diH₂O and drained, and one tube was used during the protocol, while one was set aside at 4°C to be used for storage of the final modified beads.

For many steps in the bead modification process, the bead size and concentration impacts choices of centrifuge speeds and times and amounts of other reagents added. I most commonly used 330 nm dia. beads, so all times, speeds, and amounts in parentheses are specific to this bead size. In the protocol tube, we washed latex beads (200 μ L of 4.2% w/v for 330 nm beads) 4x in 1 mL PBS buffer (centrifuge for 5 min. at 12krpm to form a pellet, remove supernatant, resuspend in 1 mL PBS and pipette and vortex to suspend). After washing, we resuspended the beads in 500 uL PBS buffer and added acBSA (15 μ L of 80 mg/ml acBSA). We sonicated for 40 min. or more until beads were separated. Next, we added anti-digoxigenin fab fragments to the beads (1 mg anti-Dig in 500 uL PBS), mixed by pipetting, and incubated on a rotator (>24 hours). After this incubation, we centrifuged the beads to form a pellet (6 min. at 12 krpm), removed the supernatant, and re-suspended them in 1.2 mL 1.0 M glycine in PBS, incubating for 40 min. on a rotator to quench the reaction. Next we centrifuged again to form a pellet (6 min. at 12krpm) and removed the supernatant. We performed the final resuspension in PBS (1350 uL PBS) plus 40 μ L of 80 mg/mL acBSA and 2% (w/v) sodium-azide, to form the final solution (0.5 nM for 330 nm beads). The final, modified-bead solution was transferred to the other acBSA-passivated tube. These antidigoxigenin beads were used in most of the sample preparations for my experiments.

2.5.4 Stuck beads

For calibrating and characterizing the instrument, samples with beads fixed to the coverslip surface were used. For preparation of these samples, we started with epoxied flow cells with KOH and/or plasma cleaned coverslips. We flowed 20 μ L of 25 pM beads diluted in

diH₂O into the flow cell. We used several types of beads, including anti-digoxigenin-modified latex beads (Surfactant-Free White Aldehyde/Sulfate Latex, with custom anti-digoxigenin modifications by our lab) and Streptavidin-modified polystyrene beads (Spherotech, Sphero-Streptavidin- Polystyrene Particles). The bead sizes varied from 330 nm dia. to 860 nm dia. We then washed the flow cell with 20 μ L SB buffer (10 mM Tris pH 7.5, 250 mM KCl, 20 mM MgCl₂). Next we washed with 200 μ L SWB buffer (10 mM Tris pH 7.5, 100 mM MgCl₂), then with 200 μ L ethyl alcohol (Completely Denatured, Mallinckrodt). Finally, we washed with 2 mL of diH₂O. These salt-stuck beads were well-fixed to the sample surface (see stability data in Fig. 2.22), even without a baking step, as is often used to melt the beads onto the glass. We preferred not to use the baking/melting step so that we could preserve the bead shape, which was important for some calibrations and characterizations. Stuck bead samples used in these characterizations were often filled with diH₂O, buffer or sometimes free beads (\sim 0.5 pM) in buffer.

Stuck bead samples could often be reused. If the sample became sticky to free beads, we often flushed the sample with doubly-distilled methanol followed by 2 mL diH₂O. Sometimes we added BSA to these samples to prevent stickiness.

2.5.5 PEG-modification of surfaces

For TBP experiments, non-stick surfaces were essential to preventing the protein from sticking to the coverslip surface. A common solution to protein-sticking problems is to implement polyethylene glycol (PEG) surfaces [26]. Protocols for PEG-coating surfaces available in the literature proved unsuitable for creating a consistently non-stick surface for our experiments, so we developed a customized protocol for covalently attaching PEG molecules to our slide and coverslip surfaces.

The first step in covalently attaching PEG to our surfaces was aminosilanization. As a starting point for aminosilanization, clean glass is essential. We cleaned the slides and coverslips first by plasma, then by KOH, either the day-of or day before the PEGylation protocol

(see Section 2.5.1 for details). We also cleaned the reaction containers for aminosilanization by performing the KOH cleaning procedure on the slides and coverslips in the same containers as would be used for the aminosilanization, hence KOH-cleaning the containers as well as the slides and coverslips. The containers used for cleaning and aminosilanization of the coverslips were 1 L glass beakers for each set of 10 coverslips, with the coverslips held in a custom-made Teflon basket with a Teflon handle. The containers for the slides were commercially available glass containers typically used for microscope slide staining, with the slides held in an accompanying glass basket with a metal handle (to prevent reactions with the metal, we removed the handles during the cleaning and aminosilanization, only attaching them when the baskets were being moved). A final rinse with methanol on the day of PEGylation completed the preparation of all the glassware. Cleaning the reaction containers and other glassware after aminosilanization was also important, because glassware will itself be aminosilanated. We cleaned after aminosilanization with methanol, followed by diH₂O, followed by 1M KOH, followed by plenty of diH₂O.

The aminopropylsilane (N-(2-Aminoethyl)-3-Aminopropyltrimethoxysilane (UCT A0700)) is highly sensitive to air, moisture, and light, all which cause degradation of the chemical. To prevent degradation, we stored the aminopropylsilane in a vacuum sealed bag (vacuum sealed using a Food-Saver device) at -20°C, and allowed the aminopropylsilane to warm to room temperature in the dark for 2 hrs before opening to air. Immediately after use, we re-sealed the aminopropylsilane in a vacuum bag and placed at -20°C.

To aminosilanate our slides and coverslips, we incubated them in a well-mixed 2% aminopropyl silane-methanol solution (prepared with a glass pipette, in a glass container, mixed with a glass stir-rod). Total incubation time was 21 minutes: 10 minutes followed by 1 minute invigoration in the bath sonicator, followed by 10 more minutes. We then rinsed with 2 methanol baths, also rinsing with methanol from a squirt bottle after each bath. Finally, to crosslink the aminosilanated surfaces, we baked at 110°C for 5-10 min. The aminosilanated slides and coverslips were assembled into flow cells with no epoxy. (Epoxy may outgas during

storage, which is undesirable, and the epoxy may weaken or become brittle over time, so epoxying was done just before using the final PEGylated samples.)

After assembling the aminosilanated samples, we covalently attached the PEG molecules. For samples to be used for DNA-tethering, we attached an ~60:1 ratio mix of methoxy-PEG (mPEG) and biotinylated-PEG (bio-PEG) molecules, so that we could later specifically attach streptavidin and biotinylated-DNA molecules to the surface while maintaining a non-stick surface. Like the aminopropylsilane, the PEG is sensitive to light, air, and moisture, and was thus treated similarly to the aminopropyl silane, i.e. stored under vacuum at -20°C , allowed to equilibrate to room temperature in the dark for 2 hours before opening to air, and quickly returned to vacuum and -20°C after use.

We dissolved the PEG in 0.1 M sodium bicarbonate buffer. The PEGylation process is pH sensitive, and the pH of the sodium bicarbonate solution is time sensitive, so the sodium bicarbonate was made within a few hours of the PEGylation process. To dissolve the PEG, we mixed by vortexing at half-max, then centrifuged at 10,000 rpm for 1 min. We then pipetted carefully, ~100x, being careful to form no bubbles and evenly mix the solution from top to bottom. We then flowed the PEG solution into the assembled, aminosilanated samples, and placed the samples in a humidity chamber (pipette box with a lid, with water in the bottom). We incubated the PEG solution in the flow cells for 3-4 hours in the dark, then rinsed the flow cells with 500 μL Sodium Bicarbonate, followed by 2 mL of diH₂O. We then dried the cells completely with nitrogen. We stored the PEGylated flow cells in black-tape wrapped bottles, vacuum sealed, for up to 1 month.

2.5.6 DNA-tethering beads to surfaces

For TBP experiments, we prepared samples with DNA-tethered beads on our prepared PEG surfaces. For stabilization during the experiments, we also fixed streptavidin-coated beads to the biotin-PEGs on the surface. We began this sample preparation by epoxying a PEGylated sample. We prepared beads to be used in the sample by washing them (centrifug-

ing for 5 min. at 14K rpm to form a pellet, removing the supernatant, and resuspending the beads by pipetting) 3x in 200 μL phos-tween (10 mM Na Phos, 0.4% tween-20). After washing, we suspended the beads in MTWB-no BSA (20 mM Tris, 50 mM KCl, 0.4% tween-20) at the desired concentration (1 pM for streptavidin beads to be fixed to the sample surface, 375 pM for antidigoxegenin beads to be tethered via DNA). To separate beads that stuck together during washing, we sonicated the beads for 5 min.

To fix beads to the surface, we first washed the sample 2x with 200 μL MTWB-no BSA, then added 20 μL of the washed 1 pM Streptavidin-coated bead solution to the flow cell to incubate for 10 min. After incubation, we again washed with 2 x 200 μL MTWB-no BSA.

To form the DNA-bead tethers, we first incubated the washed 375 pM antidigoxegenin beads with 75 pM dig-bio-DNA (DNA modified at one end with digoxegenin, at the other end with biotin) in equal volumes for 20 min, quickly pipetting and vortexing on medium power to prevent local concentration mismatches and push the reaction towards forming complexes with 0 or 1 DNA's attached per bead. After the final sample wash following the step to fix beads to the PEG surface, we added 10 $\mu\text{g}/\text{ml}$ streptavidin (SA20) solution in MTWB-noBSA to the sample and incubated for 10 min., followed by washing with 2 x 200 μL MTWB-noBSA. Finally we attached the tethers to the PEG surface by adding the bead-DNA complexes to the sample and incubating for 20 min. After the incubation, we washed away unattached complexes with another 2 x 200 μL MTWB - no BSA wash.

For a few experiments, we prepared samples with DNA-tethered beads on non-PEG surfaces. The preparation was very similar to that on the PEGylated surfaces, but began with a clean (preferably KOH), epoxied flow cell. We attached biotynilated-BSA to the clean flow cell by flowing 50 μL of 125 $\mu\text{g}/\text{mL}$ bioBSA solution in Sodium phosphate buffer and incubating for 20 min. We then washed the flow cell with a BSA solution, MTWB (20 mM Tris, 50 mM KCl, 0.4% tween-20, 3 mg/mL BSA), and incubated for 10 min. to allow BSA to passivate the surface. The remaining steps (attaching straptavidin beads to the surfaces,

attaching streptavidin to the surfaces, preparing the bead-DNA complexes and adding them to the sample) were as described for the PEGylated flow cells, but with the BSA buffer MTWB and an added 10-min wait time between each step to allow the BSA to passivate.

2.5.7 TBP handling

For performing experiments with TBP, details of handling the protein were very important. Recombinant human TBP was provided by the Goodrich Lab, prepared as described in Ref. [27]. The protein was stored at -80°C , and transferred from the Goodrich Lab freezer to the Perkins Lab freezer on dry ice. When needed for an experiment, the TBP was removed from -80°C and warmed in finger tips for 1-2 min. before being placed on ice (in a water-filled cold-block). The buffers for dilution of the TBP were also on ice. The protein was added to the buffer, pipetted gently 5-10x, then tapped in the tube to mix. The diluted TBP was flowed into the room temperature sample on the microscope, and data was acquired for 30 min. If undiluted protein remained in the original tube, it was diluted again (after sitting on ice for 30 min.), added to the sample on the microscope (after washing the sample with 2 x 200 μL buffer), and data was acquired for another 30 min. Any remaining protein was discarded at this point (though care was taken to efficiently use the protein).

2.6 DATA ACQUISITION

For this thesis, we acquired several types of data, with the instrumental calibration and characterization, and TBP and control data on DNA tethers. This section provides details of the data acquisition.

For all types of data, warming up the instrument for several hours was important for stability and repeatable measurements. A minimum warm-up time was not determined, but typically the instrument was turned on at least 3 hrs before acquiring meaningful data. Turning on the lasers, electronics, and microscope lamp, and projecting the lasers through the microscope seemed to best stabilize the system.

2.6.1 Computer, controllers, drivers, and electronics

For precision and repeatability, data acquisition, sample positioning, laser positioning and laser intensity control were performed via a computer using custom-written LabVIEW software. Data was acquired on a computer via a 333 kS/s, 16-Bit, 16-Analog-Input Multifunction DAQ Board (National Instruments NI-PCI-6052E). Before being read by the DAQ board, position data from the QPDs was anti-aliased at 1/2 the data acquisition frequency using custom JILA electronics. The sum signal from the QPD was offset and differentially amplified with custom JILA electronics. Voltage data was communicated from the computer to the intensity-servo electronics, AOM drivers (when not using the intensity servo), shutters (Uniblitz) and PZT-mirror controllers (PI E-509.x3) via a 16-Bit Static Analog Voltage Output Board (National Instruments NI-PCI-6703). The stage position was both controlled and reported via a stage controller (PI E-710.P3D). Using computer-based LabVIEW software for measurements and instrumental control allowed precision and repeatability of measurements.

2.6.2 Centering lasers and beads

For data acquisition, precisely aligning one or more lasers with a bead was often necessary. This process is described for aligning over a stuck bead in Section 2.4. As an added step in this process, we sometimes had to manually move the fiducial detection laser via the micrometers on the PZT. This manual movement was necessary when a fiducial was beyond the range of the available PZT motion ($\sim \pm 5 \mu\text{m}$).

For a trapped bead, we often wished to align the trapped bead precisely with the detection laser. We accomplished this similarly to the process with a stuck bead, but using the PZT mirror to translate the trap laser while detecting the position signal via the detection laser. We acquired scans that look similar to those in Fig. 2.9, again fitting to the derivative of a Gaussian, finding the symmetry point, but now moving the trap via the PZT mirror to

move the symmetry point to the center of the detection laser. For trapping a bead attached to the surface by very short tethers, we modified this process by moving the stage and PZT mirror simultaneously to prevent pulling the bead out of the trap center. These centering processes were all automated in LabVIEW.

2.6.3 Setting height

We also often wished to precisely control the height of the lasers in our sample for our data acquisition. To determine the height, we aligned a bead in our laser (either by centering over a stuck bead or trapping a bead) and moved the stage axially. For a stuck bead, the acquired signals looked like those in Fig. 2.10. For a trapped bead, the signals looked like those in Fig. 2.12. To precisely position the height of sample relative to the lasers, we fit a parabola to the maximum peak of these signals, and chose a height offset from that peak.

2.6.4 Detection sensitivity calibrations

Once we accomplished sample positioning in the lateral and axial directions, we typically needed to calibrate the detection sensitivity of our bead in x , y , and z . The detection sensitivity calibration in x and y is described in Section 2.4. For the axial direction, we simply used the axial signals, as in Fig. 2.10. We switched the axes and fit the min to max portion of the curve to a 7th-order polynomial, obtaining a $nm(V)$ calibration. For trapped beads, the axial calibration is more complicated and is described in the next chapter. These sensitivity calibrations were automated in LabVIEW, and typically performed on each bead we measured.

2.6.5 Measuring trap stiffness and force

For measuring force (F), as is typically done in optical trapping, we calibrated the trap stiffness (k_{trap}), measured the bead displacement (x_{bd}), then calculated force assuming a linear force vs. bead displacement relationship, $F = -k_{trap} * x_{bd}$. The k_{trap} calibrations

are described in detail in Section 2.4. Measurement of the axial force is discussed in the next chapter.

2.6.6 Centering over DNA tetherpoint

Many of our experiments were completed on DNA-tethered beads. For these experiments, we carefully aligned the surface-tethering point relative to the lasers. For this alignment, we performed DNA force vs. extension measurements, like those shown in Fig. 2.23. We fit these curves with a worm-like-chain model [22] in both axes, both directions. The symmetry point of these fits represented the surface-tethering point, which we could then position precisely relative to the laser center.

For many experiments, we wished to iterate through the above processes at least twice to ensure precision. We often centered beads in our lasers, determined the height, calibrated the sensitivity in x , y , and z , performed a tether centering routine, and repeated. For measurements on short tethers, roughly pre-centering over the tether point using average x and y sensitivity-calibration parameters was necessary.

2.6.7 TBP and control tether data acquisition: DNA extension vs. time

We acquired TBP and control data on DNA-tethered beads on PEG surfaces. Our final assay is shown in Fig. 2.24. We tethered 330-nm dia. antidigoxigenin-modified latex beads to the PEG surfaces with 92 nm DNA, following the protocols described in Section 2.5. After sample preparation, we washed the sample with the buffer chosen for the experiment. We aligned the sample on the microscope, then selected individual tethers for data acquisition. With a custom-written LabVIEW program, we pre-stretched the DNA as described above, checking for a persistence (P) and contour (L) length consistent with a 92-nm tether. This screening was very preliminary because the program used average values for the sensitivity calibration, the fit was performed without geometry corrections, and the height and centering had only been roughly determined at this point.

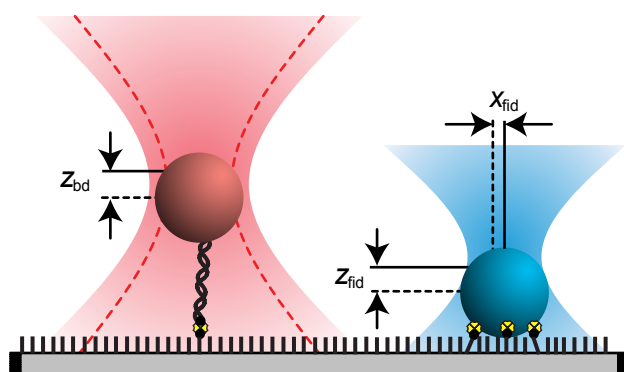


Figure 2.24: Final assay. Shown on the left, a DNA-tethered bead is trapped directly above the tethering point. The bead is tethered by biotinylated DNA attached to the surface by streptavidin bound to covalently attached biotinylated-PEG molecule. The bead displacement is detected by a second laser (*dashed curves*); displacement in the axial direction from the trap center is denoted z_{bd} . Shown on the right, a streptavidin coated bead is attached to the surface by biotinylated-PEG. The position (e.g. x_{fid} , z_{fid}) is measured by a separate laser and actively stabilized.

If the tether passed the screening criteria, we continued with data acquisition. First we manually aligned the fiducial detection laser over a stuck bead (using the micrometer on the PZT mirror). Next we set the height and centered over the tether-point as described above, then centered the fiducial-detection laser over the stuck bead with the PZT mirror. Then we calibrated the x , y , and z detection sensitivity for both the trapped-bead and the fiducial. (See the next chapter for z detection details). Next we performed a final x and y stretch of the DNA, before beginning data acquisition of position vs. time.

We stabilized the sample during the position vs. time data. We set the axial position and force by changing the axial stabilization set-point until the axial bead position (z_{bd}) moved to the desired position. We acquired data on 6 channels (x, y, z of the fiducial; x, y, z of the trapped bead) at 4 kHz, anti-aliasing at 2 kHz. We typically acquired data for 100-300 s per tether at a given force, unless something happened to stop the data acquisition (e.g. tether detached or another bead fell into the trap). If data at another force or bead position was desired, we then moved the sample-stabilization set-point and/or changed the trap stiffness and acquired more data. On a given sample, we usually acquired at least 100 s of control data on the sample before adding TBP to the sample.

2.7 DATA ANALYSIS

We analyzed our data both in real-time during data acquisition as well as afterwards for more in-depth analysis. For real-time analysis, we used LabVIEW. We performed more extensive analysis after acquisition using Igor.

Real-time analysis of data during acquisition was performed for centering, calibrations, and averaging of signal vs. time data to allow visualization and active sample stabilization. Analysis for centering and calibrations was already described in Sections 2.4 and 2.6. For sample stabilization, the LabVIEW-based software servo is also described in Section 2.3. For stabilization, position vs. time data was box-averaged and stabilized at 100 Hz in LabVIEW.

Post-acquisition analysis in Igor was used for plotting and viewing, averaging and

decimating, fitting, performing mathematical transformations, and simulating. We wrote custom Igor procedures to plot and quantify essentially every type of instrumental data acquired. To highlight the programs where Igor analysis was essential, I will discuss the procedures used to process PZT calibration data, tether stretching data, position vs. time data, and the step-like DNA-extension changes in TBP data. We also wrote simulations in Igor to simulate a bead in an optical trap and to simulate TBP-induced DNA-extension changes.

2.7.1 PZT calibrations

For calibrating the PZT mirrors, the data was loaded into Igor as a matrix of x and y stage positions with corresponding V_x and V_y PZT voltages. These were plotted and fit in cross-section to obtain slopes, or nm/V values, in the x and y axes, as well as cross-talk terms. These slopes were averaged and the averages used as the calibration values for the PZT mirrors.

2.7.2 Force vs. extension

For DNA force vs. extension curves, the lateral bead displacement and the lateral tether-point displacement were recorded in LabVIEW. These values were loaded into Igor, and a custom-written procedure calculated the geometry-corrected force and extension [21]. The curve was then fit in Igor with a modified Worm-like-chain [22] to obtain the persistence length and contour length.

2.7.3 Stability/noise calculations

Position vs. time data was processed in Igor to show the instrumental stability and noise. The data was Box-smoothed and the standard deviation at the smoothing rate provided one measurement of the noise. We also calculated the power spectral density using the Wavemetrics PSD algorithm. We then calculated the integrated noise vs. frequency by

integrating the PSD from a minimum frequency up to the given frequency. The standard deviation, PSD, and integrated noise were all used to characterize the noise of a given trace.

2.7.4 Simulation: Bead in an optical trap

We simulated position vs. time traces for a bead in an optical trap. Simulation were based on the theoretical characteristics of a trapped bead trace, namely the theoretical relationships between the trap stiffness (k_{trap}) and various trace properties: the standard deviation ($\sigma = \text{sqr}(k_B T / k_{trap})$ where $k_B T$ is the thermal energy), the corner frequency of a fit to the power spectral density (PSD) of the trace ($f_0 = k_{trap} / 2\pi B(h)$ where $B(h)$ is the Faxen's Law corrected drag at height h), and the autocorrelation time constant ($\tau = B(h) / k_{trap}$). Note that to fully specify these properties, we chose an input k_{trap} and bead height, h . The simulation input and output values are shown in Table 2.6.

Table 2.6: Trapped bead simulation input and output values.

Value	Simulation Input	Output, Full Bandwidth	Output, Filtered
k_{trap} input (pN/nm)	0.0300		
k_{trap} via EQP		0.0300	0.0341
k_{trap} via PSD		0.0309	0.0310
k_{trap} via tau		0.0308	0.0276
σ (nm)	11.7	11.7	11.0
f_0 (Hz)	384	395	397
τ (ms)	0.415	0.404	0.451

Fig. 2.25 outlines the process we followed for the simulation. First, we made a Gaussian noise wave with the desired length and time scaling (10 s at 120,000 pts/sec). Next we made an exponential wave with the desired time constant, τ . We convolved the Gaussian noise wave with the exponential wave, deleted the 2nd half of the wave that contains irrelevant points, and scaled the remaining wave to have the correct standard deviation. Finally, we filtered the resulting trace to 2kHz by taking the Fast-Fourier Transform (FFT), setting the components with $f > 2$ kHz to zero, and taking the inverse FFT to yield the final filtered

trace. We analyzed both the full bandwidth and the filtered simulation. The resulting traces, histograms, PSDs, and autocorrelations are shown in Fig. 2.26. The histograms were Gaussian, the power spectral densities were Lorentzian, and the autocorrelations were exponential. The std. dev. of the trace, corner frequency of the Lorentzian fit to the PSD (f_0), and characteristic time (τ) of an exponential fit to the autocorrelation are shown in Table 2.6. We also calculated the simulation output k_{trap} from these values as described by the equations above. At full bandwidth, all the simulation output values match well with the simulation input values. However, after filtering to 2 kHz, the accuracy of the values derived from equipartition and autocorrelation analysis decreased. In contrast, the values derived from the power spectral density analysis remain accurate even after filtering.

2.7.5 Calculation of axial bead position probability distribution

To determine the expected distribution of positions of a trapped bead in the axial direction, a calculation must be made of the expected probability, $P(z)$, of axial positions of a bead in a laser trap. This probability is related to the axial potential energy profile of the trap (U) and the thermal energy ($k_B T$) by Boltzmann statistics [13]

$$P(z) \propto e^{-U/k_B T}. \quad (2.6)$$

U is simply the negative integral of the total force on the trapped bead (F_{total}),

$$U = - \int F_{total} dz. \quad (2.7)$$

This statement is only true for conservative forces. F_{total} is the sum of two forces, the scattering force (F_{scat}) and the gradient force (F_{grad}) [28]

$$F_{total} = F_{scat} + F_{grad}. \quad (2.8)$$

The scattering force is not a conservative force (the integral is path-dependent), but for the purposes of this calculation, the integral simply can be calculated for the path along $x = 0$,

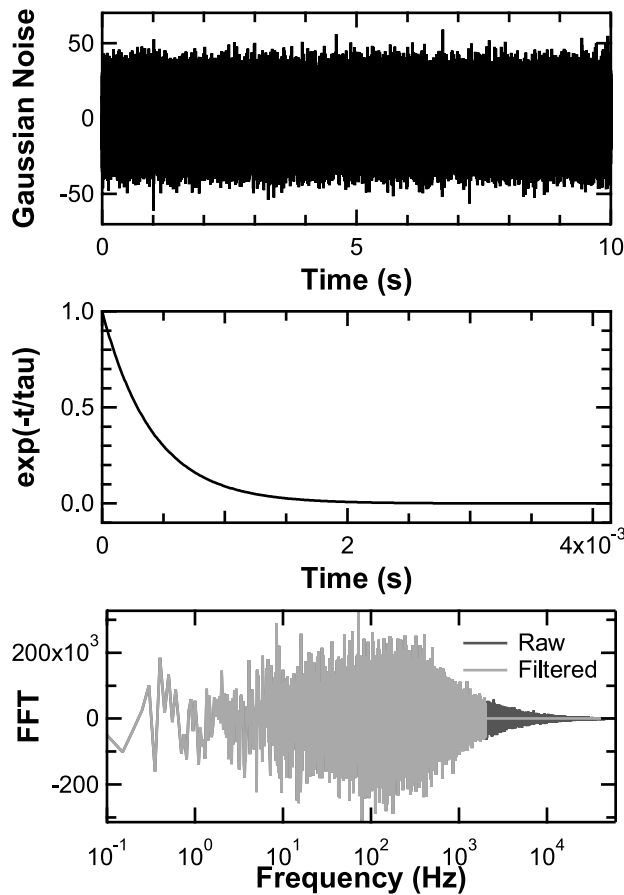


Figure 2.25: Process for simulating trapped bead position traces. The goal was to simulate a position vs. time trace with the spatio-temporal properties of a bead trapped with a stiffness, k_{trap} , at a height above the surface, h . To create the simulated trace, a Gaussian noise trace (A) was convolved with an exponential trace (B). The exponential was given by $y = \exp(-t/\tau)$ where $\tau = B(h)/k_{trap}$ and $B(h)$ is the Faxens corrected drag. The resulting convolved trace had two distinct halves: one half was Gaussian noise with a Lorentzian power spectral density (PSD), the other half was a constant. We truncated the convolved trace to the relevant Gaussian noise portion, then scaled it to have the correct standard deviation (σ) for k_{trap} , $\sigma = \text{sqrt}(k_B T/k_{trap})$, where $k_B T$ is the thermal energy. This process yielded a final trace with Gaussian noise, a Lorentzian-shaped PSD, and an exponential autocorrelation. (C) We then took the fast-fourier transform (FFT) of the final trace (*dark gray*) and filtered it by setting $\text{FFT}=0$ for all frequencies, $f > 2$ kHz (*light gray*).

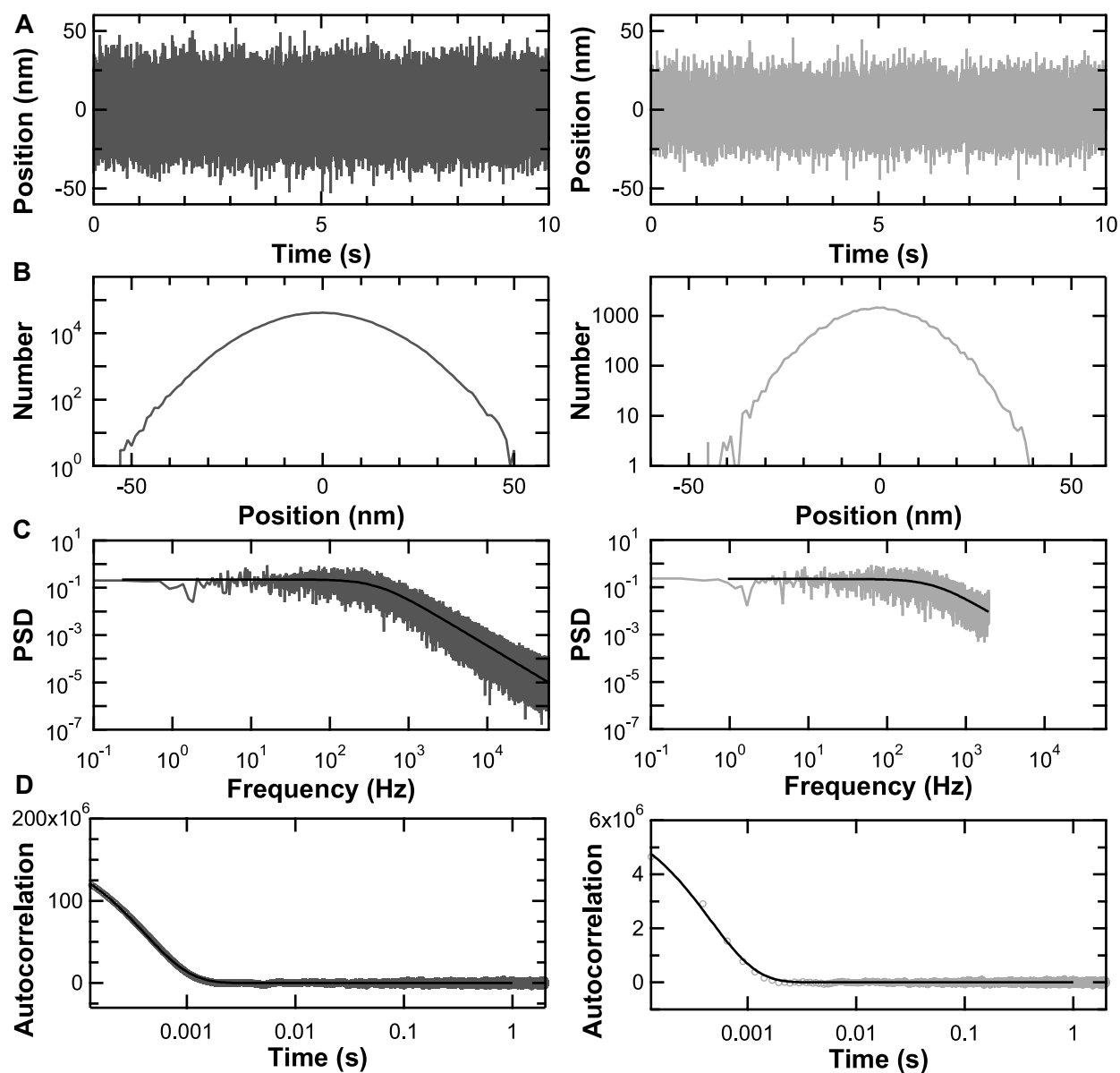


Figure 2.26: Simulation of a trapped bead axial position trace. We plotted results from both the full-bandwidth simulation (left) and the simulation filtered to 2kHz (right). (A) Axial bead position vs. time. (B) Histogram of bead positions. (C) PSD and Lorentzian fit of bead positions. (D) Autocorrelation and exponential fit of bead positions.

$y = 0$ [29]. Thus if we can calculate F_{scat} and F_{grad} as functions of z , we can calculate the probability distribution of bead positions in the axial direction.

To calculate F_{scat} and F_{grad} for our optical trap, we must relate these forces to measurable properties of our trap. The scattering force is related to the laser intensity (I), scattering cross-section (σ), refraction of the solution (n_m), and the speed of light (c) by [13]

$$F_{scat} = I\sigma n_m/c. \quad (2.9)$$

σ is related to the bead radius (r_{bd}), the laser wavelength (λ), and the relative index of refraction ($m = n_p/n_m$ where n_p is the index of refraction of the bead) by [13]

$$\sigma = \left(\frac{128\pi^5 r_{bd}^6}{3\lambda^4}\right) \left(\frac{m^2 - 1}{m^2 + 2}\right)^2. \quad (2.10)$$

The gradient force is related to the polarizability (α), the gradient of the intensity (∇I), the speed of light, and the index of refraction of the medium (n_m) by [13]

$$F_{grad} = (2\pi\alpha/cn_m^2) * \nabla I. \quad (2.11)$$

α is related to the index of the medium, the bead radius, and the relative indices of refraction by [13]

$$\alpha = n_m^2 r_{bd}^3 \frac{m^2 - 1}{m^2 + 2}. \quad (2.12)$$

Thus F_{scat} and F_{grad} depend on several measurable properties, including the intensity profile. To find the z dependence of these forces, we must use the axial intensity profile, I_z of our laser.

For calculating the axial intensity profile of our focused laser, we assume Gaussian beam optics, i.e. the lateral intensity profile I_r is given by [30]

$$I_r = I_0 e^{-2r^2/w^2}. \quad (2.13)$$

For the axial dependence, the beam width as a function of z , $w(z)$ is then given by [30]

$$w(z) = w_0 [1 + (z/z_0)^2]^{1/2} \quad (2.14)$$

where w_0 is the beam waist, z is the axial position from the waist, and z_0 is the Rayleigh range, [30]

$$z_0 = \pi w_0^2 / \lambda. \quad (2.15)$$

Here λ is the laser wavelength.

To relate these equations to the axial intensity profile and to the measurable power in our trap, we use the relationship between intensity, laser power (P) and area (A), $I = P/A$. Since P remains the same at every lateral cross section, and the area changes with beam width as $A = \pi w(z)^2$, we obtain

$$I_z = P_w / (\pi * w(z)^2) \quad (2.16)$$

where P_w is the power within the beam width, w . To calculate the power within the beam width from the total power, we use the general equation for calculating the power within a radius, P_R using Gaussian beam optics, (Newport Gaussian Beam Optics tutorial)

$$P_R = P_{total}(1 - e^{-2(R/w)^2}). \quad (2.17)$$

If we substitute the beam radius w for R , we obtain $P_w = P_{total}(1 - e^{-2})$. Substituting this P_w and the equation for $w(z)$ (Eq. 2.14) into Eq. 2.16, we obtain

$$I_z = \frac{P_{total}(1 - e^{-2})}{\pi w_0^2(1 + (z/z_0)^2)}. \quad (2.18)$$

This intensity is the average intensity within the beam width, w . Thus with a known beam waist (w_0) and laser power, P , we can calculate the axial intensity profile (with intensity being the average intensity within the beam radius w).

For the purposes of our final calculation of the axial bead position probability distribution, we only needed the relative value of the intensity profile, since any multiplying factor of the intensity would only result in an irrelevant multiplying factor of the final probability. A normalized intensity, I_{norm} can be calculated based on Eq. 2.18

$$I_{norm} = \frac{1}{1 + (z/z_0)^2}. \quad (2.19)$$

Using this intensity profile in the calculations of F_{scat} and F_{grad} , then integrating gives us the potential energy profile. We then exponentiate to obtain the probability distribution of axial bead positions.

The values we used in the final calculation are given for reference. For the final calculation of I_{norm} , z_0 was obtained from fit of the 1064 axial detection signal to the Pralle axial intensity equation [18] (without the π) to give $z_0 = 675.144$ nm. For calculating F_{scat} and F_{grad} , we ignored c since it was simply a scaling factor in both forces. We used $n_m = 1.33$ (index of H_2O), $r_{bd} = 165$ nm, $\lambda = 1064$ nm, and $n_p = 1.591$ (for our beads at 20C and 500 nm wavelength from manufacturer bead information sheet). We performed the calculations in Igor, calculating the intensity profile I_{norm} given by Eq. 2.18 with 4000 points from $z = -2000$ to $+2000$ nm. We multiplied and numerically differentiated I_{norm} as dictated by the equations above to obtain F_{scat} and F_{grad} , introducing a scaling factor (10^{-5}) to prevent large-number errors when exponentiating in the final calculation of $P(z)$. We numerically integrated F_{total} to obtain U . We exponentiated U to obtain $P(z)$, using $k_B T = 4.1$ pN nm for the thermal energy at room temperature. The resulting normalized intensity, scattering and gradient forces, potential energy profile, and probability distribution are shown in Fig. 2.27.

Even without calculating the actual values of the intensity curve, we see that the total force is the addition of a hyperbolic curve shape (representing the direct relationship between F_{scat} and the intensity) and the derivative of a hyperbolic curve shape (representing the derivative relationship between F_{grad} and the intensity). Intuitively, the shape of this force curve, as well as the potential energy profile derived from it and the probability distribution of trapped bead positions, will be asymmetric. This asymmetry has been noted in the literature [31, 32, 29, 33].

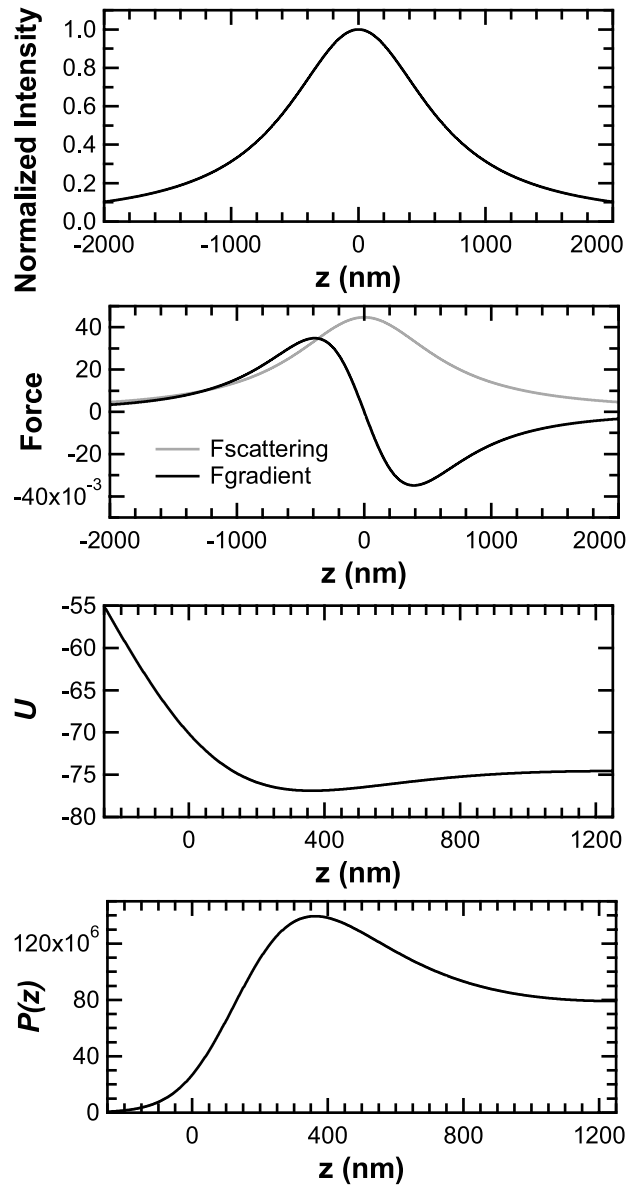


Figure 2.27: Theoretical calculation of axial bead position probability distribution. Based on properties from our experiment, we calculated the axial intensity profile of our trap (*top*). From the intensity, we calculated the scattering ($F_{scattering} \propto I$) and gradient forces ($F_{gradient} \propto \nabla I$) (*2nd from top*). Adding these forces together yields the total force, which, when integrated, gives the potential energy curve, U , of our trap (*3rd from top*). Finally, from U , the probability distribution of axial bead positions, $P(z) \propto \exp(k_B T/U)$ was calculated (*bottom*). Note the asymmetry due to adding together the scattering and gradient forces.

2.7.6 Hidden-Markov modeling analysis of TBP data

The analysis of the TBP-induced DNA-extension changes was based on a hidden-Markov modeling (HMM) algorithm. We originally used a program written for processing FRET signals, which required all values be between 0 and 1 [34]. We modified our data for this program by normalizing all values to be between 0 and 1, processed the data with the HMM-algorithm, then converted all values back to the original values. This analysis yielded average extension changes, and rates of bending and unbending. The bending and unbending rates were found by either the probabilities in the transition probability matrix, or by fitting the dwell time histograms of the most-likely path. Data was rejected if no extension changes were found. We also implemented a more sophisticated version of this HMM-algorithm, added a drift-correction to correct for baseline drift of our data. This drift correction was accomplished by adding Fourier modes to account for drift in the traces and using the HMM-algorithm to find the most-likely path, including both drift and step-like changes.

2.7.7 Simulation: TBP data

We simulated TBP data by simulating a trace with Gaussian noise and adding exponentially distributed steps to that trace. We chose the Gaussian noise level based on our data (~ 1 nm noise for data smoothed to 1.67 Hz). We chose the step-size as 3 nm, based on the analysis from our measurements. We chose the exponential rates based on the exponential fit to the dwell times in our data. See the TBP chapter for more details.

Chapter 3

AXIAL CALIBRATION AND DETECTION

3.1 INTRODUCTION

As discussed in the previous chapters, our experimental techniques were driven by the challenges presented by our biological system of interest: TBP bending DNA. The predictions of a small and infrequent signal for TBP bending DNA led us to implement the actively stabilized optical-trapping instrument, as well as the precise alignment and calibration techniques and the automated data acquisition described in the previous chapter. Preserving TBP activity and preventing nonspecific binding drove the development of the sample preparation techniques. The acquired data led to the data analysis techniques described. These experimental techniques paved the way for studying TBP bending DNA at the single-molecule level.

With the implementation of the experimental techniques described, one experimental challenge remained. For interpretability, we wished to study TBP bending DNA in single bending events at specific TATA box DNA sequences. While TBP has higher binding affinity for TATA box DNA sequences, TBP also has lower binding affinity for non-TATA box DNA sequences [2]. To ensure single bending events at specific TATA boxes (as opposed to multiple bending events at random DNA sequences), the DNA tethers in our experiments needed to be short with carefully designed sequences. These short DNA tethers prove challenging for study via optical trapping techniques due to constraints in traditional trapping geometries. To overcome this last experimental challenge, we developed an axial calibration and detection

technique capable of measuring extension changes on the short DNA tethers required for studying TBP bending DNA.

3.1.1 Geometry constraints in traditional optical trapping

In traditional optical trapping, measurements are performed primarily in the lateral (x, y) axes. For a surface-based optical-trapping assay, measuring in the lateral direction requires a diagonal experimental geometry, like that shown in Fig. 3.1. In this diagonal geometry, calibrations generally are made for the lateral bead displacement from trap equilibrium (x_{bd}) and the lateral trap stiffness ($k_{trap,x}$), while the lateral location of the tetherpoint generally is obtained by a centering routine. From this tetherpoint, the pre-calibrated stage then offsets the sample laterally by a known amount (x_{stage}) to extend the tethering molecule and apply a force. With these lateral calibrations, measurements are made of lateral projections of the bead displacement (x_{bd}), force ($F_x = k_{trap,x} * x_{bd}$), and extension ($x_{DNA} = x_{stage} - x_{bd}$) of the tethering molecule.

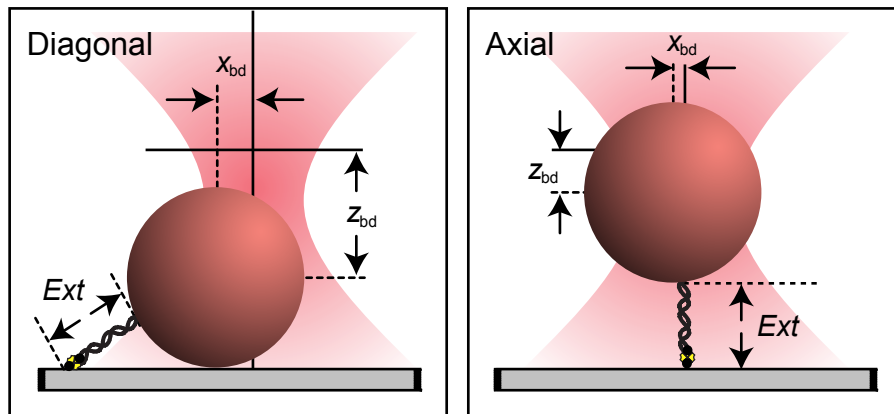


Figure 3.1: Diagonal vs. axial geometry. The diagonal geometry is typical for surface-based optical trapping, and the diagram shows the geometry problem that occurs with short DNA molecules. The axial geometry offers a solution to this problem, as well as offering several other advantages over the typical diagonal geometry.

In diagonal assays, these lateral measurements are projections of the more relevant quantities of total force, F , and extension of the tethering molecule, Ext . Calculations of

F and Ext require assumptions about the axial trap stiffness, $k_{trap,z}$, and the axial extension, z_{DNA} . Usually $k_{trap,z}$ is calculated using theoretical assumptions about the axial:lateral trap stiffness ratios [21]. For z_{DNA} , determination generally relies on some means of determining the trap height, z_{trap} , and the axial bead displacement from trap equilibrium, z_{bd} . Determination methods for z_{trap} vary; examples of methods include measuring the height dependence of the lateral drag coefficient [21], using features of the detected intensity curve as a bead is scanned through the laser axially [35], and a combination of the two [13]. To determine z_{bd} , geometry is used in combination with the other known and assumed quantities. Specifically, the axial:lateral force ratio, F_z/F_x , is equated to the axial:lateral extension ratio, z_{DNA}/x_{DNA} ,

$$\frac{F_z}{F_x} = \frac{k_{trap,z} * z_{bd}}{k_{trap,x} * x_{bd}} = \frac{z_{trap} - z_{bd}}{x_{stage} - x_{bd}} = \frac{z_{DNA}}{x_{DNA}}, \quad (3.1)$$

and the resulting equation is solved for z_{bd} . With the geometry fully determined, the axial projections of the total force and the extension can be obtained, i.e. $F_z = k_{trap,z} * z_{bd}$, and $z_{DNA} = z_{trap} - z_{bd}$. From these and the laterally measured quantities, the total force and extension of the tethering molecule are geometrically calculated, $Ext = (z_{DNA}/\sin(\theta)) - r_{bd}$ and $F = F_x/\cos(\theta)$ where θ is the angle between the sample surface and the tethering molecule, $\theta = \tan^{-1}(z_{DNA}/x_{DNA})$ [21]. In summary, the experimentally relevant quantities of total force and total extension are calculated based on calibrated measurements in the lateral axis, combined with an estimate of the axial extension and an assumed axial trap stiffness.

To minimize measurement uncertainties in diagonal optical-trapping assays, the angle between the surface and the tethering molecule should be as small as possible. When this angle is small, x_{DNA} is large compared to z_{DNA} and F_x is large compared to F_z . We assume z_{DNA} and F_z have a larger uncertainty since they are derived from multiple other measurements and assumptions. Thus the larger x_{DNA} and F_x are compared to z_{DNA} and F_z , the less the uncertainty in the axial quantities affects the uncertainty of the final measurements.

When making measurements on long tethering molecules, satisfying this small angle ideal is easily accomplished.

In contrast, when making measurements on short tethering molecules, this small angle ideal becomes much more difficult to achieve. The difficulty arises when the tethering molecule extension becomes of similar size to the tethering bead radius, r_{bd} , i.e. $Ext \sim r_{bd}$. To see this mathematically, let $Ext = r_{bd}$. Then $\theta > 45^\circ$ for the bead to remain above the surface. Explicitly, $\sin \theta = (z_{trap} - z_{bd}) / (Ext + r_{bd})$. With $Ext = r_{bd}$, $\sin \theta = (z_{trap} - z_{bd}) / 2r_{bd}$. For the bead to remain above the surface, $z_{trap} - z_{bd} > r_{bd}$, thus $\sin \theta > r_{bd} / 2r_{bd} = 1/2$, i.e. $\theta > 45^\circ$. These equations set a lower limit on the angle, but experimentally, this angle should be larger than 45° to prevent the bead from resting on the surface and skewing the geometry. Thus as the extension of the tethering molecule approaches the scale of the bead radius, the trapping angle must become larger, and the uncertainty in the measurements increases as described.

3.1.2 Advantages of axial trapping and detection

Axial trapping and detection offers a solution to the geometrical problem in traditional optical trapping, in the form of geometrical simplification. In contrast to the diagonal geometry of traditional surface-based trapping, the axial trapping geometry is a single axis, vertical geometry, as shown in the axial geometry in Fig. 3.1. No angles must be calculated or assumed; the signal measured axially is the full signal, not a geometrical projection of the signal, and this advantage improves the signal to noise. The total bead displacement is the axially measured bead displacement, z_{bd} ; the total force is the axially measured force, $F = F_z$; the extension is the axially measured extension, $Ext = z_{DNA}$. Additionally, axial trapping minimizes crosstalk between axes because bead motion is directly on one axis rather than at an angle. These geometrical advantages make a compelling case for axial detection.

The improved trapping geometry in axial trapping allows shorter biological tethers to be studied. These shorter DNA tethers allow the detection of single binding events by DNA-

binding proteins with lower sequence specificity, solving the final experimental challenge in our TBP experiments. In addition to the expansion of biological systems that can be studied, the shorter biological tethers that can be studied without a geometric restriction increase the stiffness of the system and therefore improve the signal to noise. The signal-to-noise advantages and addition of the biological phenomenon that can be studied on short DNA have driven our motivation to trap and detect along the axial direction.

Axial trapping also has advantages over other methods that allow a single-axis trapping geometry, namely dual-beam trapping and trap-pipette geometries. In a dual-beam trapping geometry, the short biomolecules that can be studied with axial trapping would be difficult to study because when the two traps of the dual-beams are too close, interference and/or bead hopping between traps occurs. The trap-pipette geometry would overcome this obstacle, but the pipette in this setup is subject to mechanical noise. The mechanical noise problem could theoretically be remedied by stabilizing the pipette tip relative to the laser, as we stabilize our surface relative to the laser [10, 11, 12]. Given the demonstrated stability of our surface-based assay, for the excellent signal-to-noise offered by a single-axis trapping geometry and short biological tethers, axial trapping seems to be the best choice.

3.1.3 Axial detection in the literature

Given the potential advantages of axial trapping and detection, unsurprisingly many examples of axial calibration exist in the literature. Earlier introduced axial calibration techniques included axial detection via an overfilled photodiode [36, 37], fluorescence detection [38, 39], evanescent wave excitation [40, 41] and video [42]. These methods tended to suffer from limited spatio-temporal resolution and/or require additional optics and detectors, and thus have not been widely adopted by the optical-trapping community.

The more recent axial calibration techniques, including the one introduced in this thesis, have been based on the intensity changes that occur at a detector placed at the back focal plane of an optical-trapping microscope when a bead is moved axially through a focused

laser. This intensity vs. axial bead position curve was described theoretically by Pralle et al. [18] and then in even more detail by Rohrbach et al. [29]. The shape of the curve is attributed to interference of the scattered and unscattered light, which undergoes a gouy phase shift at the laser focus [18]. The dependence of this signal vs. capture angle has been theoretically described [29, 43] and experimentally tested [44]. Neuman et al. [13, 19] used this curve, obtained on beads fixed to the sample surface, to serve as an average calibration curve for trapped beads. With this calibration process, axial bead position was measured [45, 13, 19], an axial force clamp was applied [45], and the effective focal shift caused by the index mismatch at the coverslip-buffer interface was estimated [13, 19]. This axial detection method, exploiting intensity dependence on axial bead position, has been the basis of the more recent efforts towards precision measurement in the axial direction.

Other recently introduced techniques were also based on a more complex application of this axial intensity detection curve. In one of the most recent and thorough treatments of axial calibrations, Deufel and Wang state that three parameters must be determined for axial detection: 1)axial displacement from the trap center, 2)axial stiffness, and 3)axial height above the surface [46]. These three quantities were determined with precision in Deufel and Wang's work, as well as by two other recently introduced methods [47, 48]. In the work of Deufel and Wang, a DNA construct was unzipped to determine the average displacement, stiffness, and height calibrations. Sample preparation and unzipping DNA constructs for a calibration may be somewhat unwieldy, but the authors also show that using the power spectral density to obtain the axial trap stiffness and then using this stiffness in the equipartition equation to obtain the displacement calibration yields a reasonable calibration of stiffness and displacement. Schaffer et al. introduce a method to calibrate axial displacement, stiffness, and height using the power spectral density of a trapped bead while oscillating the sample [47]. Most recently, Chen et al. introduced an axial detection method that uses multiple trapping lasers coupled with calibrated video detection and laser detection, and offers the advantage of the passive-force-clamp technique [48]. These methods

extend the detection capabilities of optical trapping to the axial direction.

We wished to build a precision axial detection method, capable of measuring force and extension changes on very short DNA, from these most recent examples in the literature. We adopted the calibrations above that were most straightforward to perform in our actively stabilized optical- trapping instrument, in essence using Neuman’s axial displacement, axial trap stiffness, and trap height calibrations [45, 13, 19] as a starting point. Into the displacement calibration, we built floating parameters that allowed the calibration to be customized for each trapped bead. We attempted to improve the displacement calibration and estimation of the trap equilibrium point by correcting for the voltage oscillations that occur with depth. For the trap height estimation in our system, we found a stiffness-dependent correction, and for trap stiffness, we determined a height dependent correction. Ultimately we found these techniques provided adequate measurements of the trap stiffness and relative axial displacement, but a final connection between DNA polymer theory and the height dependent drag was required for estimating axial force and tether extension.

3.1.4 Overview of our technique

We present here an axial calibration and detection method for determining axial displacement, stiffness, and height capable of measuring force and extension on very short (92 nm) DNA. Like the other recently introduced axial calibration methods, this method is based on the intensity distribution that occurs when a bead is moved axially through a focused laser. This intensity distribution is shown for a bead fixed to the sample surface (*dashed line*) and for a trapped bead (*gray line*) in Fig. 3.2. The fit to the Pralle-described theoretical curve [18] is represented by the black line in Fig. 3.2. The technique involves determining an average axial detection voltage vs. axial bead position curve with beads coupled to the coverglass surface, then using that average curve to reconstruct full detector response curves for trapped beads, with floating parameters that allow the calibration to be specific to the individual bead. Unlike previously introduced methods, our method achieves high precision

without requiring a specialized biological construct, multiple traps, or multiple types of detection. We quantify the uncertainty in our axial calibrations, finding low uncertainty in our relative axial displacement and trap stiffness measurements. Higher uncertainty in the absolute height measurement and trap equilibrium position led to large errors for force and extension measurements on DNA, so we introduce a more accurate method for estimating axially measured forces and DNA extensions. Finally, we demonstrate the improved signal to noise afforded by axial trapping and detection of a bead attached to a short DNA molecule.

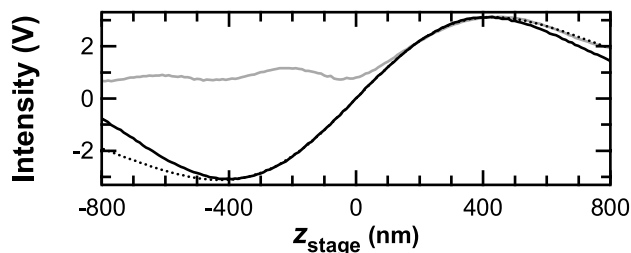


Figure 3.2: Axial intensity signal. The axial detection voltage vs. stage height is plotted for axial scans of the sample. The stage was scanned axially, and the axial detection voltage was recorded for a stuck bead (*black*) and a trapped bead (*gray*). The Pralle equation (*dashed line*) provides the theoretical description for these curves.

3.1.5 A conceptual description of axial trapping and detection

To provide background for understanding the calibrations and measurements in the following sections, this section provides a conceptual overview of axial trapping and detection. In this conceptual description, a focused laser propagates in the plus z direction, forming an optical trap. The optical trap holds a bead at equilibrium, in the center of the laser laterally, slightly past the focus axially due to the balance of scattering and gradient forces. The bead is trapped within a sample, and the sample surface moves axially. As the sample surface moves axially, because of an index mismatch between the glass surface of the sample and the buffer inside the sample, the focal point of the laser also shifts axially. This shift is known as the focal shift, and generates a correction factor estimated in the literature and in this

chapter. As the sample surface moves upward axially, it pushes the trapped bead upwards in the laser, past equilibrium, but trapped against the sample surface. As the sample surface moves downward axially, the bead follows the surface until it reaches equilibrium. Then the sample surface continues to drop away as the bead sits at trap equilibrium. If the bead is linked to the surface, the linker pulls the bead downward to follow the dropping sample surface. If the linker is compliant, the extension of the linker grows as the sample surface pulls downward. The downward force from the linker balances with the upward force from the trap, like two springs pulling on the bead in opposite directions. This physical picture describes axial trapping.

To describe axial detection, the laser light must be described. The laser light, after encountering the sample and bead, continues propagating to the detector. The intensity distribution on the detector changes as the bead moves vertically in the laser. The relationship between bead motion in the laser and laser intensity at the detector is given by the Pralle equation [18].

However, for a bead near a sample surface, a secondary scattering phenomenon also affects the intensity of the light at the detector. This secondary scattering phenomenon is due to light interfering as it bounces between the bead and the sample surface. As the bead to sample surface distance (h_{bd}) changes, this phenomenon causes an oscillation in the amount of light reaching the detector, which appears as an oscillation in the intensity of the light at the detector [19].

In the physical picture of axial detection, we therefore have two relationships governing the intensity of light at the detector; we have the Pralle relationship describing the relationship between the intensity and the position of the bead in the laser, $I(z_{bd})$, and we have the oscillating affect describing the relationship between the intensity and the bead-surface distance, $I(h_{bd})$.

To complete the conceptual description of axial detection, the detection voltage must be described. In a detection voltage picture, we examine the same physical picture as above,

now examining the effects on the detection voltage. For a detector placed at the back-focal plane, the axial detection voltage, V_z , is directly proportional to the laser intensity, I , on the detector, i.e. $V_z \propto I$. As described above, the intensity on the detector changes as the bead moves vertically in the laser and as the bead-surface distance changes, $I = I(z_{bd}) + I(h_{bd})$. Thus, the detector voltage changes in the same way, yielding proportionate relationships between bead motion in the physical system and detector voltage, i.e. $V_z = V(z_{bd}) + V(h_{bd})$.

This physical picture and the relationship with the detection voltage provide the background information for the calibrations and measurements that follow.

3.2 MATERIALS AND METHODS

The actively stabilized optical trapping instrument and detection system were as described in the Experimental Techniques chapter. Calibrations for beam steering (PZT mirror calibrations) and lateral trap stiffness were as described. Sample and laser positioning (centering laser foci with each other, with beads fixed to the surface, with trapped beads and relative to tether points) and lateral displacement calibrations were also performed as described in that chapter.

For detection of bead position, we used a quadrant photodiode (QPD) for each detection laser, placed in the back-focal plane of the microscope condenser. With this arrangement, the sum of the voltage from the four quadrants is proportional to the intensity on the QPD, which is related to the axial bead position as described in the text. In our experiment, this QPD sum voltage was further modified electronically with a tunable voltage offset and differential amplification. For conciseness, this offset, differentially amplified QPD sum voltage is referred to as the axial detection voltage, V_z , in the rest of this thesis.

For clarity, an explanation is useful describing the variability of the absolute values of V_z and axial stage position, z_{stage} , in our experiment. The absolute value of V_z varied due to an adjustable electronic voltage offset. In a given experiment, the absolute value of V_z provided the means for measuring axial position and thus was not adjusted between

calibration and measurement or during the measurement. However, between experiments, the offset varied. The absolute value of z_{stage} varied due to drift. Because of the variability in both these quantities, we built voltage and axial offsets (V_{off} and z_{off}) into the fits of V_z vs. z_{stage} curves (see text for details). To eliminate variability in plots of the V_z vs. z_{stage} , we subtracted the voltage and axial offsets obtained in the fits before plotting, giving $V_z = 0$ and $z = 0$ meaning only in the context of the fit. In later sections, we identify two other meanings for $z = 0$. In one context, $z = 0$ indicates that a bead trapped at equilibrium would rest on the sample surface; in another context, $z = 0$ represents the point when a trapped bead would be positioned at equilibrium ($z_{bd} = 0$). The relative nature of V_z and z_{stage} and the context-dependent meaning of $z = 0$ are important details for understanding our plots and calibrations.

Sample preparation was performed as described in Experimental Techniques, as well. Samples included flow cells with beads fixed to surfaces (by salt, not melting), beads free in solution, and beads tethered to the surface via 92 nm DNA. The DNA tethered bead samples were either on biotynilated BSA (force vs. extension curves) or on PEGylated surfaces (all other tether data). Beads were either 330 nm dia. antidigoxigenin-modified beads or 860 nm Streptavidin coated beads, as indicated. Data was acquired in filtered, deionized H_2O , except force vs. extension data (10 mM phos, 3 mg/ml BSA, 0.4% tween-20, [25]) and other DNA tether data (10 mM Tris, 10 mM Hepes, 150 mM KCl, 0.5 mM MgCl₂, 1 mM DTT, 0.2% tween-20, 0.4 mg/mL BSA).

Data acquisition was also as described in the Experimental Techniques chapter. In each type of data acquired, care was taken to laterally align detection lasers with detected beads, since the axial detection signal depends on this lateral alignment. This alignment was accomplished via automated centering programs as described in that chapter. Lateral detection calibrations were performed at the measurement height.

Data analysis was performed in Igor; methods are described in the text.

3.3 AXIAL CALIBRATIONS

To quantitatively manipulate and measure in z , we calibrated the axial displacement (z_{bd}), the trap height above the surface (z_{trap}), and the axial trap stiffness ($k_{trap,z}$). Because the trap equilibrium point on the calibration curve was not *a priori* known, the axial displacement measurement was divided into two parts: the relative axial displacement (Δz_{bd}) and the estimated trap equilibrium position ($z_{bd} = 0$). These calibrations provided measurements of 4 experimentally relevant quantities: 1) extension changes of DNA, 2) estimates of the axial trap stiffness, 3) an initial estimate of the force on a trapped bead ($F = k_{trap,z} * z_{bd}$) and 4) an initial estimate of the height above the surface of a trapped bead ($h_{bd} = z_{trap} - z_{bd}$).

3.3.1 Calibration of relative axial displacement

To calibrate the relationship between the relative axial displacement and the axial detection voltage, $\Delta z_{bd}(V_z)$, we followed a three step process. First, an average axial detection voltage vs. bead position curve was acquired by scanning beads fixed to the sample surface through the detection laser (Fig. 3.3 A). Second, this average voltage curve was used to reconstruct the detection voltage curve for individual trapped beads (Fig. 3.3 B). Third, this reconstruction was fit with a 7th order polynomial (Fig. 3.3 C) to give the relative displacement calibration $\Delta z_{bd}(V_z)$ for each individual bead.

In the first step of this process, we established an average axial detection voltage vs. bead position curve $V_z(z)$ based on beads fixed to the sample surface. Ten beads, fixed to the sample surface, were scanned axially through the detection laser using the calibrated piezo stage while V_z at the back-focal plane was recorded. The obtained V_z vs. axial stage position (z_{stage}) curves were each fit to the following equation, adapted from Pralle et al. 1999 [18],

$$V_z(z) = V_{off} + I_c \left(1 + \left(\frac{z - z_{off}}{z_0} \right)^2 \right)^{-1/2} \sin\left(\pi \arctan\left(\frac{z - z_{off}}{z_0}\right)\right). \quad (3.2)$$

The axial position, z , is the relative bead position in the laser, which here is equivalent to

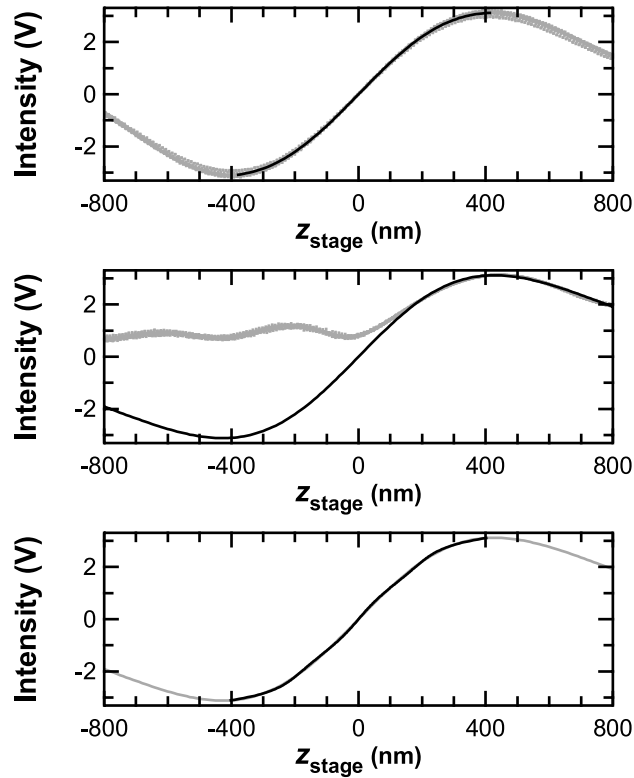


Figure 3.3: Axial detection displacement calibration. (*Top*) Step 1: A master curve (*black line*) is generated by fitting axial scans of 10 different stuck beads (*gray dots*). Each axial scan is fit to the Pralle Equation. The Pralle fit coefficients are averaged to generate the Pralle master curve. (*Middle*) Step 2: The Pralle master curve is used to reconstruct a Pralle fit (*black line*) for free bead axial scans (*gray dots*). 10 different free bead scans are plotted. Each scan is fit to the Pralle master curve with floating offsets to generate the Pralle reconstruction. The average Pralle reconstruction is plotted here. (*Bottom*) Step 3: A 7th order polynomial is fit to the Pralle reconstruction, with axes switched, to provide the $nm(V)$ displacement calibration.

z_{stage} since the bead is fixed to the sample surface. I_c , z_0 , V_{off} , and z_{off} are fit parameters; π is simply a scaling factor and does not affect the fit quality. The acquired curves for 10 different 330 nm dia. beads are shown in Fig. 3.3 A (*gray dots*) with the voltage and axial offsets (V_{off} and z_{off} in Eq. 3.2) subtracted. The shape of the curves was very consistent from bead to bead; a calculation of variability in the curve shape fit parameters yielded 2.7% for I_c and 0.42% for z_0 (100*standard deviation/mean). This consistency in the shape parameters establishes support for the using the average fit to establish a "master curve" for calibrations of trapped beads. The average fit to Eq. 3.2 is plotted as a black line. This average fit provided the "master curve" for the next step: reconstructing the full axial detection voltage curve for individual trapped beads.

In the second step of the relative axial displacement calibration, the "master curve" generated in the first step was used to reconstruct the $V_z(z)$ curves for individual trapped beads. For trapped beads not fixed to the sample surface, a V_z vs. z_{stage} scan results in a curve with two distinct regions: a peaked upper region where the bead is trapped against the sample surface and therefore tracks the position of the surface, and a lower region where the bead has reached the axial trap equilibrium point and the sample surface drops away from the trapped bead. In the peaked upper region, since the bead is following the motion of the stage, the curve provides information about the axial bead position relationship with V_z . In contrast, in the lower region below trap equilibrium, the bead is not closely following the motion of the stage and does not provide adequate information about the relationship between V_z and the bead position below trap equilibrium. Since most measurements involve exerting force by lowering the sample surface and pulling the bead below trap equilibrium, this lower region of the curve is the most relevant portion. To provide the relationship between V_z and the bead position below trap equilibrium, we reconstruct the full $V_z(z)$ curve based on the "master curve" determined in the first step of the calibration and customized to fit the upper region of the V_z vs. z_{stage} curve for the individual trapped bead.

To provide a basis for this reconstruction of the full $V_z(z)$ curve, a V_z vs. z_{stage} scan

was performed on each individual bead. The individual bead was trapped and the stage was scanned axially while the $V_z(z)$ curve was recorded. The upper region of this curve (from 100 nm above the peak to 325 nm below the peak) was fit to Eq. 3.2. The fit was performed with fixed values of I_c and z_0 from the "master curve" determined in the first step of the calibration and floating values of the voltage and axial offsets (V_{off} and z_{off}) to allow customization of the fit for the individual bead. The acquired curves for ten trapped 330 nm dia. beads are shown in Fig. 3.3 *B* (*gray dots*) with the voltage and z offsets subtracted. The figure shows excellent overlap of the individual free bead curves, indicating the reproducibility of the shape of these curves. The average reconstruction of the full $V_z(z)$ curve (also with axial and voltage offsets subtracted) is plotted as a black line. Though the plot shows the average reconstruction with offsets subtracted, these offsets are the floating parameters that allowed each reconstruction to be customized for the individual trapped bead.

In the third and final step of the axial displacement calibration, $\Delta z_{bd}(V_z)$ was given by fitting a 7th order polynomial to the reconstructed curve (Fig. 3.3). The fits were performed with the axes of this curve exchanged, i.e. z_{stage} vs. V_z , fitting from voltage peak-to-peak so that the curve is single valued. This 7th-order polynomial, fit to the Pralle reconstruction for trapped beads, was the calibration curve that provided the means for measuring Δz_{bd} .

3.3.2 Determination of axial trap equilibrium

Once the relationship between the relative axial displacement and the axial detection voltage $\Delta z_{bd}(V_z)$ was established, to fully measure the axial bead displacement from trap equilibrium, we still needed to determine the point on the $V_z(z)$ curve that corresponded to trap equilibrium, i.e. where $z_{bd} = 0$. For consistency, we first established a reference point on the curve: the peak of the axial detection voltage curve. The position of this peak was precisely determined by a parabolic fit to a region ± 200 nm from the maximum voltage point (Fig. 3.4 *A*). From this peak reference point, we could determine the offset that would

represent trap equilibrium, the point on the curve where $z_{bd} = 0$.

The point on the $V_z(z)$ curve corresponding to $z_{bd} = 0$ varied with height above the surface. We see this height variation in Fig. 3.4 *B* as the voltage oscillations in the gray curve that occur as the sample surface drops away from the trapped bead. Though the bead in this figure remained at trap equilibrium as z_{stage} dropped from 0 to -1000 nm, the voltage representing this equilibrium position oscillated. Thus for an accurate measurement of the trap equilibrium voltage, we customized the estimation of the $z_{bd} = 0$ point for the planned measurement height.

The height-dependent $z_{bd} = 0$ estimation is illustrated graphically in Fig. 3.4 *B*. The axial detection voltage for a trapped bead (*gray*) shows the oscillating trap equilibrium voltage as the surface drops away from the bead. The measurement height, here 110 nm from the surface, is illustrated by a vertical green line. The intersection of the green line and the gray curve gives the value of the trap equilibrium voltage at the measurement height. This voltage is illustrated by the horizontal blue line. The point where the blue line intersects the Pralle reconstruction curve (*black*) represents $z_{bd} = 0$ on the curve. The $z_{bd} = 0$ position relative to the peak reference point (*red dot*) established an offset from the peak that could be applied to any trapped bead $V_z(z)$ curve.

In practice, we completed this estimation of $z_{bd} = 0$ on several beads and established an average offset from the reference peak. To test the accuracy of this determination of $z_{bd} = 0$ we trapped a bead at equilibrium at the established height and measured the mean axial displacement, z_{bd} . The result is shown in Fig. 3.4 *C*. The mean axial displacement for this trace was 0.25 nm, but for measurements of several beads the mean displacement typically varied by ± 5 nm. This offset from the peak established the $z_{bd} = 0$ point on the curve at the planned measurement height, completing the calibrations needed to measure axial bead displacement, z_{bd} .

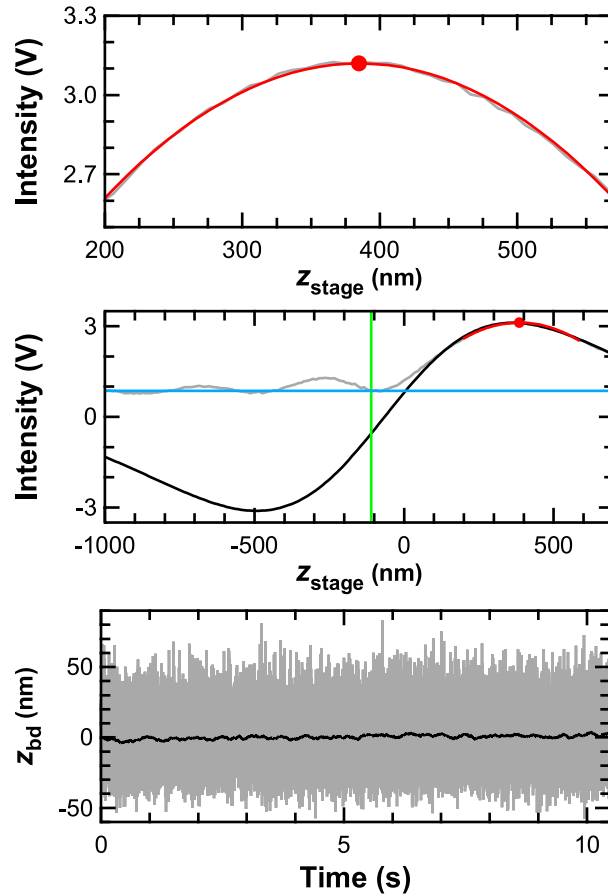


Figure 3.4: Referencing axial position from the peak of the axial detection signal. (Top) The axial detection signal from a free bead (gray) has a peak in voltage. This peak is used as a reference point for axial position measurements. The position of this peak is found by fitting to a parabola (red). The position of the peak is indicated (red dot). (Middle) Oscillations in voltage occur in the free bead signal (gray) as the sample surface is moved away from the trapped bead. At a measurement depth of 110 nm (green line), a bead trapped at equilibrium has a corresponding trap equilibrium voltage (blue line). The trap equilibrium voltage at a given measurement height represents a zero bead displacement ($z_{bd} = 0$) at that height. (Bottom) A bead, trapped at equilibrium, at a measurement height of 110 nm. The calibrated average bead displacement is 0.

3.3.3 Voltage oscillation corrections

As a second order correction to the displacement calibrations and a more sophisticated means for determining the trap equilibrium voltage, we explicitly incorporated the voltage oscillations into our calibrations. In detail, we fit the voltage oscillations for several free bead curves, added the average of these fits onto the Pralle reconstruction, and obtained the final calibration by fitting the 7th order polynomial fit to this sum of two curves. For the oscillation fits, the oscillating region below trap equilibrium was fit to a combination of 3rd order polynomial and sinusoidal functions, $P_l(z - z_0) + P_m(z - z_0)\sin(f(z - z_0))$, similarly to Neuman et al. [19]. The curves of 10 free beads (*gray*) and the average fit (*dashed black line*) is shown in Fig. 3.5 A. This average fit to the oscillations was added onto the Pralle Reconstruction at each stage height (with an offset term to yield continuity at the trap equilibrium point). The sum of these voltage curves was fit to a 7th order polynomial, performed at each stage height, yielding a calibration curve at each stage height that incorporated the voltage oscillations.

To demonstrate the improvement in the axial displacement calibration offered by fitting the oscillations, we measured the axial displacement of a trapped bead as the sample surface dropped away from trap equilibrium. The measured displacement, z_{meas} , is plotted in Fig. 3.5 B both with and without the oscillation corrections. Without the oscillation corrections (*dark gray*), the displacement from trap equilibrium deviated from trap equilibrium by as much as 74 nm, though the bead was trapped at equilibrium for the entire measurement. In contrast, with the oscillation corrections (*light gray*), the maximum measured deviation from equilibrium was < 10 nm, with a mean of -0.3 nm and std. dev. of 2.9 nm. The apparent oscillations with height were clearly diminished in the oscillation corrected calibration. These oscillation incorporations provided an axial displacement calibration that incorporated the detection voltage dependence of both the Pralle relationship, describing $V(z_{bd})$, and the oscillating affect describing $V(h_{bd})$.

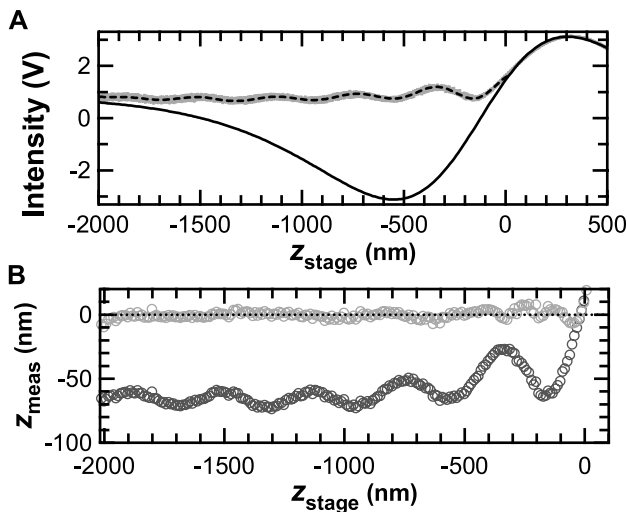


Figure 3.5: Correcting for oscillations (A) Freely diffusing beads were trapped, and the stage was scanned axially through the detection laser. The detector response is shown for 10 trapped beads (gray dots). Eq. 3.2, with I_c and z_0 values from fitting the stuck bead signals, is used to reconstruct the full detector response curve for trapped beads (black line). The oscillating region below $z_{stage} = 0$ is fit to a combination of polynomial and sinusoidal functions (dashed line). (B) Oscillations in the voltage signal are converted to displacements using calibrations without oscillation corrections (dark gray) and with oscillation corrections (light gray). The dashed line is at $z_{meas} = 0$.

3.3.4 Calibration of height above the surface

We determined the trap equilibrium height relative to the coverslip surface, z_{trap} , using a method that exploits the surface-distance dependence of the drag on a sphere, similar to the method used by Neuman and Block [13]. The surface-distance (h) dependence of the lateral hydrodynamic drag (β) on a sphere is described by Faxen's Law as

$$\beta = \frac{6\pi\eta r_{bd}}{1 - \frac{9}{16}\left(\frac{r_{bd}}{h}\right) + \frac{1}{8}\left(\frac{r_{bd}}{h}\right)^3 - \frac{45}{256}\left(\frac{r_{bd}}{h}\right)^4 - \frac{1}{16}\left(\frac{r_{bd}}{h}\right)^5}, \quad (3.3)$$

where η is the viscosity and r_{bd} is the bead radius. To determine z_{trap} , we measured the lateral drag on trapped beads at a series of axial stage positions as described below and fit to Faxen's Law; this fit determined the height of the axial trap equilibrium relative to the sample surface.

In determining z_{trap} , we first needed a reference point from which to measure. Again as in Neuman and Block [13], we chose the reference point as the peak in the axial detection voltage curve from an axial stage scan performed on a trapped bead (Fig. 3.6). Stage motion was measured from this reference point, corresponding to a stage height of 0 in Fig. 3.6.

Once the reference point was determined, we measured the lateral drag on trapped beads at a series of axial positions from the reference point. Explicitly, to measure the lateral drag, we estimated the lateral trap stiffness (k) by two different methods: the power spectral density method (k_{PSD}), which depends on the drag, and the equipartition method (k_{EQP}), which does not. In these two estimations of k , $k_{PSD} = 2\pi\beta f_0$, where f_0 is the corner frequency from the Lorentzian fit to the power spectral density of the Brownian motion of a trapped bead, and $k_{EQP} = k_B T / \langle x^2 \rangle$, where $k_B T$ is the thermal energy (Boltzmann's constant, k_B , times the temperature, T), and $\langle x^2 \rangle$ is the mean-squared Brownian motion of the trapped bead. The equations for the two methods of trap stiffness determination were equated and solved for β . In this way, we measured β at a series of axial positions.

To determine the relationship between our chosen reference point and the bead height relative to the surface, we plot and fit the measured drag coefficients (Fig. 3.6). The

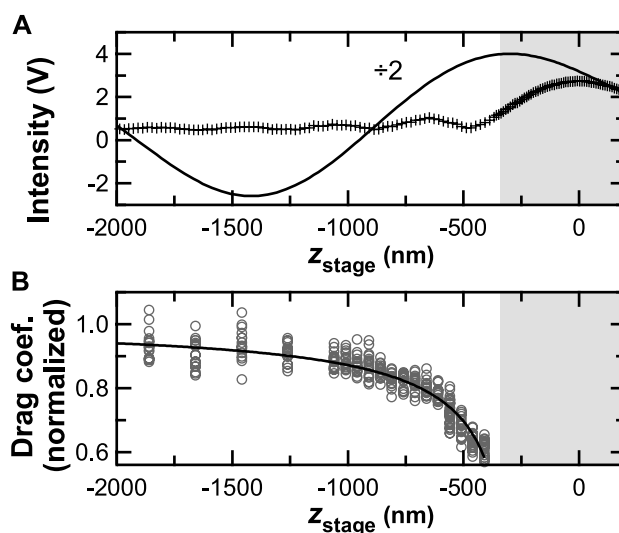


Figure 3.6: Determining trap height relative to the coverslip surface. (A) The detector response as the stage is scanned axially while simultaneously detecting a trapped bead (markers) and a stuck bead (solid line, voltage divided by 2 for display). The peak of the trapped bead detector response curve is used as a reference point for trap height determination, corresponding to 0 on the stage height axis. (B) Trap height determined by Faxens Law fit to the normalized drag coefficient as a function of height. The normalized drag coefficient was obtained from lateral stiffness calibrations via the power spectral density and equipartition theorem (gray markers). The normalized drag as a function of axial stage position was fit with Faxens Law (black line) to obtain the correspondence between stage position and trap height. The point where the bead rests on the surface is found to be 333 nm from the peak, at the intersection of the gray and white regions of the graph. In the gray region to the right of this point, the stage is pushing the bead upward in the trap. In the white region to the left of this point, the stage is dropping away from the trapped bead.

measured drag coefficients are plotted as a function of stage height from the reference peak (gray markers), normalized as β_0/β where $\beta_0 = 6\pi\eta r_{bd}$. We fit to the normalized form of Eq. 3.3, with $h = \delta(z - \varepsilon)$. Here, z is the stage motion from the chosen peak reference point and δ and ε are the free parameters in the fit: δ describes the focal shift (shift of the laser foci caused by the index mismatch at the sample surface), and ε is an offset term. We find $\delta = 0.834 \pm 0.022$ and $\varepsilon = 135.7 \pm 9.6$ nm. The estimate and error in the focal shift are similar to those found in the literature [13]. As a second estimate of the focal shift, we also fit the oscillations in the free bead signal (see section on voltage oscillations, and [19]). We found $\delta = 0.82 \pm 0.004$, within the estimated uncertainty of the focal shift found by the drag method. The point where the trap equilibrium is one bead radius from the surface is found by setting $h = \delta(z - \varepsilon) = r_{bd}$, which gives the surface offset from the peak as 333 ± 13 nm. By using this one time measurement of the height dependence of the hydrodynamic drag, the height of axial trap equilibrium z_{trap} from the surface is thus determined, referenced from the peak in the axial detection voltage curve of a bead.

On further investigation, we found the peaks in the axial detection curves acquired small offsets that varied with trap stiffness (Fig. 3.7). We measured these offsets by aligning the curves by the peak in the detection curves from stuck beads acquired simultaneously to the trapped bead scans. Fig. 3.7 shows the detector response curves from three different trap stiffnesses. The curves are aligned by the peak in the stuck bead scans such that the peak in the data from Fig. 3.6 is represented by the dashed line at 333 nm and the point where trap equilibrium would be one bead radius from the surface occurs at $z_{stage} = 0$. The offsets we measured were small (between ± 30 nm, Fig. 3.7, inset), but would be significant when trying to measure the length of a short molecule tethered to the surface.

Potentially, conditions other than trap stiffness could affect the relative position of the peaks in the axial detection curves. We considered the possibility that buffer conditions, surface coatings, DNA-tether presence and length, and day-to-day variation could potentially affect peak positions. We measured that the day-to-day variability was smaller than the the

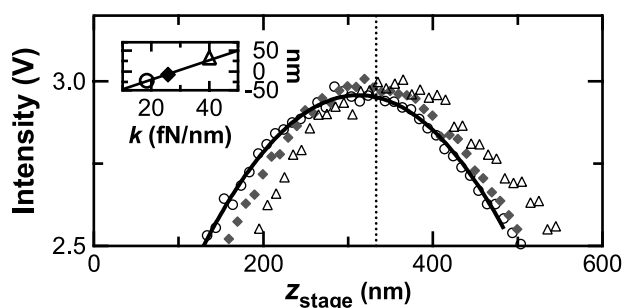


Figure 3.7: Changes in the position of the peak in the detector response curves of trapped beads. The voltage of the detector response is plotted from axial stage scans performed while trapping a bead at various trap stiffnesses. The peak positions are found by fitting a parabola to ± 200 nm from the maximum voltage point of the curves. The solid black line shows the parabola fit to the circle data points. At $z_{stage} = 0$, a trapped bead at trap equilibrium would rest on the surface, as determined in Faxen's Law fit data. The dashed line at 333 nm represents the peak position of the detector response in Faxen's Law fit data. Aligning the curves by the peaks of stuck bead scans acquired simultaneously to the trapped bead scans, the detector response curves for trapped beads are plotted for various trap stiffnesses (circles - 18.3 fN/nm, squares - 25.7 fN/nm, triangles - 40 fN/nm). The inset shows the distance from the peak in Faxen's Law fit data to the peak for each stiffness. Error bars representing the standard error on the data points are smaller than the markers.

statistical uncertainty on a given day (data not shown). For the other possible variables, we did not systematically determine their affects on the peak positions, but instead obtained the peak offset for data under each given set of conditions, eliminating the need to determine the exact effect of each condition.

3.3.5 Calibration of axial stiffness

We calibrated the axial trap stiffness, $k_{trap,z}$, by measuring the axial Brownian motion of trapped beads. As described in the trap height calibration section, the measured Brownian motion provides the means to calculate k by both the equipartition method, k_{EQP} , and the power spectral density method, k_{PSD} . When calibrating the stiffness by each of these methods, we encountered areas that required special consideration in the axial direction.

When measuring the Brownian motion of a trapped bead, we noted departures from the theoretical ideal of a perfectly harmonic trap. A plot of bead position, z vs. x (Fig. 3.8) shows an obvious apparent asymmetry in the axial direction. Plotted in histograms of bead position, in the lateral axis the x position histograms showed a nicely symmetric Gaussian distribution. In contrast in the axial direction, histograms of the z position showed an asymmetry (Fig. 3.9) that varied with height (Fig. 3.10). A plot of the theoretically calculated axial probability distribution (see Experimental Techniques chapter for details) is shown in Fig. 3.9 *D*. The asymmetry in the theoretical distribution is similar to the data asymmetry, although less pronounced. We also noted that the difference between $k_{trap,z}$ measured via the EQP and PSD methods was correlated with the asymmetries in the axial position histograms, as measured by the chi squared value for fits to a Gaussian (Fig. 3.11). These departures from the ideal harmonic trap are not surprising given that the addition of the scattering and gradient forces in the axial direction yields an asymmetric potential [31, 32, 29, 33].

When measuring the power spectral density of the axial Brownian motion of a trapped bead, we found the shape of the power spectral density to be highly dependent on the op-

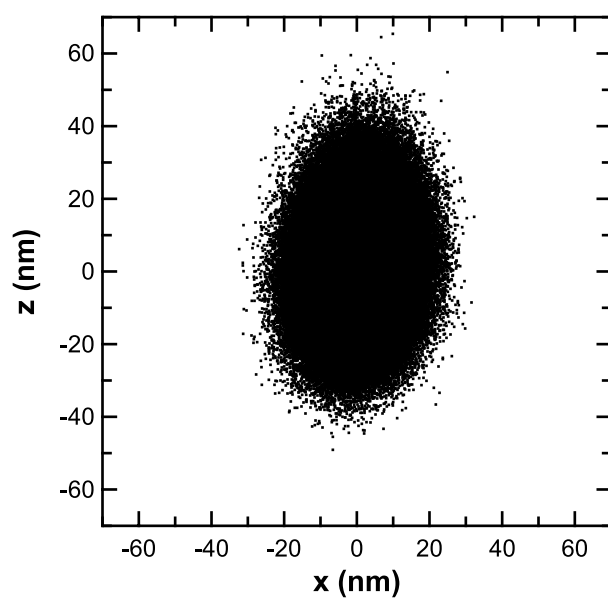


Figure 3.8: z position vs. x position of a trapped bead. Note asymmetry in the z axis.

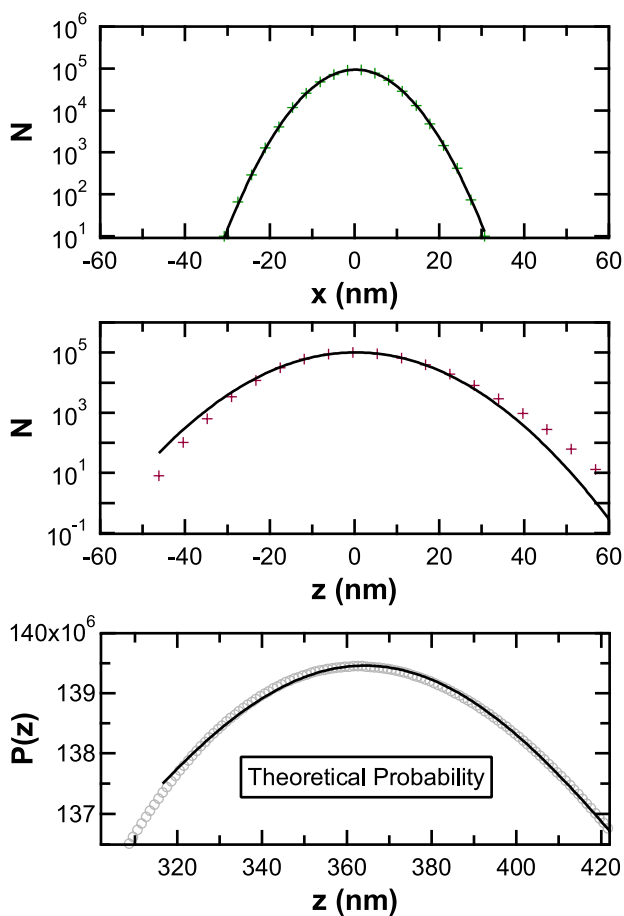


Figure 3.9: Top - Histogram of x positions (green markers) with a Gaussian fit (black line). Note symmetry and excellent fit. 2nd from top - Histogram of z positions (red markers) with a Gaussian fit (black line). Note asymmetry in histogram and lack of fit. 3rd from top - Theoretical calculation of the probability distribution of the axial positions of a trapped bead with parameters chosen to simulate the experimental conditions in our trap (gray). Details of the theoretical calculation are in the Experimental Techniques Chapter. A gaussian fit is shown in black. Note asymmetry is similar, but more subtle than in data.

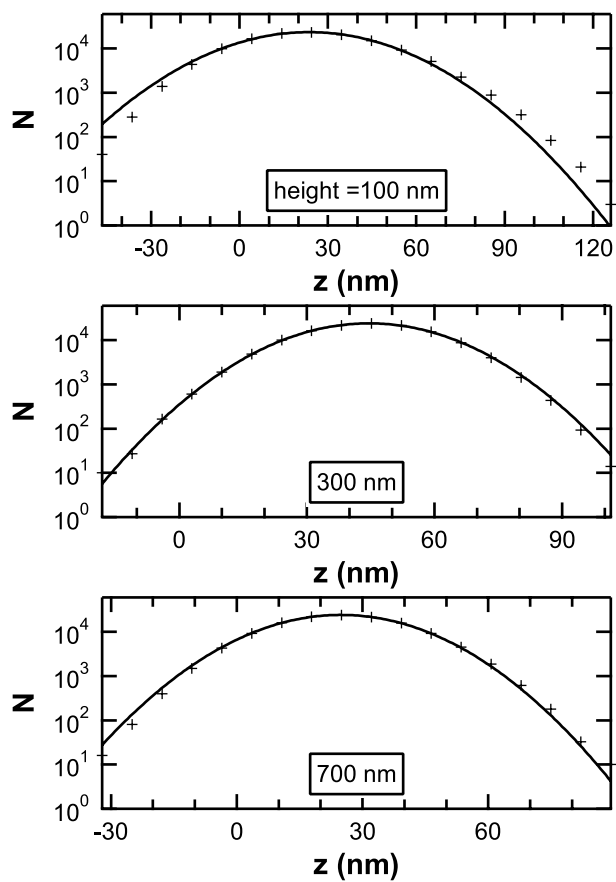


Figure 3.10: Histograms at various heights of axial positions of a trapped bead (markers), fit to a Gaussian (line). Note that the symmetry of the data and goodness of the Gaussian fit is much better at 300 nm and 700 nm, and poor at 100 nm.

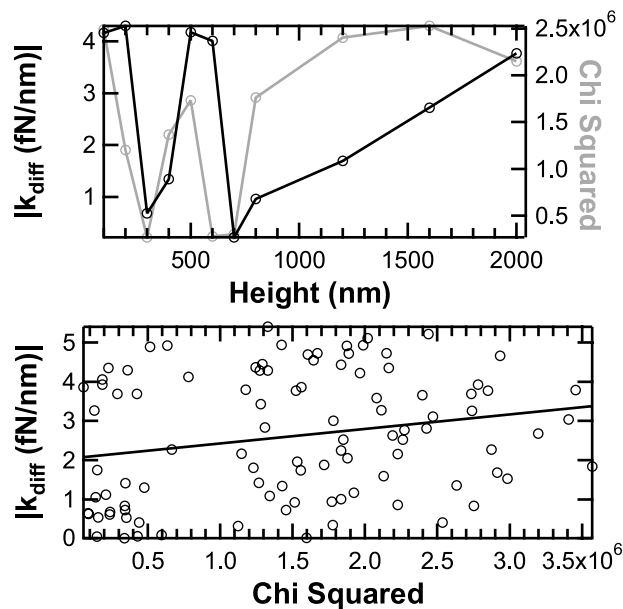


Figure 3.11: EQP asymmetry vs. height. (Top) Variation with height of stiffness agreement and chi squared from Gaussian fits to histograms. In black, the absolute value of the difference between k_z calculated via PSD and EQP is plotted vs. height. Note agreement between methods varies with height, with closer agreement at 300, 400, 700, and 800 nm. In gray, the chi squared values are plotted for each height. Note correlations between improved stiffness agreement (small k_{diff}) and goodness of Gaussian fit (small chi squared). (Bottom) Stiffness agreement vs. chi squared values. A linear fit shows a small positive slope, suggesting some correlation between the values.

timization of the intensity stabilization. This relationship was not surprising, given that the axial detection voltage is a measure of intensity. Thus intensity noise would directly manifest as axial detection voltage noise. We demonstrated this intensity stabilization dependence of the power spectral densities in Fig. 3.12, which shows power spectral densities for four conditions. In *A*, an unoptimized servo caused a significant spurious peak. This peak corresponded to a servo setting where the intensity noise peak had not been tuned to a high enough frequency, and thus the intensity noise peak showed up significantly in the power spectrum. In *B*, the power spectrum was affected by residual intensity noise even with an optimized servo. The residual noise results in a non-Lorentzian shape, clear from the attempt at a Lorentzian fit (*black*). In *C*, the power spectral density of a bead fixed to the surface reflected residual noise despite our active stabilization. In *D*, the differential power spectrum, subtracting the power spectrum of the bead fixed to the surface from that of the trapped bead, resulted in a far more Lorentzian shape. Ultimately, the servo optimization proved important for the resulting f_0 from the Lorentzian fits to the power spectral densities. Surprisingly, however, the improvement in the Lorentzian shape in the differential power spectrum changed the estimated k_{PSD} by an insignificant amount ($< 2\%$).

Keeping in mind these special considerations for the axial measurements, we calibrated k_{trap} in x and z by both equipartition and power spectral density methods as a function of laser power. We performed the calibration at an axial stage position of 1200 nm while actively stabilizing the sample position and laser intensity. The linear relationship obtained between k_{trap} and laser power (measured by the intensity servo control voltage, see Experimental Techniques for conversion of V_{servo} to power) is shown in Fig. 3.13. In x , the slope of $V(k)$ derived from the PSD and EQP measurements differed by $< 3\%$. In z , the slope values differed by $< 2\%$. However, $k_{PSD,z}$ values were far more linear, with a very small offset from 0 when fitted with a line, whereas $k_{EQP,z}$ values had a significant offset from 0 when fitted with a line without 0 fixed. Due to this offset and the significant axial asymmetries we based our axial stiffness calibrations on the k_{PSD} measurements.

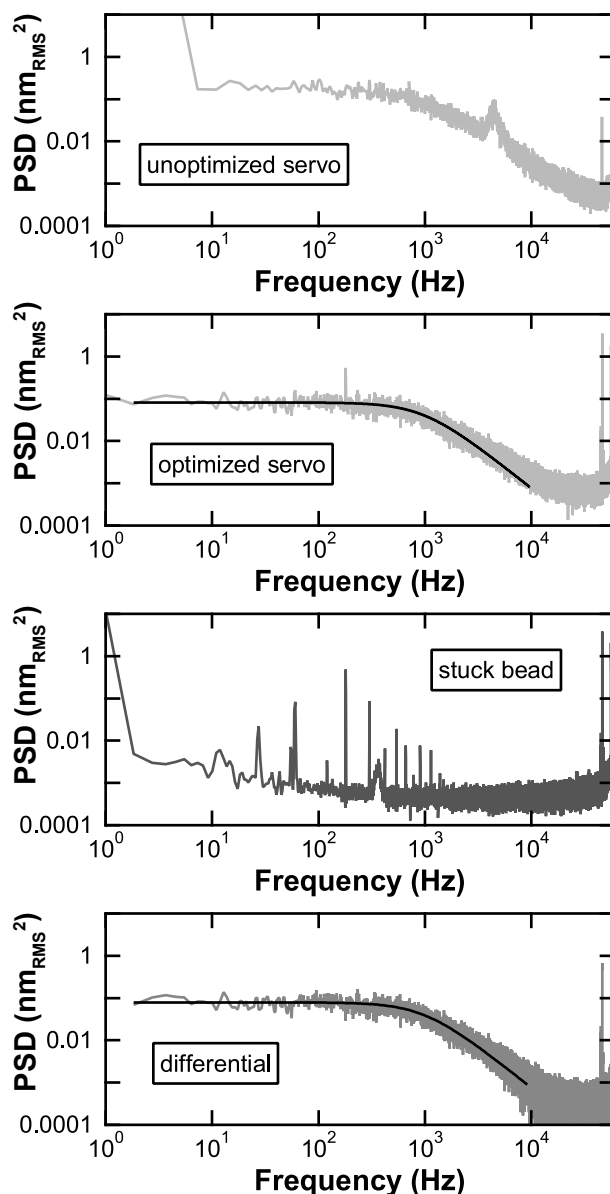


Figure 3.12: Axial power spectral densities (PSDs). top - Power spectral density of a trapped bead with an unoptimized servo. The servo was intentionally unoptimized by changing the coarse gain. Note the peak in the PSD that results. 2nd from top - PSD of a trapped bead with the servo optimized (gray) and the Lorentzian fit from Labview (black). 3rd from top - PSD of a salt-stuck bead. 4th from top - Differential PSD (gray), calculated by subtracting the stuck bead PSD from the trapped bead PSD. Note the improvement in the Lorentzian fit (black).

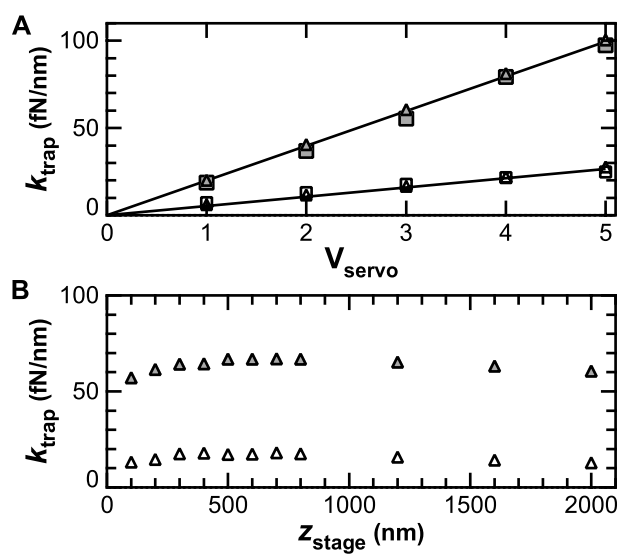


Figure 3.13: Axial trap stiffness calibrations. (A) Trap stiffness in x (solid gray markers) and z (open markers) as a function of servo control voltage. Power spectral density measurements (triangles) and equipartition theorem measurements (squares) show good agreement between the two different methods. (B) Trap stiffness as a function of axial stage position.

Because the trap stiffness has been shown to change as a function of trap height [21, 13, 19, 46, 47], we also calibrated the trap stiffness as a function of height (Fig. 3.13). To apply this height dependent calibration, we consider that the k_{trap} vs. power calibrations were acquired at $z_{stage} = 1200$ nm, and we typically performed measurements with z_{stage} between 90 and 200 nm. According to this k_{trap} vs. height calibration, $k_z(1200) = 14.9pN/nm$, $k_z(100) = 12.3pN/nm$, giving a 17.4% correction to k_z . We took this height-dependent stiffness correction factor into account in our estimations of $k_{trap,z}$.

3.4 UNCERTAINTY ESTIMATES OF CALIBRATION

The previous section describes calibrations of the relative axial bead displacement (Δz_{bd}), the position of axial trap equilibrium ($z_{bd} = 0$), the trap height (z_{trap}) and the axial trap stiffness (k_{trap}). Based on these calibrations, we wished to make measurements of DNA extension, DNA extension changes and force on a trapped bead. To know the uncertainty in our final measurements, we quantified the uncertainty in each of these calibrated quantities.

We quantified the uncertainty in the axial calibrations by several methods. We compared the measured vs. requested motion of beads fixed to surfaces, both for the 330 nm beads used in our trapped bead measurements and for 860 nm beads used as fiducials for stabilization in our measurements. We trapped beads at equilibrium and measured their apparent deviations from equilibrium, both with and without incorporating the oscillation corrections (w/ and w/out osc. cor.). We compared axial trap stiffness obtained by multiple methods. We quantified the uncertainty remaining from the fits in our z_{trap} calibration data, and finally we attempted DNA force vs. extension curves. Table 3.1 summarizes the uncertainty measurements described in this section.

3.4.1 Uncertainty by measurements on beads fixed to the surface

As a test of the accuracy of Δz_{bd} , we compared the measured vs. requested positions of beads fixed to the sample surface while stepping the sample back-and-forth with the

Table 3.1: Uncertainty estimates of axial calibration.

Experiment and Analysis	Quantity	Estimated uncertainty
fixed bead $z_{measured}$ vs. $z_{requested}$	Δz_{bd} (fixed)	4%
trapped bead deviations w/out osc. cor.	$z_{bd} = 0$	65 nm
trapped bead deviations w/ osc. cor.	$z_{bd} = 0$	30 nm
trapped bead deviations w/out osc. cor.	Δz_{bd} (trapped)	20%
k_z PSD vs. EQP at 1200 nm	k_{ztrap}	2%
Fits in z_{trap} calibration	z_{trap}	± 13.3 nm
DNA force vs. extension	z_{bd}, z_{trap}, k_z	uninterpretable

pre-calibrated piezo stage. First we performed the three-step axial displacement calibration method for trapped beads on 330 nm dia. salt-stuck beads. Next, the piezo stage was oscillated in 1 nm and 5 nm steps in z . The axial detection response was recorded, and the displacement calibration used to give the measured axial displacement (z). The measured axial displacement vs. time is shown in Fig. 3.14 A, smoothed and decimated to 100 Hz (light gray - 1 nm steps, dark gray - 5 nm steps) and 10 Hz (black).

We quantified the accuracy of the measured step size by two methods. In the first method, the 10 Hz data was histogrammed in 0.1 nm bins (Fig. 3.14 A, right, light gray - 1 nm steps, dark gray - 5 nm steps). The histogram of each set of steps was fit to two Gaussians. The average quantities obtained from 9 traces yielded peak separations (mean \pm std. dev.) of 0.99 ± 0.1 nm (1 nm steps) and 4.89 ± 0.22 nm (5 nm steps). The second method of determining the measured step size was to calculate the pairwise distance distribution (PDD). The PDD for the 10 Hz stepping data was calculated by subtracting each data point from every other data point [49]. The histograms of the PDDs are shown in Fig. 3.14 B, with 0.1 nm bin widths (light gray - 1 nm steps, dark gray - 5 nm steps). Each PDD histogram shows three peaks, which were fit with three Gaussians (black lines) to obtain peak values (mean \pm std. dev.) of $\pm 4.9 \pm 0.25$ nm and $\pm 0.96 \pm 0.18$ nm. The average peak difference in the histograms for 9 different traces is taken as the limit of the accuracy of a relative displacement measurement, and the std. dev. of the peak difference is the precision.

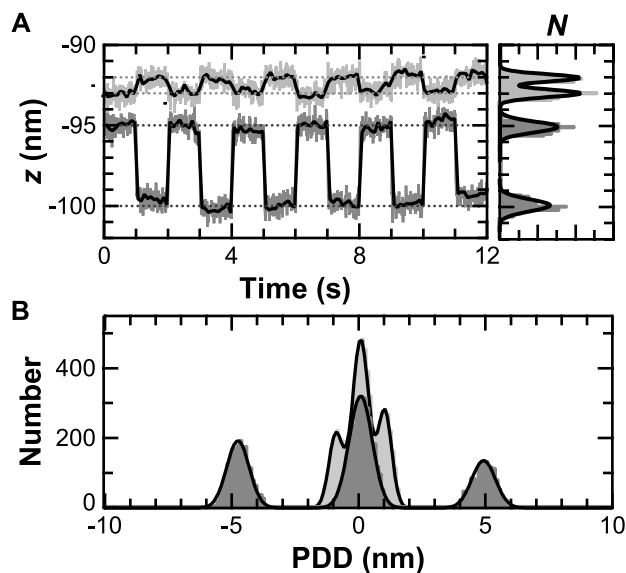


Figure 3.14: Accuracy of calibrated axial measurements. Stuck bead signals were calibrated using the method described for free beads. The stage was oscillated in 1 and 5 nm steps to test the resolution and accuracy of the calibrated z measurements. (A) Examples of measured axial steps smoothed to 100 Hz (1nm - light gray, 5 nm - dark gray) and 10 Hz (black). The dashed lines are spaced at 1 and 5 nm intervals. Histograms of 10 Hz stepping data with two Gaussian fits to each set show the peak separation to be 0.99 ± 0.1 nm and 4.89 ± 0.22 nm (mean \pm std. dev. for 9 traces). (B) The Gaussian fits (black) of pairwise distance distributions from 9 different traces have peaks for the 1nm steps (light gray) at $\pm 0.96 \pm 0.18$ nm and for the 5 nm steps (dark gray) at $\pm 4.9 \pm 0.25$ nm.

If we translate these measurements to percent differences between the measured and requested displacements, the uncertainty in Δz_{bd} measured by this method is quite small ($1 - 4\%$). However, this measurement provides no information about the uncertainty of the trap equilibrium ($z_{bd} = 0$) position. Also, this measurement is really a lower limit on the uncertainty of Δz_{bd} of a trapped bead, because of differences between the detection signal of a stuck bead and a trapped bead.

For completeness, we also determined axial displacement calibrations for large (860 nm) stuck beads used as fiducials in stabilizing the coverslip surface relative to the laser focus. A representative detector response vs. axial stage position curve is shown in Fig. 3.15 A (*gray markers*). The curve was fit to 7th order polynomials in two separate regions to obtain a shallow calibration, (solid line) and a deep calibration (dashed line).

As a metric to test the accuracy of the fiducial axial displacement calibration, we used these shallow and deep calibrations to convert the detector response voltage to measured axial position (z_{meas}). The measured axial position vs. requested axial stage position (z_{req}) is plotted for the shallow (Fig. 3.15 B) and deep (Fig. 3.15 C) regions (*gray markers*). The measured vs. requested positions were fit to a line, obtaining a slope of 1.0057 ± 0.0022 and offset of 2.89 ± 1.1 in the shallow region, and a slope of 1.0027 ± 0.00158 and offset of 4.53 ± 2.5 in the deep region. The residuals are shown for each linear fit. The extremely small deviation of the fitted slopes from an ideal slope of 1 represent the very small percent uncertainty for the displacement calibrations on the fiducials used for stabilization. The small offsets represent small systematic offsets for the measured positions for these fiducials. Because these uncertainties were so small, and because they represent uncertainties for the fiducial rather than the trapped bead, they are not included in the table summarizing the uncertainties in the axial calibration.

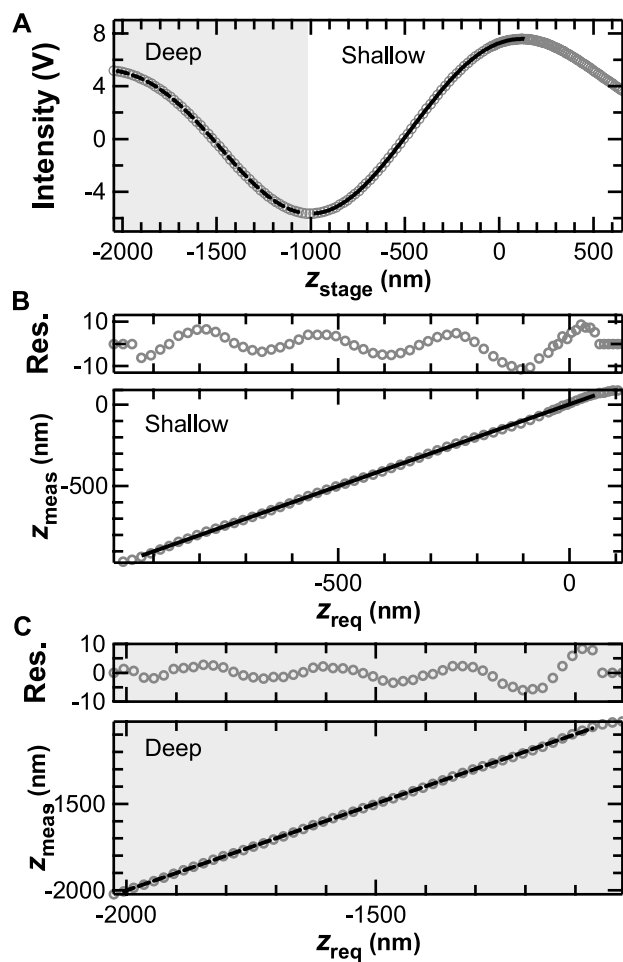


Figure 3.15: Accuracy of calibrated axial measurements for fiducial. (A) Seventh-order polynomials are fit to the shallow (solid line, white background) and deep (dashed line, gray background) regions of the stuck bead curve. (B) The calibration is used to convert the voltage signal (markers) to the measured z (z_{meas}) vs. the requested z (z_{req}) in the shallow region. A linear fit yields a slope 1.0057 ± 0.0022 and offset of 2.89 ± 1.1 . Residuals are shown for the linear fit. (C) Same as B, for the deeper region. The slope is 1.0027 ± 0.00158 and offset is 4.53 ± 2.5 in the deep region. The residuals are shown for each linear fit.

3.4.2 Uncertainty by trapped bead deviations from equilibrium

As another quantification of the uncertainty in our calibrated quantities, we measured the apparent deviations from equilibrium for a bead trapped at equilibrium as we moved the sample surface. With no external forces on the trapped bead, the average position of the bead should remain at equilibrium, i.e. $z_{bd} = 0$. However, as described, the axial detection voltage oscillates as the sample surface drops away from trap equilibrium. We quantified this uncertainty both with and without oscillation corrections incorporated into the displacement calibration.

Without oscillation corrections, we saw previously in Fig. 3.5 that apparent deviation from trap equilibrium was as large as 74 nm. Thus depending on the measurement height and the height where $z_{bd} = 0$ was determined, $z_{bd} = 0$ could be off by up to the full amplitude of that largest oscillation. I often determined $z_{bd} = 0$ between 100-150 nm from the surface, which is near the bottom (-65 nm) of the first oscillation. With trap height changes, and/or unaccounted changes in bead height due to the DNA tether, $z_{bd} = 0$ could be off by as much as 65 nm.

With oscillation corrections incorporated, we measured apparent deviations from trap equilibrium of as much as ± 10 nm. Also, depending on the bead, the average measured z_{bd} position was sometimes closer to +10 or even +20 nm. This measurement means that even with oscillation corrections, $z_{bd} = 0$ could be off by up to 30 nm (20 nm average + 10 nm remaining oscillations).

These oscillations also illustrate the increased uncertainty in Δz_{bd} when measuring the relative position of a stuck bead vs. a trapped bead. For trapped beads, the largest of these oscillations, $z_{meas} = 65 - 25 \text{ nm} = 40 \text{ nm}$ uncorrected, occurs between 150 and 350 nm depth. This slope (0.2) can be interpreted as a 20% potential error in a Δz_{bd} measurement taken along this slope. With a stationary surface, if a trapped bead moved from 350 to 150 nm ($\Delta = 200 \text{ nm}$) in depth, it would only have appeared to move 160 nm, a 20%

underestimation. On another part of the curve, the motion could actually be overestimated by 20% due to these oscillations. However, the error in Δz_{bd} should not be larger than 20%, because if the bead moved from one oscillation to the next, the opposite directions of the slopes would actually cancel out some or all of the error.

3.4.3 Uncertainty by trap stiffness measurements

The next method for estimating uncertainty was a comparison of axial trap stiffness measurements by equipartition and power spectral density, k_{EQP} and k_{PSD} . The difference between $k_{trap,z}$ estimated by the two methods provides an estimate of the uncertainty in $k_{trap,z}$. For the measurements of $k_{trap,z}$ as a function of intensity, the measured slopes were within 2% of each other, yielding an estimated average uncertainty in $k_{trap,z}$ of 2%. This average uncertainty is actually substantially lower than the uncertainty in $k_{trap,z}$ introduced by variations in bead size. According to the manufacturer, the bead size coefficient of variation is 4%, which leads to a 12% variation in $k_{trap,z}$, since $k_{trap,z}$ is proportional to the volume of the beads. Thus the bead-to-bead variation in $k_{trap,z}$ of 12% is larger than the uncertainty estimated by measuring $k_{trap,z}$ by the two different methods.

Another uncertainty estimation based on trap stiffness measurements is based on the z_{trap} calibration in Section 3.3.4. The estimated uncertainty in z_{trap} from this method is simply the fitting error in the Faxen's Law fit obtained to the lateral drag vs. height data. This uncertainty estimate for z_{trap} was ± 13.3 nm.

The above measurements, combined with previous measurements during the course of calibration, provided estimates of the uncertainty of the various quantities of our calibration. From the summary of uncertainty quantifications in Table 3.1, we can see that the uncertainty estimate is smallest (2%) for the trap stiffness (k_{trap}), and larger but still reasonable ($< 20\%$) for the relative axial displacement (Δz_{bd}). The estimated uncertainty in z_{trap} is not large (± 13.3 nm), but is difficult to manage if an experiment aims to measure quantities near the sample surface. In contrast, the uncertainty for the trap equilibrium location ($z_{bd} = 0$)

is substantial, especially without the oscillation corrections (65 nm). From our uncertainty estimations, we expect we can estimate k_{trap} and measure relative axial displacements well. However, mostly due to the large uncertainty in $z_{bd} = 0$, we would have large uncertainties when measuring extension of molecules ($Ext = z_{trap} - z_{bd}$) and force ($F = k_{trap} * z_{bd}$). The next section described in detail how these uncertainties would be expected to impact measurements of DNA force and extension.

3.4.4 Uncertainty by DNA force and extension

Another method for estimating the uncertainty in the axial calibration was the DNA force vs. extension measurements. In this method, the axial force (F) and extension (Ext) were measured on DNA molecules. Because $F = -k_{trap} * z_{bd}$ and $Ext = z_{trap} + z_{bd}$, this method relies on all of the calibrated quantities, z_{bd} , z_{trap} , and k_{trap} . This method has the potential to provide a very nice confirmation of the axial calibration if all calibrated quantities have very small errors. However, if more than one of the calibrated quantities has more than a very small error, the DNA force vs. extension measurement becomes virtually uninterpretable.

Based on the relationships listed above between the calibrated quantities and the measured force and extension, we can predict the effect on the DNA force vs. extension curve. These predicted effects are summarized in Table 3.2. An error exclusively in k_{trap} could be easily identified, as the F vs. Ext curve shape would simply appear distorted in the force axis. A systematic error in z_{trap} would also be easily identified, as the curve shape would simply be offset on the extension axis. An error exclusively in trap equilibrium ($z_{bd} = 0$) could also potentially be identified, as the curve would be simply shifted towards the upper left quadrant (bigger F , smaller Ext) or the lower right quadrant (smaller F , bigger Ext). These three examples assume the error is constant over the relevant portion of the curve. An error in the relative displacement measurement Δz_{bd} would be very difficult to identify, as it would skew both the force axis and the extension axis, resulting in an oddly shaped

curve. But in the least interpretable example, if non-negligible errors occur in more than one calibrated quantity, the result of a shifted and distorted curve would be uninterpretable. Unfortunately, this last example seems to be the case for our data.

Table 3.2: Force vs. extension errors from calibration uncertainties.

Parameter with error	Resulting change in F vs. Ext curve
k_{trap}	same general curve shape, but with scaled F axis
z_{trap}	same curve shape, but shifted along Ext axis
$z_{bd} = 0$	same curve shape, but shifted to upper left or lower right quadrant
Δz_{bd}	skewed F and Ext
multiple parameters	skewed and possibly shifted F and Ext

Despite the uncertainty estimates predicted, we tested our axial measurement technique by obtaining axial force vs. extension curves on short (92 nm) DNA molecules. The DNA tethers were stretched by dropping the stage axially. The trap height z_{trap} was corrected for the focal shift by multiplying by 0.83. The extension $Ext = z_{trap} + z_{bd}$ and the force $F = -k_{trap} * z_{bd}$ were calculated from the calibrated axial quantities. The obtained force vs. extension curves are plotted in Fig. 3.16, along with the theoretical $F(Ext)$ curve from the Bouchiat-modified Marko-Siggia WLC model [22], with corrections for short DNA [25]. The persistence length used in the calculation was 19 nm, calculated using the equation from Seol et al. with $p_{infinity} = 44.5$ nm, as obtained in lateral stretching curves of 2013 nm DNA under the same conditions. The curves demonstrate the expected scenario: the curves are both skewed and shifted in such a way that no specific uncertainties can be interpreted.

Attempts at obtaining axial DNA stretching curves on long DNA proved uninterpretable as well. With long DNA (2013 nm), the force vs. extension curve curve is more well established. However, the 2013 nm DNA was so long that the trap had to be at a depth of 2000 nm to pull the DNA to forces where the stretching curve became steeper. At this depth, the reliability of the axial trap calibrations became questionable, and in a way with little relevance to the very shallow measurements we actually cared about. Thus, the axial 2013 nm DNA measurement became somewhat irrelevant. However, the lateral measurement of

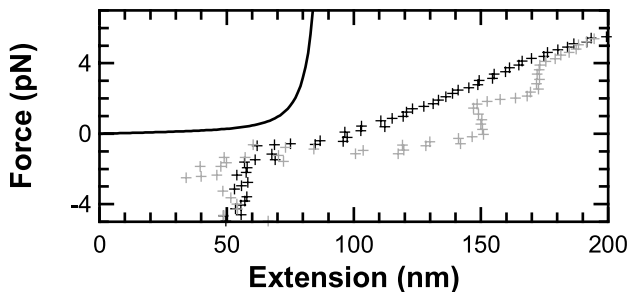


Figure 3.16: Force vs. extension, measured in the axial direction. Markers - Force vs. extension data, stretching in the axial direction and using axial detection and axial calibrations for the bead displacement from equilibrium (z_{bd}), trap height (h_{trap}), and trap stiffness (k_{trap}). The force axis was calculated via $F = k_{trap} * z_{bd}$. The extension axis was calculated as $Ext = h_{trap} - z_{bd}$. $k_{trap} = 0.0332$ pN/nm, using the axial stiffness calibration from the axial stiffness figure, with the height correction at 100 nm (i.e. $k_{100} = 0.87 * k_{1200}$). Trap height was calculated using the trapped bead peak as a reference, with the surface offset from Faxen's Law fit and the peak corrections for stiffness, then correcting for the focal shift by multiplying by a factor of 0.83. Black markers - The displacement calibration was performed via the Pralle reconstruction, using the simple peak offset method for determining the trap equilibrium voltage (as in TBP data). Gray markers - The displacement calibration was performed by adding the oscillation corrections on top of the Pralle reconstruction. Line - Theoretical force vs. extension curve. The curve was calculated using a modified WLC model [22] with a contour length of 92 nm and persistence length of 19 nm. The 19 nm persistence length was calculated using the empirical formula for calculating p of short DNA [25] with $p_{\infty} = 44.5$ nm (calculated from 2013 nm DNA lateral stretching in experimental methods section).

the 2013 nm DNA provided a good measure of the persistence length, which was needed to provide the theoretical force vs. extension curve for the short DNA.

3.5 IMPROVED AXIAL FORCE AND EXTENSION ESTIMATIONS

3.5.1 Estimating force from data traces

Because of the larger uncertainties in the estimation of the trap equilibrium position and trap height, we needed a different method to measure the force and extension of a molecule axially. While a general estimation of the force and extension would be useful, what is most meaningful for our data is a specific estimation of the force and extension for the actual measurements we obtained. For our TBP data, we obtained measurements at three different forces, nominally $F = 0.08, 0.3$ and 1 pN. Therefore, we needed to obtain our separate estimation of the force and extension at these forces.

We obtained this improved estimates of the force and extension by measuring the Brownian motion of trapped, tethered beads under identical conditions to our TBP data. We analyzed the Brownian motion of trapped, tethered beads to yield estimates of the total stiffness of the tethered-bead system, k_{total} . From k_{total} and the calibrated k_{trap} , we calculated $k_{DNA} = k_{total} - k_{trap}$. From this estimated k_{DNA} and the theoretical calculation $k_{DNA} = dF/dExt$ (based on the the modified-WLC $F(Ext)$ [22], we found the force and extension that corresponded to the experimentally derived k_{DNA} . This force and extension were the final estimates for the force and extension in our TBP data.

Initially, we estimated the force and extension by estimating k_{total} via three different methods: an equipartition theorem method, a power spectral density method, and an autocorrelation method. Fig. 3.17 illustrates the Brownian motion analysis of a typical trace at the intermediate force for each of the three methods. Each method had advantages and potential drawbacks, as detailed below.

After performing these calculations on our data, we used the obtained mean k_{total}

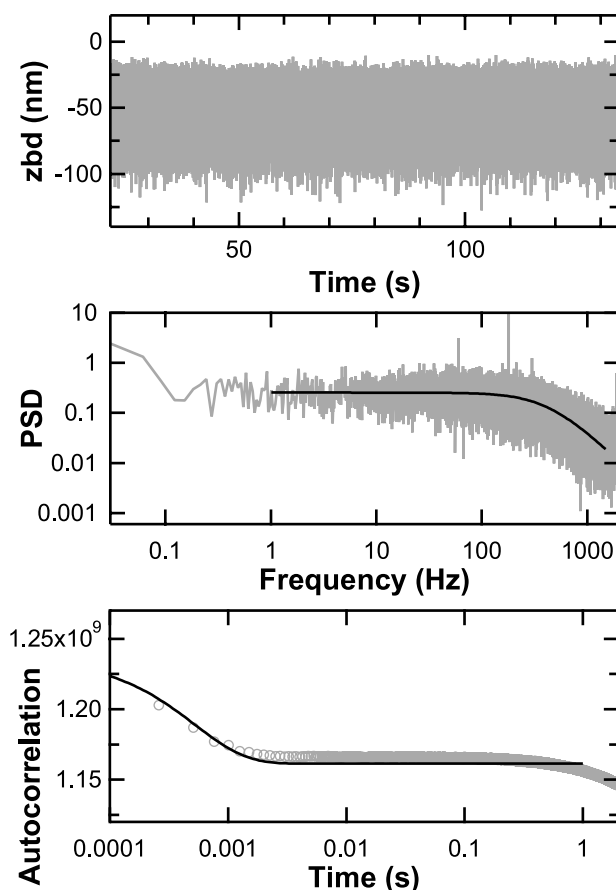


Figure 3.17: Three methods for estimating force. In each method, we analyzed tethered bead motion to calculate the total stiffness of the system (k_{total}). From k_{total} and the trap stiffness (k_{trap}), we then calculated the DNA stiffness, $k_{DNA} = k_{total} - k_{trap}$. From k_{DNA} , we found the corresponding force on the theoretical DNA stiffness curve, $k_{DNA} = dF/dExt$, where Force (F) as a function of Extension (Ext) was based on the Bouchiat-modified, Marko-Siggia WLC model for DNA. (A) Axial bead position (z_{bd}) vs. time (from intermediate force data). Here, k_{total} is calculated via the equipartition theorem (EQP). In the EQP method, $k_{total} = k_B T / \sigma^2$, where $k_B T$ is the thermal energy of the system and σ^2 is the variance of z_{bd} . (B) Power spectral density (PSD) of the z_{bd} vs. time trace (gray). Here, k_{total} is calculated via the PSD method, $k_{total} = 2\pi\beta f_0$, where β is the drag coefficient of the bead and f_0 is the corner frequency of the Lorentzian fit (black) to the PSD. (C) Autocorrelation of the z_{bd} vs. time trace (gray). Here, k_{total} is calculated from the autocorrelation time (τ) of an exponential fit (black) to the autocorrelation of the data.

and extension ($Ext = h_{bd}$) at each force to simulate trapped bead traces. (See details in Experimental Techniques chapter.) Fig. 3.18 shows simulated data and analysis. By simulating these traces at full bandwidth, then filtering, we estimated the uncertainty/error caused by the finite bandwidth in our data for each analysis method. In the simulations, analyzing the data via the power spectral density provided the closest match between input values and output values. In fact, errors between the input forces and output forces were $< 2\%$. Due to this low error, we ultimately relied on the force and extension values estimated by the power spectral density.

3.5.2 Force estimation by equipartition

In detail, for the equipartition measurement, we calculated k_{total} based on the variance, σ^2 of our data traces, $k_{total,EQP} = k_B T / \sigma^2$. We calculated σ^2 in 1 s windows to prevent misestimation from residual drift. From this estimate of k_{total} , we estimated the DNA force and extension as already described.

Comparison of the equipartition analysis of the data and simulations showed that equipartition misestimated the force and extension for at least two reasons. The simulations showed that equipartition significantly underestimated the variance on the traces filtered to 2 kHz, which translated to an overestimate in the simulations of k_{total} , Ext , and F output values compared to simulation input values. Another source of error was the anharmonicity of the trap in the axial direction. This anharmonicity is shown in Fig. 3.19 in the histograms on the left. For these simulations, the simulated traces assumed the ideal harmonic trap, as shown by the histograms on the right. The lack of symmetry and non-Gaussian distributions in the data degraded the accuracy of the stiffness measurement by equipartition in an unpredictable way. Ultimately equipartition analysis of the data and simulations did not follow the same trends, which we interpreted as being due to the competing and unpredictable affects described. Ultimately the equipartition analysis was not the best way to estimate the force.

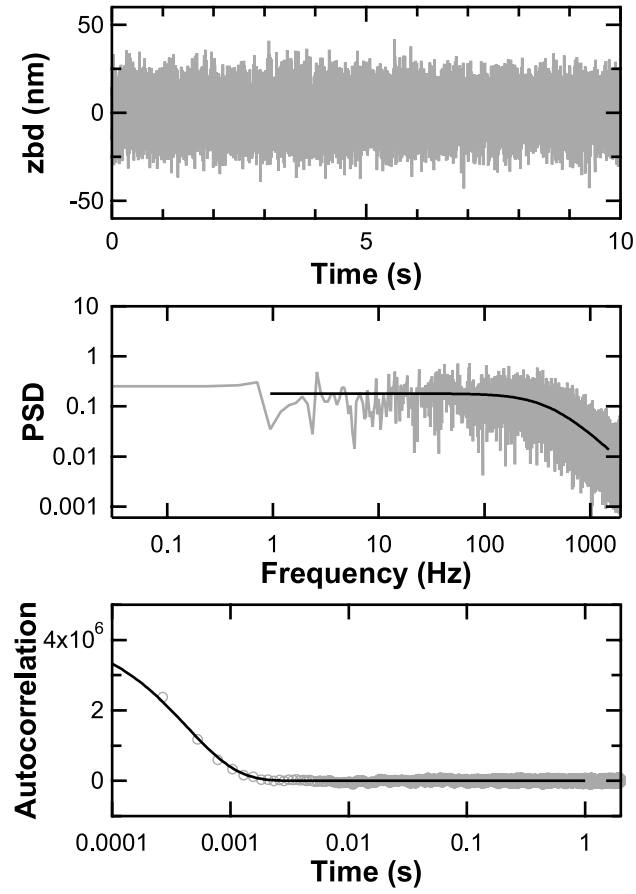


Figure 3.18: Simulation of three methods for estimating force.

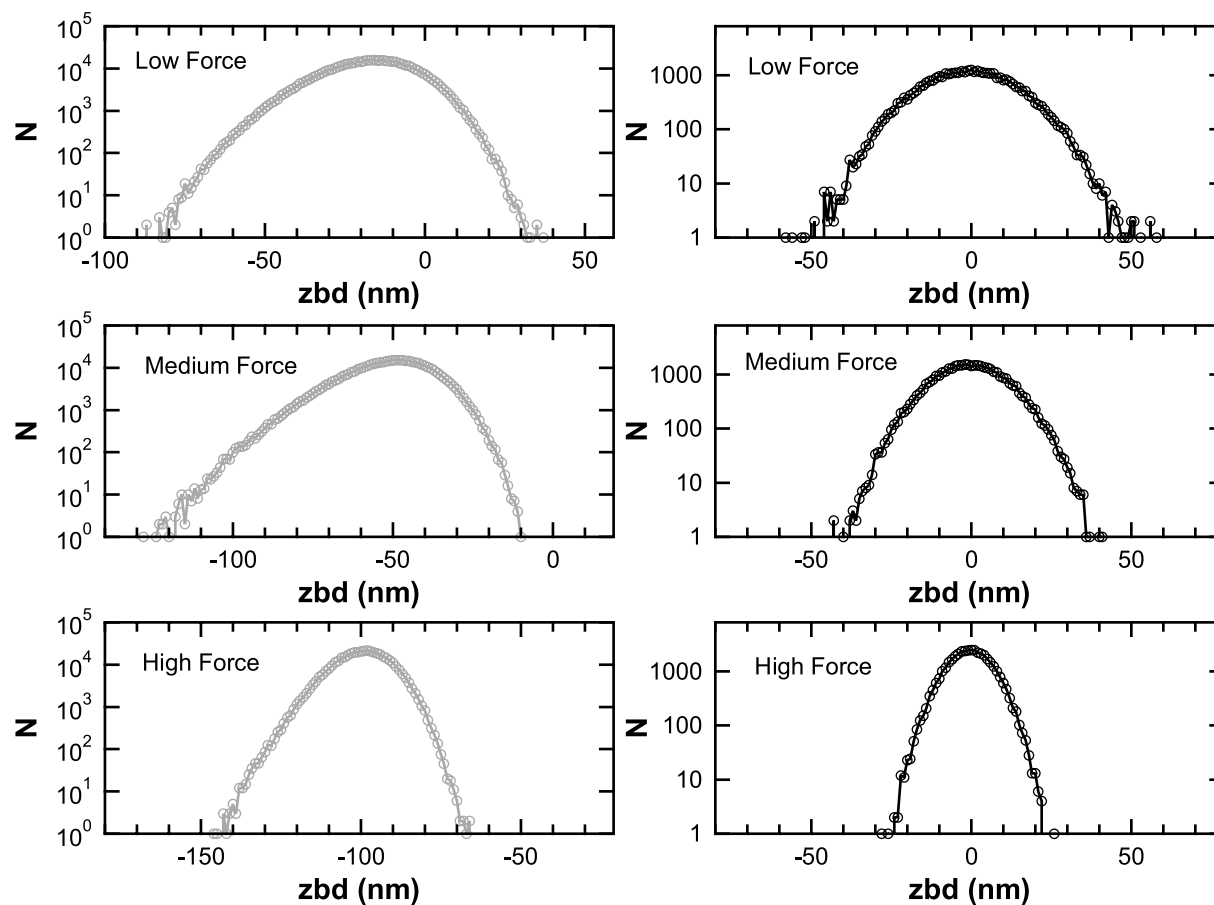


Figure 3.19: Histograms of axial bead position. Histograms of data traces (left) show a skewed, non-Gaussian position distribution. Histograms of simulated traces (right) are Gaussian and symmetric, as simulations were based on a harmonic trap. The asymmetry seen in the data histograms affects the variance calculated from the traces, and therefore affects the accuracy of the force calculated via the EQP method.

3.5.3 Force estimation by power spectral density

For the power spectral density analysis, we obtained k_{total} based on the corner frequency, f_0 of the Lorentzian fit to the power spectrum of our data traces, $k_{total,PSD}(h) = 2\pi\beta(h)f_0$, where $\beta(h)$ is the height dependent drag coefficient. We fit the region $1 < f < 1500$ Hz. The low frequency limit was to prevent skewing by residual drift; the high frequency limit was to prevent skewing by the high f tail in our data caused by an imperfect filter.

The key concept for estimating the force and extension by the power spectral density method was carrying the height dependence of the drag in the stiffness measurement $\beta(h)$ through to the estimation of the DNA stiffness, $k_{DNA}(h) = k_{total,PSD}(h) - k_{trap}$. By retaining the height dependence, we estimate $k_{DNA}(h)$ without using the error-prone trap height or trap equilibrium calibrations. Then, using the fact that $h = Ext$ for a DNA molecule stretched between the surface and a bead, we plot $k_{DNA}(h)$ on the same axes as $k_{DNA} = dF/dExt$. Fig. 3.20 shows both an example of these curves. The intersection of the two curves gives the resulting $k_{DNA} - Ext$ pair, from which we found the corresponding force.

The power spectral analysis relied on temporal properties of trace, and data was acquired at a bandwidth (4 kHz with 2 kHz antialiasing) not much faster than the corner frequency (f_0) of the power spectrum of the data. Because of this low bandwidth/ f_0 ratio, we feared fitting the power spectrum to obtain f_0 would result in inaccuracies. Fig. 3.21 shows the power spectral density and fit of the highest force (and hence highest f_0) data, and the PSD and fit of the simulation of the highest force data. The percent difference between the simulation input f_0 and the simulation output f_0 from the fit to the simulation was $< 5\%$ for all forces. This small difference between simulation input and the fit to the filtered simulation gives confidence in estimating the force and extension using the power spectral method.

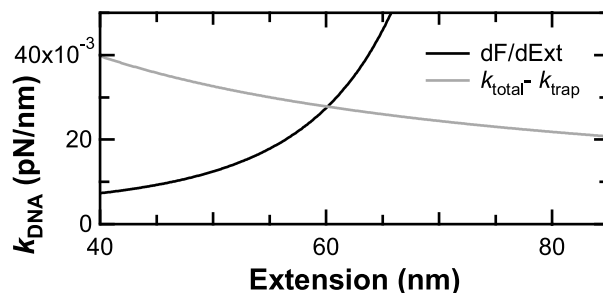


Figure 3.20: DNA stiffness vs. extension. The PSD and autocorrelation methods for calculating k_{total} from tethered bead data traces depend on the drag coefficient (β) of the bead. β depends on the height above the surface. Thus, k_{total} is a function of height, which means k_{DNA} calculated from a tethered bead data trace is also a function of height, $k_{DNA}(h) = k_{total}(h) - k_{DNA}$. For a tethered bead, the height to the bottom of the bead (h) is the same as the DNA extension (Ext). Therefore, $k_{DNA}(h)$ can be plotted as $k_{DNA}(Ext)$. $k_{DNA}(Ext)$ can also be calculated theoretically as $dF/dExt$, as described in the text. Plotting $k_{DNA}(Ext)$ calculated from a tethered bead data trace and from theory, the intersection of the two curves provides the correct k_{DNA} and Ext , which can then be used to find the corresponding force.

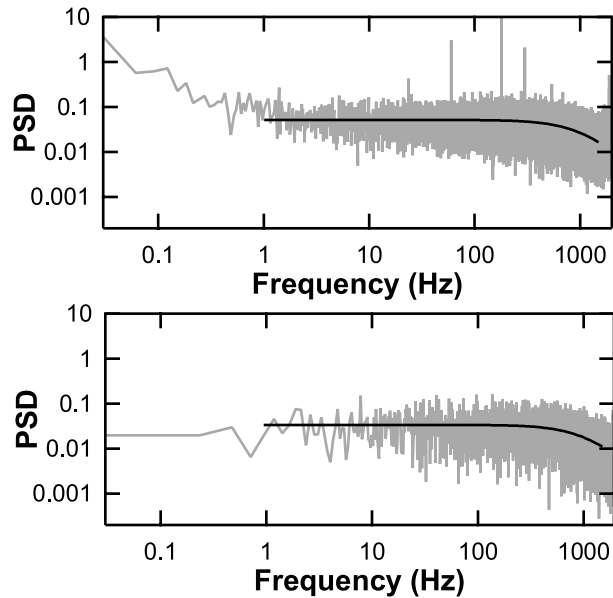


Figure 3.21: Power spectral density of highest force data and simulation. Data was acquired at a bandwidth (4 kHz with 2 kHz antialiasing) not much faster than the corner frequency (f_0) of the power spectrum of the data (1030 Hz). Because of this low bandwidth/ f_0 ratio, we feared fitting the PSD to obtain f_0 may result in inaccuracies. This plot shows the PSD and fit of the highest force (highest f_0) data (top), and the PSD and fit of the simulation (bottom) of the highest force data. The percent difference between the input f_0 for the simulation and the fit f_0 was less than 5% for every force. The agreement between the simulation input and output demonstrates the accuracy of f_0 from the PSD fit despite the low bandwidth/ f_0 ratio.

3.5.4 Force estimation by autocorrelation

For the autocorrelation method, we obtained k_{total} based on the autocorrelation time, τ , obtained from an exponential fit to the autocorrelation of the data. Here, $k_{total,tau}(h) = \beta(h)/\tau$. Similarly to the power spectral analysis, we retained the height dependence in the equations through the calculation of $k_{DNA}(h)$, plotted $k_{DNA}(h)$ and the theoretical $k_{DNA}(Ext)$, and found the k_{DNA} , extension, and corresponding force at the intersection of the curves.

Simulations indicated that the autocorrelation analysis tended to underestimate k_{total} (and therefore F and Ext), likely because of limited bandwidth. Data similarly showed $k_{total,tau}$ values smaller than the $k_{total,PSD}$ values, which simulations showed were most accurate. However, the effect between data and simulation was not quantitatively identical, possibly due to the small residual drift in data. This effect was most dramatic for the highest force data, which had the most drift. On lower force data, fitting the autocorrelation function to 1 s from the autocorrelation peak provided reasonable estimates of k_{total} . However, on high force data, when fitting to 1 s from the peak, the slope of the function skewed the autocorrelation time from the fit to the point where the k_{total} calculation became nonsensical. Narrowing the fit range to 0.1 s from the peak provided a reasonable estimate. I interpret the slope in the autocorrelation function calculated from data, which is not present in the simulation, as the cause of the non-quantitative agreement between the values of k_{total} calculated from the data and simulation.

3.5.5 Summary of final force estimates

To summarize, we estimated the force and extension from the Brownian motion of our data traces at three different forces. We estimated via the three methods described: equipartition, power spectral density, and autocorrelation analysis. For the power spectral and autocorrelation analyses, using the intersection of $k_{DNA}(h)$ by the analysis and $k_{DNA}(Ext)$ from

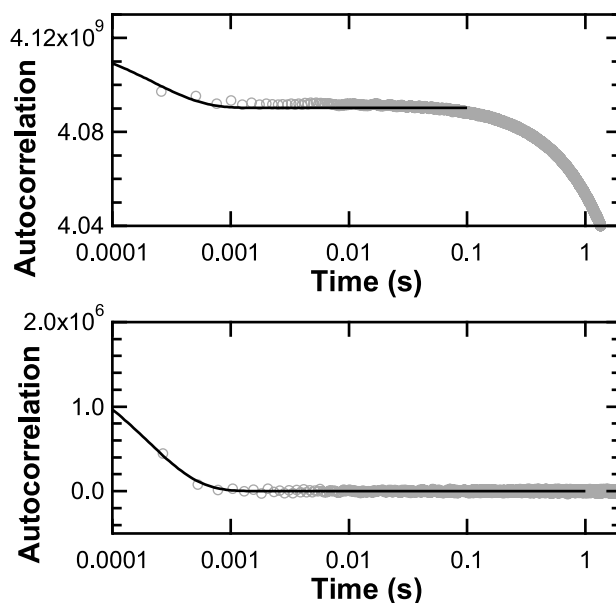


Figure 3.22: Autocorrelation of axial bead position traces. (Top) Autocorrelation of the highest force data. (Bottom) Autocorrelation of the highest force simulation. Simulations indicated that the autocorrelation analysis tended to underestimate k_{total} (and therefore F and Ext), likely because of limited bandwidth. Data also showed k_{total} values smaller than k_{PSD} values, which the simulation showed are most accurate. However, the affect between data and simulation was not quantitatively identical, possibly due to the small residual drift in data. This effect was most dramatic for the highest force data, which had the most drift. On lower force data, fitting the autocorrelation function to 1 s from the peak provided reasonable estimates of k_{total} . However, on high force data, when fitting to 1 sec from the peak, the slope of the function skewed the autocorrelation time from the fit to the point where the k_{total} calculation became nonsensical. Narrowing the fit range to 0.1 s from the peak provided a reasonable estimate. However, I interpret the slope in the autocorrelation function calculated from data, which is not present in the simulation, as the cause of the non-quantitative agreement between the values of k_{total} calculated from the data and simulation.

the theory curve provided force and extension measurements independent of the $z_{bd} = 0$ and z_{trap} calibrations with large uncertainties. We performed simulations to quantify the accuracy of these estimations and the affect of the low bandwidth/ f_0 ratio. Based on these simulations, the power spectral analysis yielded the most accurate estimations of force and extension, with simulation input to output errors of $< 2\%$. This uncertainty neglects the anharmonicity of the trap that exists in the experiment but not in the simulation. The summary of the final force and extension estimates by the above calculations is given in two tables. Table 3.3 gives the force estimated by each of the three methods. Table 3.4 gives the final estimates for the force and extension by power spectral analysis, judged the most reliable method.

Table 3.3: Force estimation from data by equipartition (EQP), power spectral density (PSD) and autocorrelation (tau) methods.

Method	Low force (pN)	Intermediate force (pN)	High force (pN)
EQP	0.33	0.40	0.67
PSD	0.34	0.47	0.79
tau	0.33	0.37	0.62

Table 3.4: Final force and extension estimates via the power spectral density method, which yielded the most accurate results in simulations.

Relative force	Force (pN)	Extension (nm)
Low	0.34	54.5
Intermediate	0.47	60.4
High	0.79	67.8

3.6 DECREASED NOISE ON SHORT DNA TETHERS

As a demonstration of the improved signal to noise made possible by axial detection, we obtained axial position vs. time traces for 92 nm DNA tethers (Fig. 3.23 A). The position of the tethered bead was measured in all 3 axes while the sample was stabilized on a bead fixed

to the sample surface. The obtained position vs. time traces, smoothed to 5 Hz, are shown in Fig. 3.23 A. The integrated noise vs. time (Fig. 3.23 B) was obtained by integrating the power spectral density of the axial position vs. time traces shown in Fig. 3.23 A. The signal to noise obtained in these measurements demonstrates the power of axial trapping and detection. Because such short DNA can be used for tethering, the stiffness of the DNA is higher and the spatiotemporal resolution is improved, leading to an integrated noise of $<1\text{nm}$ over 0.03 - 3.2 Hz for a bead trapped at 0.47 pN.

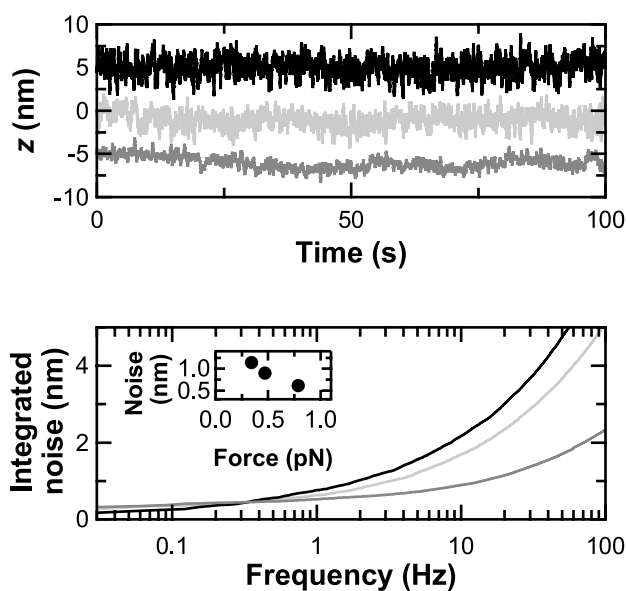


Figure 3.23: Stability of DNA extension measured on 92 nm tethers with stabilized, axial optical trap. (A) Axial position vs. time, smoothed to 5 Hz, for three different applied forces (black - 0.34 pN, light gray - 0.47 pN, dark gray - 0.79 pN). (B) Integrated noise vs. frequency for three different applied forces (same color representation as in A). (Inset) The integrated noise (0.03 - 2.5 Hz) vs. force. With our stabilization and axial-detection scheme, the integrated noise level is below 1 nm up to 3.2 Hz for a bead trapped at 0.47 pN (k_{trap} - 0.00528 pN/nm).

3.7 CONCLUSIONS

We have demonstrated an axial calibration and detection method that allows stable, precision measurements on very short DNA. Using a single laser and detection method and

stuck beads, we calibrated the axial displacement, stiffness, and height above the surface and developed a new method of estimating axial force and extension on very short DNA molecules. By axial trapping and detection, the trapping geometry is simplified, resulting in measurements made with no assumptions about the off-axis terms, less cross-talk, and improved signal-to-noise. The signal-to-noise is further improved by the ability afforded by axial trapping to make measurements on ultra-short DNA molecules, resulting in faster averaging of Brownian motion.

For the data in the following chapter, we used several relevant parts of the axial calibrations described in this chapter. We used the relative axial displacement calibration (without the oscillation corrections) to measure extension changes of DNA. We also used the axial trap stiffness calibration, combined with the described improved axial force and extension estimations to measure the absolute force and extension.

The other portions of the axial calibrations described in this chapter remain as useful 1st-order approximations. For our experiments, we used the described estimations of trap equilibrium and trap height to set the force and height during data acquisition. Later, during analysis, we corrected the force and height using the improved force and extension estimations.

Chapter 4

DIRECT MEASUREMENT OF HUMAN TBP BENDING DNA

4.1 INTRODUCTION

As described in Chapter 1, TBP binding DNA is one of the first steps in gene expression: recruitment of the transcription machinery necessary for making RNA. Upon binding, human TBP induces an $\sim 100^\circ$ bend in DNA. Using the techniques described in the previous chapters, we measured TBP dynamically bending DNA at the single molecule level in order to elucidate TBPs role in regulating transcription.

We report here direct observations of TBP-induced extension changes of DNA. The measurements were made using a novel biophysical assay including custom PEG surfaces, an actively stabilized optical trap, and an axial trapping geometry with a new method for axial force and extension determination (Fig. 4.1). Calibrated forces were applied to axially stretch the DNA and TBP-induced step-like DNA extension changes were measured. Hidden Markov modeling was applied for quantitative analysis of the extension change as well as rates of bending and unbending. Our results show that, under physiological KCl and MgCl₂ concentrations, human TBP dynamically bends and unbends TATA box DNA in step-like changes on time-scales of tens of seconds, which may imply a more dynamic role for TBP in transcription regulation than previously thought.

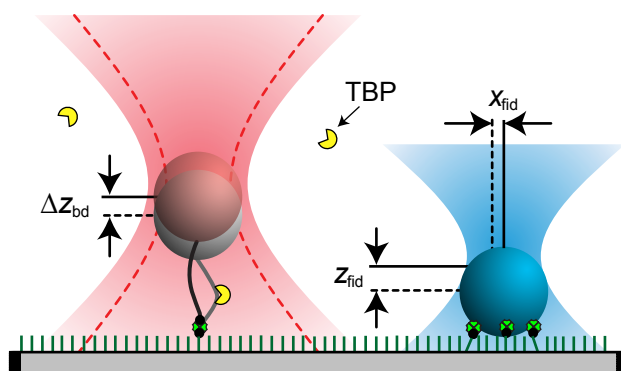


Figure 4.1: Final TBP assay. A cartoon depicts the final biophysical assay implemented to detect TBP bending DNA. On the right, sample stabilization is performed on a streptavidin-coated bead fixed to the surface by biotinylated-PEG. The position (e.g. x_{fid} , z_{fid}) is measured by a separate laser and actively stabilized using the piezo stage. On the left, TBP bending DNA is measured by axial detection of a DNA-tethered bead trapped directly above the tethering point. The bead is tethered by biotinylated DNA attached to the surface by streptavidin bound to covalently attached biotinylated-PEG molecule. When TBP bends the DNA, the bead is pulled down in the trap.

4.2 MATERIALS AND METHODS

The instrument and sample preparation were as described in Chapter 2. The actively stabilized optical-trapping microscope ensured the stability essential for measuring the small, infrequent events of TBP bending DNA. Beam steering and lateral stiffness were calibrated as described. Samples surfaces were coated with covalently attached PEG, which was essential for consistent, reproducible data acquisition. These surfaces incorporated mPEG (Laysan Bio) and 1-3% biotin PEG (Rapp Polymere) for specific attachment of DNA tethers to the surface, as well as for anchoring 860 nm dia. streptavidin beads to the surface to use as fiducials for sample stabilization. Tethers were 92 nm DNA, with biotin on one end to attach to biotin-PEG anchored streptavidin, and digoxigenin on the other end to attach to 330 nm dia. antidigoxigenin-modified beads. The short DNA was essential for single, TATA-specific extension changes, as was a carefully engineered DNA sequence with one or no TATA boxes and no other TATA-like sequences.

Experiments were exceptionally sensitive to buffer conditions. For all experiments, we used TBP buffer (10 mM Tris-Cl - pH 7.9, 10 mM Hepes - pH 7.9, 150 mM KCl, 1mM DTT, 0.5 mM MgCl₂, 0.2% tween-20, 0.4 mg/ml BSA). TBP buffer was actually a 1:1 combination of two different buffers, mixed just before experiments. One buffer was DB300 - 20 mM Tris-Cl, 300 mM KCl, 1 mM DTT, 0.8 mg/ml BSA, the other buffer was RM - 20 mM Hepes, 1mM MgCl₂, 1 mM DTT, 0.4% tween-20. The reason for mixing the buffers in this way was so that dilutions of TBP, which was in a buffer almost identical to the DB300, could be made in such a way as to not change the final concentrations of the buffer components. The storage buffer for TBP was DB100 (20 mM Tris - pH 7.9, 100 mM KCl, 1mM DTT, 20% glycerol, 50 μ g/ml BSA), the same as DB300 but with lower KCl, slightly higher BSA, and 20% glycerol. Transcription experiments have previously shown sensitivity to BSA solutions (personal communication from Jim Goodrich), and our TBP experiments also showed different behavior with different BSA solutions, failing when we used Sigma,

Bovine Albumin Fraction V A-3059. For this reason, we used the same BSA solution used in transcription experiments in the Goodrich lab (Roche BSA, Cat. No. 10 711 454 001). Sensitivity of TBP to other buffer conditions is discussed in the text.

Recombinant, human TBP was prepped as described in [27], and stored at -80°C , warmed in fingers and diluted into TBP buffer just before experiments. The TBP dilution was flowed into samples and data acquisition started ~ 3 min. afterwards. Leftover TBP was stored on ice and new TBP (from leftover on ice) was added after ~ 30 min. After 1 hour from removal from 80°C , any leftover TBP was discarded.

Data acquisition was as described in Chapter 2 and Chapter 3. Lateral sample and laser positioning and displacement calibrations were as described in Chapter 2, and axial positioning and calibrations were based on the description in Chapter 3. Axial displacement calibrations were 7th-order polynomial fits to Pralle reconstructions of the axial detection signal of each bead to be measured. Axial stiffness vs. power and vs. height were based on the PSD method estimates (see Chapter 2 and 3). The first approximation of axial trap equilibrium during acquisition was by the peak offset corresponding to the equilibrium voltage at the measurement height, as described in Chapter 3, and first approximation of trap height during acquisition was also determined by an offset from the voltage peak determined by the height dependent lateral drag measurement and stiffness dependent peak corrections. The final reported axial force and extension were calculated in analysis as described, based on the PSD of control 92-nm DNA-tether data, the height-dependent axial drag, and the theoretical $dF/dExt$ curve. Axial detection was essential for measurements on short DNA.

For data acquisition on each tether, we pre-tensioned the tether for screening and pre-centering over the tetherpoint. If the tether remained attached and had a (highly preliminary) persistence length measurement of $P > 7$ nm and contour length measurement $200 \text{ nm} < L < 265$ nm, we continued acquisition. We then positioned the sample and lasers and calibrated detection of x, y, z using automated LabVIEW. In detail, after the pretensioning, we set the sample height based on the axial detection peak, calibrated x, y detection sensi-

tivity of the trapped bead, moving the trap and stage simultaneously for calibration of the short DNA. We then centered over the tetherpoint via the stage and DNA centering curve, set the height again, and centered the fiducial laser over the fixed 860 nm bead by the PZT mirror. Finally, we performed the final x , y , z detection calibration of both detection lasers by moving the stage and the 1064 PZT mirror simultaneously.

For extension vs. time measurements, we acquired x , y , and z bead displacement vs. time for both the trapped bead and fiducial. We acquired 4000 data points/s, with 2 kHz antialiasing, stabilizing the sample at 100 Hz. In these measurements, changes in the axial trapped bead displacement were equivalent to changes in DNA extension to within an uncertainty estimate of relative bead position of 20% (based on the estimates in the previous chapter). For final display, we converted to absolute extension by adding the force-dependent extension calculated in the previous chapter to the bead position at that force minus the average bead position at that force.

Extension vs. time measurements were acquired with several variables. One variable was force: varying 0.3, 0.5, 0.8 pN, typically 100-300 s at each force. The force was set by changing the trap stiffness and moving the sample to change the bead displacement from the trap center to the desired displacement. The other two variables provided the main measurement vs. the controls: the main measurement was TBP + TATA box DNA. The controls were 1) TATA box DNA with no TBP present and 2) TBP + no TATA DNA.

For data analysis, extension changes, equivalent to axial displacement changes, were analyzed by three methods. The first method was a qualitative analysis of extension change events (see text below for details). The second method was an adapted hidden Markov modeling (HMM) algorithm developed for FRET data [34]. For this analysis we scaled displacement to between 0 and 1, and analyzed using the Hammy 4.0 GUI (available online at TJ Ha's website). The third method of analysis was a more sophisticated HMM algorithm, modified from the Hammy algorithm to introduce Fourier modes to correct for residual drift in the data.

4.3 TBP AND TATA-DEPENDENT EXTENSION CHANGES IN DNA

The first step in studying TBP bending of DNA was establishing TBP dependent extension changes of the DNA in a DNA tethering experiment. Our first dramatically TBP-dependent results on DNA tethers were achieved on a DNA construct containing 48 repeats of a consensus TATA box on 502 nm DNA. This construct was designed to maximize extension changes by TBP, creating compaction of the DNA that would be obvious by visual inspection of video microscopy, thus allowing faster screening of conditions. With this construct, we observed TBP dependent partial DNA compaction. As designed, this compaction was obvious by visual inspection of the CCD microscopy image of the DNA tethered beads, and it was also observed by stretching the DNA and observing discontinuities in the stretching curves. In addition, during extension vs. time data, we observed multiply-sized extension changes.

These experiments suggested that the DNA compaction did not occur from the construct sticking to the surface. In the stretching experiments, the centerpoint of repeated stretching experiments with discontinuities did not change within a few nm. The extension vs. time experiments also suggested the effects were not surface sticking because the lateral position of the bead in the laser was stable during the axial extension changes. However, without establishing TATA dependence, these experiments could not rule out sticking between DNA-TBP and the trapped bead. These experiments did demonstrate that applied load was able to disrupt some of the compaction, but often the compaction seemed to stabilize over time to become increasingly resistant to disruption.

We next set out to establish TATA box dependence. On similar length DNA to the multi-TATA construct but without engineered TATA boxes, we still observed similar partial DNA compaction. We decreased the DNA length to 285 nm and a sequence with no consensus TATA boxes and observed fewer discontinuities in stretching curves and fewer extension changes during extension vs. time data. We then further decreased the length of the DNA

tethers to 92 nm DNA. The 92 nm DNA improved both the TATA box dependence and also decreased Brownian noise due to the increased stiffness of the shorter DNA molecules, improving signal/noise.

Simultaneously to the experiments on different lengths of DNA, we performed experiments with varying KCl, MgCl₂, competitor GC DNA, and TBP concentration in attempts to find optimum conditions for further experiments. We also varied the DNA among four constructs: 92 nm DNA with one TATA box and no TATA box and ~300 nm DNA with one TATA box and no TATA box. Testing was generally preliminary in the sense that we only tested conditions on 2-6 samples, trying to quickly screen for the best conditions. The goals were to maximize interpretability and statistics, i.e. multiple consistently sized events over 100 s, with maximum specificity for the TATA box. Multiple events over 100 s would allow efficient gathering of statistically significant numbers of extension changes and dwell times in different states. Consistently sized events would suggest we had determined the base level extension change. Specificity to TATA leads to easier interpretability, because we would only be studying bending at one DNA sequence, reducing variables. The final optimized conditions were 150 mM KCl, 0.5 mM MgCl₂, no GC DNA, and 10-20 nM TBP. Interestingly, this KCl and MgCl₂ concentration mirror in vivo conditions [50].

4.3.1 Data reduction

Once DNA length, [TBP], [KCl], and [MgCl₂] were optimized, we obtained statistically significant amounts of data at identical conditions with controlled variables to more quantitatively show TBP and TATA box dependence. We obtained DNA extension vs. time data on 92 nm TATA DNA in the presence and absence of 20 nM TBP, and on 92 nm no TATA DNA in the presence and absence of 20 nM TBP, all under an applied load of 0.5 pN. In addition, we obtained 92 nm TATA \pm TBP under applied loads of 0.3 and 0.8 pN. Under these consistent conditions, we obtained extension vs. time traces on a total of 30 individual samples. At the tether level, we attempted to acquire data on some 300 tethers.

Of these 300, 70 stuck or detached before we could acquire >100 s of data. We chose 100 s as a cutoff in an attempt to ensure multiple events per typical TBP + TATA trace. Of the 230 remaining tethers, we cut 31 more due to poor persistence or contour length fit values. We cut 4 tethers due to qualitatively strange force vs. extension curves, one because of an unstable attachment to a fiducial, and 8 because they were acquired after TBP had been present in the sample without being refreshed for >30 min. We were left with 186 remaining tethers, 62% of the original 300.

Before performing further analysis on the extension vs. time data, the x , y , and z vs. time traces of both beads were visually inspected at both full bandwidth and 5 Hz smoothing and decimating. Regions of the traces representing different applied force were separated, resulting in 285 total traces. Further cuts were made here, at the trace level. Specifically regions of traces were cut if the tether detached (the axial bead displacement abruptly moved to ~ 0). Regions were also cut if the 0.2 Hz smoothed bead displacement moved $> \pm 10$ nm from the mean displacement. Regions were cut with spurious x or y tether and/or x , y , or z fiducial motion. Segments of traces adjacent to the removed regions were considered independent traces. If <100 s of data remained in a trace, the trace was discarded from the remaining analysis. These cuts resulted in discarding 34 full traces (12%) leaving a remaining 251 traces for further analysis.

From the initial visual inspection, distinct TBP and TATA dependent behavior was clear. Fig. 4.2 shows the typical observed behavior. Almost all traces in the absence of TBP showed a steady extension with a 1-2 nm noise level and some slow drift. Almost all no TATA + TBP data traces were similarly "quiet" with possibly a slight increase in events with abrupt extension changes. Almost all TATA + TBP traces showed multiple abrupt changes in DNA extension of ~ 3 nm. We interpret the dips as states where TBP is bound to and bending the DNA. To further quantify the TBP and TATA dependence, we performed a more rigorous visual inspection, counting events on the different types of traces.

On the final data set, examining the data at 5Hz smoothed/decimated, we observed

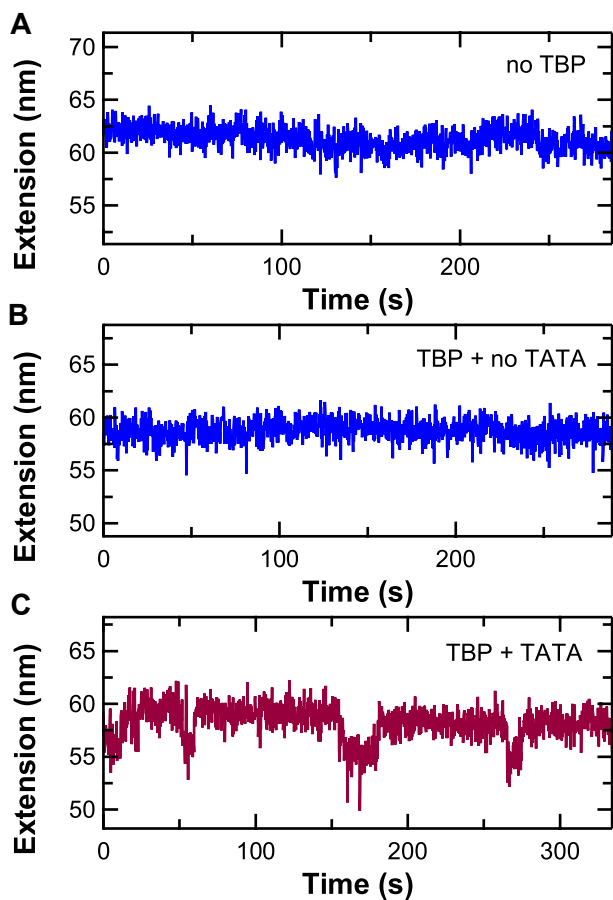


Figure 4.2: TBP and TATA dependent extension changes in DNA. DNA extension vs. time traces demonstrate clear TBP and TATA dependent extension changes. (A) DNA extension measured with no TBP present demonstrates typical noise levels for our experiment. (B) A trace on DNA containing no TATA box shows no step-like extension changes. (C) A trace on on DNA containing a consensus TATA box shows several step-like changes.

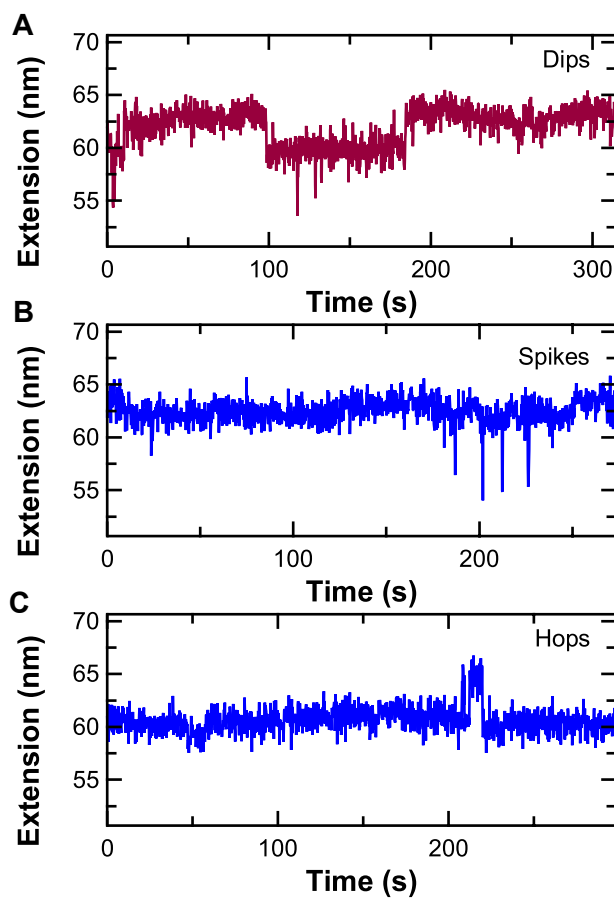


Figure 4.3: Common events in DNA extension vs. time traces. (A) Dips in extension from the state with the majority dwell time were the most common event on TBP+TATA traces. (B) Downward spikes in extension were the 2nd most common event. (C) Upward hops in extension from the state with the majority dwell time were more rare, but common enough to classify as an event.

three distinct classes of events: dips, spikes and hops. Fig. 4.3. We defined dips as >3 data points 2-5 nm below the extension with the majority dwell time. We defined spikes as 1-3 data points at >5 nm from main level of trace, and we defined hops as >3 data points 2+ nm above the extension with the majority dwell time. We then quantified numbers of each of these events by visual inspection for the data at 0.5 pN. For traces in the absence of TBP, on 51 traces we observed an average of 0.3 dips per trace, 0 spikes, and 0.04 hops/trace. The average trace length was ~ 200 s for each of these data sets. For no TATA + TBP traces, on 36 traces we observed an average of 0.3 dips/trace, 1.14 spikes/trace, and 0.2 hops/trace. For the TATA + TBP traces, on 88 traces we observed 3.8 dips/trace, 1.8 spikes/trace, and 0.2 hops/trace. While a more quantitative analysis than visual inspection could provide more precise results, the dramatic difference in the number of dips/trace firmly establishes the TBP and TATA dependence of these step-like DNA extension changes.

We also further analyzed the spike class of events in an attempt to elucidate their origin. Note that we observed 0 spikes in the no TBP data, 1.14/trace in the no TATA + TBP data, and 1.8/trace in the TATA + TBP data. The similar frequency of spikes in the no TATA + TBP and TATA + TBP traces suggests the spikes are TBP, but not TATA box, dependent. In addition, we quantified the presence of spikes for the TBP + TATA data at 0.3 and 0.8 pN. At 0.3 pN, we saw a dramatic increase in the frequency of spikes to an average of 5 spikes/trace. In contrast, at 0.8 pN, we saw only 0.49 spikes/trace. The spikes display a dramatic force dependence, qualitatively consistent with force increasing the energetic cost for larger DNA bends and decreasing the probability for longer range interactions under increased load. Finally, we quantified by visual inspection the incidence of spikes with origins stemming from dips vs. the upper level of traces that typically had the majority dwell time. In the No TATA data, spikes did not stem from dips. In the TATA + TBP data, across all forces, $> 83\%$ of spikes originated from dips, with a small force dependence (0.3 pN: 83%, 0.5 pN: 90%, 0.8 pN: 94%).

The origin of these spikes is currently unclear. They appear TBP dependent but not

entirely TATA dependent. They seem to vary in size of extension change, though determining the size of such fast events is difficult due to Brownian motion noise limits. The duration of the extension change associated with the spikes varies; examining the 4 kHz data leads to duration estimates of $\sim 0.1-0.5$ s. The spikes occur from dips far more frequently than not. Our interpretation that dips represent states where TBP is bound then suggests spikes may be an interaction of bound TBP with something else, another part of the DNA, another TBP bound to another part of the DNA, or possibly a brief interaction with the bead. The spikes are not consistent with interactions with the surface because no x or y motion accompanies them. One attractive hypothesis credits spikes to interactions with another TBP bound transiently to the DNA. Though untested, this hypothesis would have interesting implications in that the other bound TBP would have to be bound in an unbent, and probably highly unstable state.

4.4 EXTENSION CHANGES VS FORCE

For more quantitative analysis of extension changes and rates, we performed hidden Markov modeling analysis of our data traces. After initially applying the analysis to the 5 Hz smoothed data, evaluation of the extension change to standard deviation ratio ($\Delta Ext/\sigma$) showed the average $\Delta Ext/\sigma$ barely passed the threshold of 2 established in robustness measurements of the Hammy algorithm. For the low force data, $\Delta Ext/\sigma$ was <2 for over half the individual molecules. This evaluation led to re-analysis of the data at 1.67 Hz smoothing. Furthermore, we rejected traces that still had $\Delta Ext/\sigma$ ratios <2 at 1.67 Hz.

We fit the data to the simplest model, assuming 2 states, bent and unbent. We processed traces using the Hammy 4.0 GUI. We rejected data after processing if no transitions were present, if it was unclear which 2 states shared the majority dwell time, or if the Hammy algorithm could not fit the 2 states with the majority dwell times. We tested the influence of fitting to a 2-state model in the presence of the spikes. When fitting traces with many spikes, the difference in the measured extension change was $<10\%$ between fits including a

3rd state for spikes vs. fits with 2 states. The data and the HMM analysis show consistently sized extension changes with variable dwell times in the upper and lower extension states, see Fig. 4.4 for a trace and HMM fit at 0.5 pN. We interpret the lower state to represent bent DNA, and the upper state to represent unbent DNA. The 0.5 pN trace also shows long and short dwell times, with an expanded view to show excellent correspondence between short dwell times in the fit and the data. Traces and fits for 0.3 pN and 0.8 traces are shown in Fig. 4.5, showing similar extension changes and varying dwell times to the 0.5 pN data. Note also the spikes so frequently present in the 0.3 pN data.

The similarity of extension changes for the three forces is shown in Fig. 4.6. The histograms show distributions all peaked near 3 nm. Statistical analysis yields mean extension changes for the three forces all within statistical error of one another (2.8 ± 0.2 nm for 0.3 pN, 3.1 ± 0.1 nm for 0.5 pN, and 2.9 ± 0.2 for 0.8 pN). This lack of force dependence did not follow the trend expected from theoretical predictions of extension changes for kinked DNA under varying load, shown in Fig. 4.7 [9], though the magnitude of the extension changes is similar to the theoretical prediction.

4.5 KINETICS

HMM analysis yielded two separate measures for the transition rates between the two states. In one measure, the transition probabilities computed during the fit to each trace are converted into transition rates (rate = probability*data acquisition rate). Histograms of these transition rates are shown in Fig. 4.8. The statistics are low, but on inspection, the histograms do not appear to represent a normal distribution, especially the rates to unbend. In the Hammy analysis paper on which our HMM analysis is based, the transition rate histograms also appear to be non-normal distributions [34]. The authors convert to the natural log of the rates to yield normal distributions, then measure the mean and exponentiate it to obtain an expectation value of the rates. Conversion to natural logarithms of the transition rates shown here does not result in a normal distribution. Despite the skewed distributions,

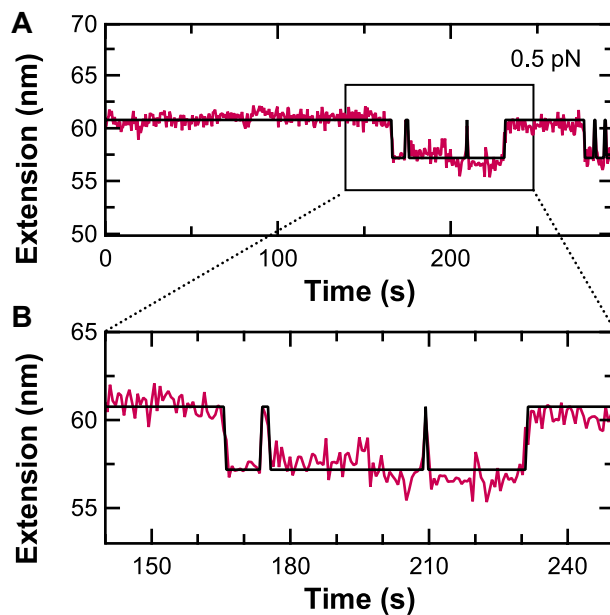


Figure 4.4: Extension changes show long and short dwell times. We analyzed the step-like extension changes in our data traces with a hidden Markov model (HMM). The fit is shown in black. (A) Long and short dwell times are evident in the data and well fit by the model. (B) A closer look at short dwell times and the HMM fit.

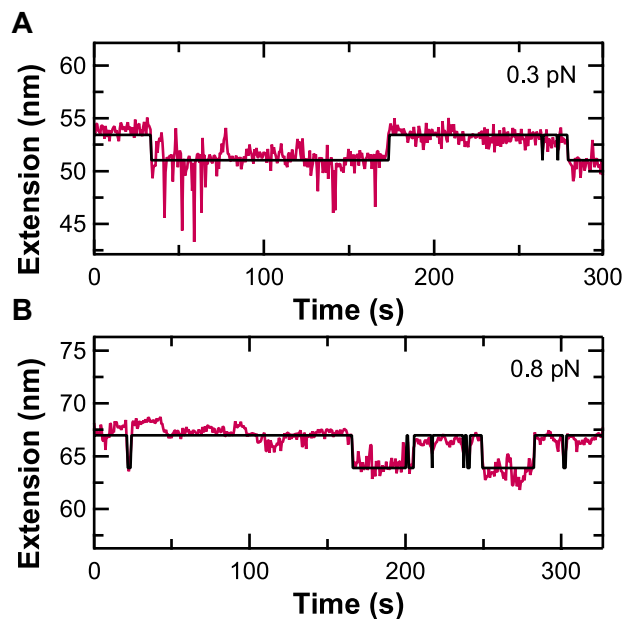


Figure 4.5: Exploring force dependence. Extension vs. time traces at 0.3 pN (A) and 0.8 pN (B) show TBP-dependent, step-like changes of similar size to extension changes for 0.5 pN traces.

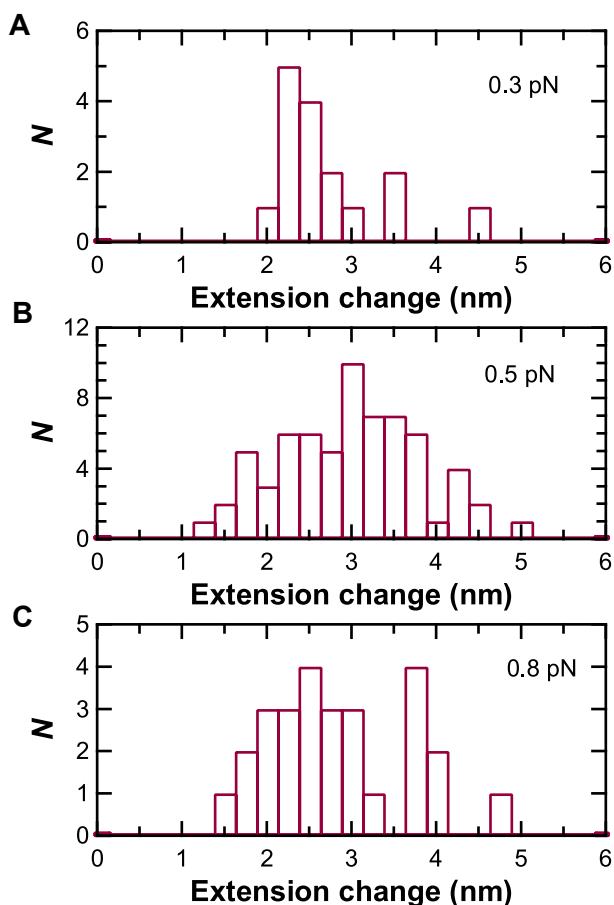


Figure 4.6: Histograms of extension changes for three forces. The extension changes from HMM analysis are histogrammed for three applied forces: 0.3 (A), 0.5 (B) and 0.8 (C) pN. The mean \pm std. error for the three forces respectively were 2.8 ± 0.2 nm, 3.1 ± 0.1 nm, and 2.9 ± 0.2 nm, all within statistical error of each other.

we report mean rates \pm standard errors in Table 4.1.

As the 2nd method of rate analysis yielded by HMM, we accumulated the dwell times in each state into dwell time histograms. A simple reaction should yield dwell time histograms well-fit by single exponentials, with the decay rate giving the rate of the process. For our model, we would expect fits to dwell times in the unbent state to yield bending rates, and fits to dwell times in the bent state to yield unbending rates. Fits to the dwell time histograms for our data were dependent on histogram binning and details of the fit. We optimized the binning and fitting using simulations (see next section) and determined 6 s time bins and

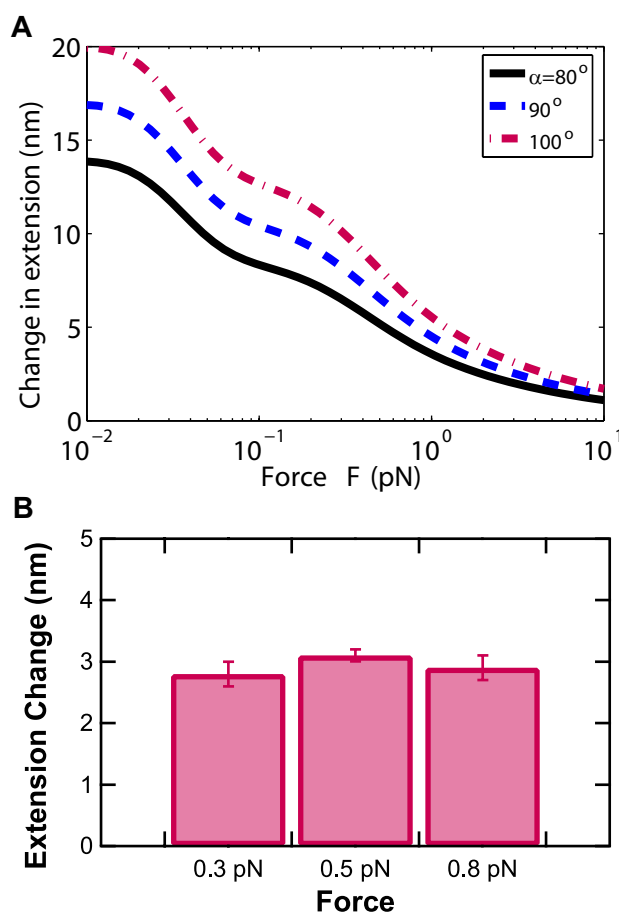


Figure 4.7: Force vs. extension change, theory and experiment. (A) A theoretical estimation of the expected extension change for TBP bending short DNA shows a strong force dependence of the extension change [9]. (Figure credit: figure by Prof. Meredith Betterton.) (B) The measured extension changes are similar in magnitude to the theoretical predictions, but do not follow the trend for different forces. Extension changes for each force (2.8 ± 0.2 nm for 0.3 pN, 3.1 ± 0.1 nm, for 0.5 pN and 2.9 ± 0.2 nm for 0.8 pN) are shown with the standard error.

linear fits to $\ln(N)$ provided the most accurate measure of rates for simulations based on the data values and a 2 state model with single exponentially distributed steps. Fig. 4.9 shows $\ln(N)$ and the linear fits for the bent and unbent dwell times, for each of the applied forces in our experiment. The obtained rates are listed in Table 4.2. The unbent state (bending rate) seems like a reasonable fit by this single exponential model. The bent state (unbending rate) is fit poorly by a single exponential, which also correlates with poor agreement between

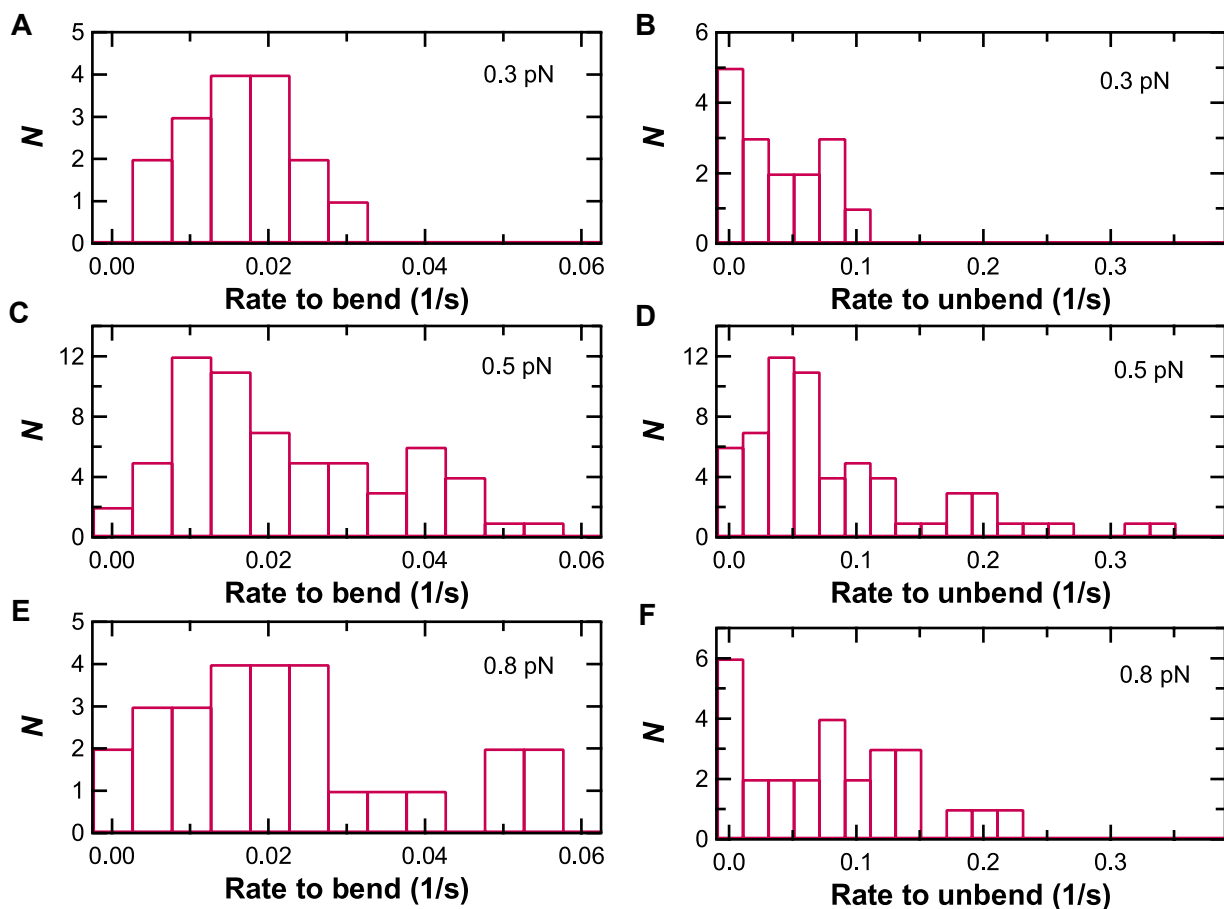


Figure 4.8: Transition rates calculated from transition probabilities. Transition probabilities for bending and unbending were calculated for each trace via HMM analysis. These probabilities were converted to transition rates (rate = probability * data acquisition rate), and histogrammed to show the distributions. Rates to bend are shown on the left; Rates to unbend on the right. Histograms of the rates are shown for three forces, 0.3 pN (A and B), 0.5 pN (C and D) and 0.8 pN (E and F).

Table 4.1: Transition rates from HMM transition probabilities.

Force	rate to bend (s^{-1})	rate to unbend (s^{-1})
0.3 pN	0.018 ± 0.002	0.048 ± 0.009
0.5 pN	0.029 ± 0.003	0.12 ± 0.02
0.8 pN	0.025 ± 0.003	0.09 ± 0.01

the unbending rates determined by transition rates vs. dwell time fits.

Table 4.2: Transition rates from dwell time fits.

Force	rate to bend (s^{-1})	rate to unbend (s^{-1})
0.3 pN	0.016 ± 0.003	0.018 ± 0.005
0.5 pN	0.03 ± 0.003	0.034 ± 0.006
0.8 pN	0.025 ± 0.003	0.016 ± 0.006

4.6 SIMULATIONS TO VALIDATE ANALYSIS

Before interpreting the values of these rates, we performed simulations to test the validity of our analysis methods on a simulation set with similar numbers and lengths of traces, similar extension changes, similar noise, and similar rates. We performed simulations of the sets of traces for each force, with the smallest set being the low force data with 17 traces. We then evaluated the percent difference between the input and output values for the extension change and the rates. The simulation for the smallest data set is shown in Fig. 4.10. The input, output and percent difference values are listed in Table 4.3. Though the percent difference values in the table show a maximum of 20%, repeated simulations actually showed percent differences in rates up to $\pm 50\%$ measured relative to the input rates. This large variation could actually be a factor of 2 times the measured rate, if the measured rate is 50% smaller than the input rate. The simulations suggest that even for an ideal system with the exact 2 state model we posit, with single exponential bending and unbending rates, the measured rates may only be estimates within 2x for our data sets.

4.7 DRIFT CORRECTING HIDDEN MARKOV ANALYSIS

Inspection of our long data traces reveals residual drift, despite active stabilization of our instrument. To quantify the impact of that drift on our TBP traces and potentially improve our measurements, a drift-correcting HMM algorithm was developed that incorporates Fourier modes to account for this drift (unpublished work by George Emanuel, Tatiana

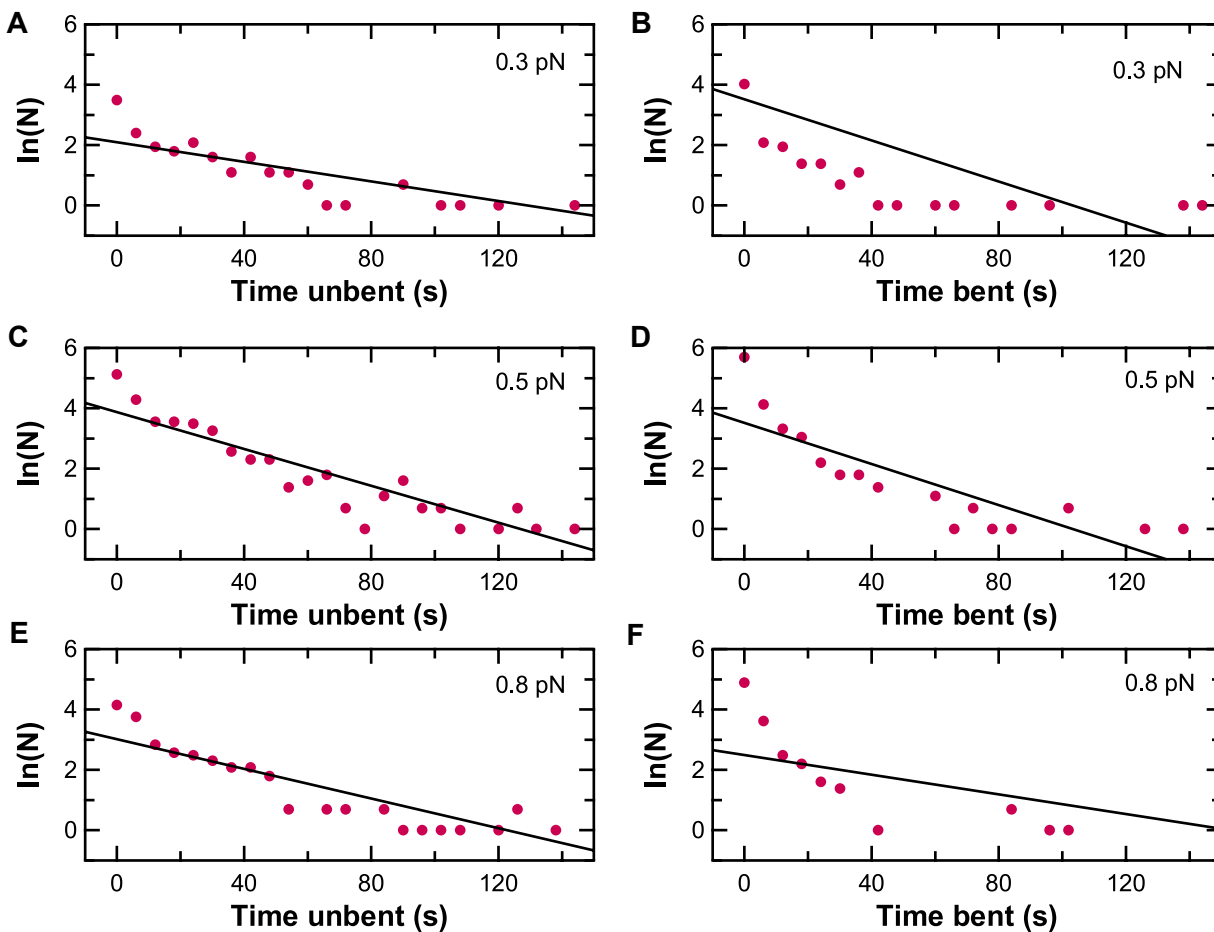


Figure 4.9: Dwell time histograms for three forces. Histograms of dwell times, plotted as $\ln(N)$, and linear fits to determine the bending rate and unbending rate at each force. The single-exponential rates are equivalent to the slopes, k , of the linear fits to $\ln(N)$ vs. time. The bending rate is the slope of the fit to the dwell times in the unbent state (left). The unbending rate is the slope of the fit to the dwell times in the bent state (right). Plots and fits are shown for three forces, 0.3 pN (A and B), 0.5 pN (C and D), and 0.8 pN (E and F). The unbending rates are poorly fit by the single-exponential model, indicating that a more complex model is needed to explain the data.

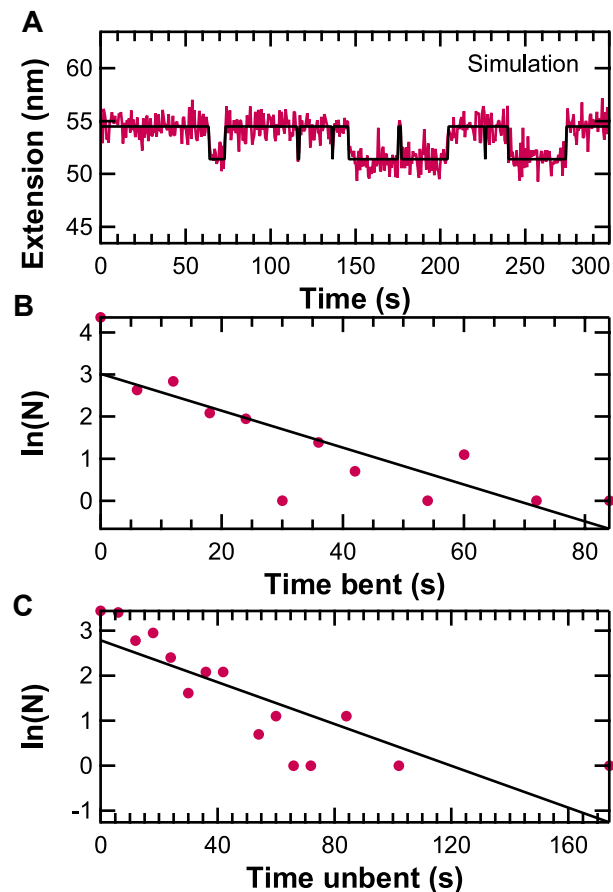


Figure 4.10: Simulations to verify analysis methods. Data analysis was performed with a hidden Markov modeling program. To verify this analysis, we simulated traces at a noise level ($\sigma = 1$ nm at 1.67 Hz) and trace length (~ 300 s) similar to our data set. We added exponentially distributed steps equal to the measured extension changes (~ 3 nm) with rates determined from the transition probabilities in our data analysis (bending rate = 0.02/s, unbending rate = 0.05/s). A simulation trace (A) and dwell time histograms of time spent in the bent (B) and unbent (C) states are shown. With the number of traces equivalent to our smallest data set ($N = 17$ at 0.3 pN) and single exponential fits to the dwell times, we recover our input values to within 20% (see table).

Table 4.3: TBP trace simulations.

	Input	Output	% difference
ΔExt	3	3.04	1.3
Rates from transition probabilities			
rate to bend	0.02	0.024	20
rate to unbend	0.05	0.052	4.9
Rates from dwell time analysis			
rate to bend	0.02	0.023	15
rate to unbend	0.05	0.044	-12

Kuriabova, and Meredith Betterton). As a first application of this method, analysis was performed, again with the simplest 2 state model, allowing for 1 Fourier mode to account for drift. A trace with obvious drift and the improved fit by the drift correcting algorithm is shown in Fig. 4.11. The entire data set was process with this algorithm, and extension changes and rates were quantified. Comparing those values and calculating percent differences demonstrates a $< 4\%$ difference in the measured extension change and differences in rates varying from -44% to $+ 56\%$. Though this rate variation is substantial, it is well within the 2x uncertainty suggested by simulations. Nonetheless, this drift-correcting HMM algorithm shows excellent potential for improving the precision of measurements on long traces with drift.

4.8 CONCLUSIONS

TBP bound to TATA box DNA recruits the transcription machinery to initiate site-specific transcription and is not ordinarily thought to be a transient complex. Nevertheless, our results indicate step-like dynamic bending of DNA by TBP on timescales of tens of seconds. These dynamics imply that TBP-TATA complexes must be caught and stabilized in a bent state during recruitment of the transcription machinery, in contrast to the textbook model of TBP stably bending TATA box DNA for hundreds of seconds and forming a virtually static site-specific scaffold for the transcription machinery. We anticipate that

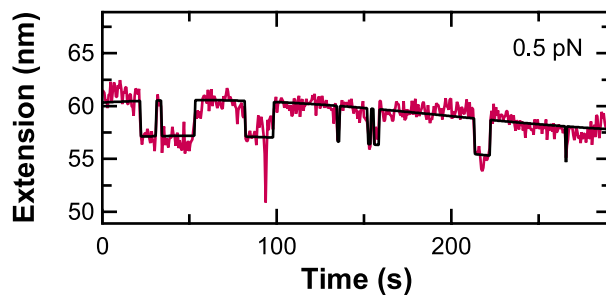


Figure 4.11: Drift correcting Hidden Markov Modelling analysis. Traces were analyzed with a more sophisticated HMM algorithm that accounted for steps and allowed Fourier modes to account for drift.

the developed biophysical assay will allow not only further characterizations of TBP-DNA interactions, but also direct measurements of the architectural changes that occur during assembly of the human transcription preinitiation complex.

Chapter 5

CONCLUSIONS AND FUTURE DIRECTIONS

5.1 CONCLUSIONS

One of the major results in this thesis is the development of a biophysical assay capable of performing stable, precision optical trapping measurements on DNA-binding proteins interacting with very short DNA molecules. The key developments for this assay included an actively stabilized optical trapping instrument (based on previous work [10, 11, 12]), a novel axial detection technique for measuring changes in DNA extension and determining DNA extension and force, and custom PEG surfaces to prevent non-specific adhesion of proteins to the sample surfaces. These innovations allowed measurements to be performed on short DNA molecules (<100 nm), which not only expands the range of biological phenomenon that can potentially be studied by optical trapping, but also, due to the increase in DNA stiffness for shorter molecules, improves the spatio-temporal resolution of these measurements.

The techniques described in this thesis allowed direct, single-molecule measurements of human TBP bending DNA. These measurements found a step-like TBP-induced DNA extension change of ~ 3 nm, constant over a force range of 0.3-0.8 pN. The magnitude of the extension change was similar to the theoretical predictions at these forces [9] for the 100° bend expected for TBP, but smaller by a factor of $\sim 2-4$ x, and without the predicted force dependence. Over this force range the measurements showed TBP bending and unbending DNA on a timescale of tens of seconds. The measured unbending rates were much faster than dissociation rates in the literature measured at lower KCl concentrations, but similar

to a more recently published measurement of TBP dissociation rates under a similar, more physiological KCl concentration. The faster dissociation rates observed at more physiological monovalent salt concentrations could have interesting implications for models describing the role of TBP in transcription initiation and regulation.

5.2 FUTURE DIRECTIONS

5.2.1 Technique and instrumentation improvements

The axial measurement techniques described in this thesis were adept at measuring axial trap stiffness and DNA extension changes with low uncertainty (<20%), as well as estimating an average applied force and DNA extension. However, these techniques fell short when attempts were made at obtaining a simple force vs. extension curve on DNA and at dynamically measuring force and absolute bead displacement from trap equilibrium on individual molecules. This failure was mostly credited to an inability to determine the position of the axial trap equilibrium with accuracy. The biggest impediment to determining the trap equilibrium position was the voltage oscillations that occur in the detection signal with changes in depth from the sample surface. A technique for removing these voltage oscillations from the detection signal has shown promise (personal communication from Allison Churnside), and this oscillation removal technique could dramatically decrease the uncertainty in measurements of the axial trap equilibrium position. With this improvement, the axial measurement technique could potentially measure not only DNA extension changes and average force and extension, but also dynamically measure the force, DNA extension, and absolute bead displacement from trap equilibrium for individual molecules with a precision similar to lateral measurement techniques.

5.2.2 Exploring TBP-induced spikes in DNA extension

During the measurements of TBP bending DNA, larger, faster extension decreases also occurred, appearing in the time-averaged data as downward spikes in extension. The spikes were a TBP-dependent phenomenon but not completely dependent on the presence of a TATA box. The origin of these spikes is currently unclear, but the observation that a majority of spikes originated from the bent state ($\sim 90\%$) strongly suggests they originate from a bound TBP interacting with another region of the DNA or possibly with the bead. Further analysis of the existing data could examine the size and duration of these spikes, determining a range of interaction zones, and/or determining the likelihood that spikes originate from an interaction with the bead. If the TBP-induced spikes in extension prove an interesting phenomenon (i.e. not likely resulting from an interaction with the bead), future experiments could explore the origin of this interaction.

Part of the interest in this spike phenomenon is based on the hypothesis that the spikes may originate from an interaction with the N-terminal tail of TBP. The N-terminal tail of TBP is made up of a varying number of glutamine repeats, typically between 29 and 42 [2]. Polyglutamine tracts, like those in the tail of TBP, are associated with protein aggregation [51], which fuels the hypothesis that the TBP tail may be the source of the interaction causing these TBP-dependent spikes in DNA extension. Further fueling this hypothesis is the extreme TBP concentration dependence observed during data acquired while optimizing conditions for our experiments. When the TBP concentration was increased by as little as 10%, the observed behavior changed dramatically. Rather than observing step-like extension changes, we observed highly variable extension changes, with increasing stability over time, resulting in apparently compacted DNA after only a few minutes. Such dramatic concentration dependence is often associated with cooperative processes, which supports a hypothesis that larger extension changes may be caused by multiple TBP molecules binding to the DNA and interacting with one another. Driving home the relevance of studying interactions

caused by the tail of TBP, expansion of the number of glutamine repeats in the human TBP tail to >42 causes nuclear aggregates of TBP in cells and the neurodegenerative disease spinocerebellar ataxia type 17 (SCA17) [52]. The possible relevance of these interactions to a disease-causing mechanism solidifies the potential importance of understanding these interactions.

To elucidate the origin of the spikes, two experiments may prove useful. If the interactions are between TBP and other regions of the DNA, introducing non-specific competitor GC DNA could decrease the frequency of the spikes. Addressing the question from another angle, if the interactions are caused by interactions with the TBP tail, performing experiments with truncated TBP containing only the C-terminal DNA-binding region should eliminate the spikes. Additionally, if the extremely concentration dependent DNA compaction originates from interactions with the N-terminal tail, the truncated TBP would not cause this DNA compaction. If proven true, an added benefit would be the ability to measure TBP-DNA interactions at an increased TBP concentration, which should also accelerate the binding rate, allowing faster and concentration-dependent measurements to be made of TBP bending DNA. These types of measurements are currently impeded by the compaction that occurs when the concentration of TBP is increased.

5.2.3 Angle vs. stability changes for bending of non-consensus TATA boxes

TBP preferentially binds TATA-box sequences of DNA, but to function in promoters without a TATA box, TBP must also bind non-TATA DNA sequences. This requirement begs the question of what differences may exist between TBP binding TATA box vs. non-TATA box DNA, and how these differences may influence the regulation of genes with TATA promoters vs. genes without TATA promoters. FRET studies have begun to answer these questions [53, 54, 55], finding a significant decrease in apparent bend angle for non-TATA box DNA sequences. These studies also found a broadening of the distribution of bend angles for non-TATA sequences, indicating a more heterogenous population of bending angles. Thus

the question remains unanswered whether the apparent bend angle decrease was caused by an actual decrease in bend angle for the individual molecules, vs. a decrease in the stability of the bending, which would be time-averaged over the population of molecules in these measurements. Our single-molecule optical trapping experiments, performed on DNA with non-consensus TATA box sequences, could potentially differentiate between these two possibilities, either showing a decreased bend angle for individual molecules, a decrease in stability of bending, or even a combination of the two.

5.2.4 Geometry and stability changes with additional PIC proteins

TBP bending of DNA is but one of the conformational changes of DNA thought to occur during transcription initiation. FRET studies have shown bending angles are different for TBP-DNA complexes alone vs. TBP-DNA complexes containing TFIIA [5]. Crosslinking and electron microscopy studies have suggested wrapping of the DNA around members of the preinitiation complex (PIC) [8, 56, 57]. In addition, TBP can bind DNA both alone and as a subunit of the general transcription factor TFIID, and the structure of TFIID-DNA complexes remains an open question [58]. This structural question, once answered, could greatly influence the interpretation of the role of bending and DNA architecture in transcription initiation and regulation.

The assay established in this thesis could potentially elucidate how the geometry and stability of protein-DNA complexes change as different transcription factors are introduced. The optical trapping experiments described here studied dynamic bending of DNA by TBP on timescales of tens of seconds, an ideal timescale for these extension vs. time measurements. Adding additional transcription factors often increases the stability of the protein-DNA complexes, which could create complexes with dynamics too slow to study reasonably by simply measuring extension vs. time. However, with an optical trap, the force can be increased, which should increase the dissociation/unbending rates of the DNA-protein complexes. Preliminary studies we performed showed increasing the force dynamically to 5-20 pN may even

cause abrupt unwrapping of DNA-PIC complexes, and these complexes may rewrap as the force on the DNA is relaxed.

These type of single-molecule optical trapping studies of various complexes of DNA with PIC components could not only measure the changing geometry and stability of these complexes, but potentially even observe the order these complexes may assemble on the DNA. This order of assembly remains another open question in transcription, with contrasting models, one suggesting an ordered assembly of proteins on the DNA vs. another suggesting assembly of proteins in solution before binding to the DNA [2]. Elucidating the architecture of PIC complexes and the order of assembly of these complexes is an exciting possibility that could have an impact on our understanding of transcription initiation and regulation of gene expression.

Bibliography

- [1] J. M. Berg, J. L. Tymoczko, and L. Stryer, *Biochemistry*, 5th ed. (W. H. Freeman and Company, New York, 2002).
- [2] M. C. Thomas and C. M. Chiang, The general transcription machinery and general cofactors, *Crit Rev Biochem Mol Biol* **41**, 105 (2006).
- [3] D. B. Nikolov, H. Chen, E. D. Halay, A. Hoffman, R. G. Roeder, and S. K. Burley, Crystal structure of a human TATA box-binding protein/TATA element complex, *Proc Natl Acad Sci U S A* **93**, 4862 (1996).
- [4] K. M. Masters, K. M. Parkhurst, M. A. Daugherty, and L. J. Parkhurst, Native human TATA-binding protein simultaneously binds and bends promoter DNA without a slow isomerization step or TFIIB requirement, *J Biol Chem* **278**, 31685 (2003).
- [5] A. R. Hieb, W. A. Halsey, M. D. Betterton, T. T. Perkins, J. F. Kugel, and J. A. Goodrich, TFIIA changes the conformation of the DNA in TBP/TATA complexes and increases their kinetic stability, *J Mol Biol* **372**, 619 (2007).
- [6] J. E. Whittington, R. F. Delgadillo, T. J. Attebury, L. K. Parkhurst, M. A. Daugherty, and L. J. Parkhurst, TATA-binding protein recognition and bending of a consensus promoter are protein species dependent, *Biochemistry* **47**, 7264 (2008).
- [7] S. F. Tolic-Norrelykke, M. B. Rasmussen, F. S. Pavone, K. Berg-Sorensen, and L. B. Oddershede, Stepwise bending of DNA by a single TATA-box binding protein, *Biophys J* **90**, 3694 (2006).
- [8] B. Coulombe and Z. F. Burton, DNA bending and wrapping around RNA polymerase: a "revolutionary" model describing transcriptional mechanisms, *Microbiol Mol Biol Rev* **63**, 457 (1999).
- [9] J. Y. Li, P. C. Nelson, and M. D. Betterton, Entropic elasticity of DNA with a permanent kink, *Macromolecules* **39**, 8816 (2006).
- [10] L. Nugent-Glandorf and T. T. Perkins, Measuring 0.1-nm motion in 1 ms in an optical microscope with differential back-focal-plane detection, *Opt. Lett.* **29**, 2611 (2004).

- [11] A. R. Carter, G. M. King, T. A. Ulrich, W. Halsey, D. Alchenberger, and T. T. Perkins, Stabilization of an optical microscope to 0.1 nm in three dimensions, *Appl. Opt.* **46**, 421 (2007).
- [12] A. R. Carter, Y. Seol, and T. T. Perkins, Precision Surface-Coupled Optical-Trapping Assays with 1 Base-Pair Resolution, *Biophys. J.* **96**, 2926 (2009).
- [13] K. C. Neuman and S. M. Block, Optical trapping, *Rev. Sci. Instrum.* **75**, 2787 (2004).
- [14] A. R. Carter, A Precision Optical Trapping Assay: Measuring the Conformational Dynamics of Single E. Coli RecBCD Helicases, Ph.D. thesis, 2008.
- [15] J. Kobayashi, Y. Izumi, M. Kumakura, and Y. Takahashi, Stable all-optical formation of Bose-Einstein condensate using pointing-stabilized optical trapping beams, *Appl. Phys. B* **83**, 21 (2006).
- [16] K. Visscher, S. P. Gross, and S. M. Block, Construction of multiple-beam optical traps with nanometer-resolution position sensing, *IEEE J. Sel. Top. Quant. Electr.* **2**, 1066 (1996).
- [17] F. Gittes and C. F. Schmidt, Interference model for back-focal-plane displacement detection in optical tweezers, *Opt. Lett.* **23**, 7 (1998).
- [18] A. Pralle, M. Prummer, E. L. Florin, E. H. K. Stelzer, and J. K. H. Horber, Three-dimensional high-resolution particle tracking for optical tweezers by forward scattered light, *Microsc. Res. Tech.* **44**, 378 (1999).
- [19] K. C. Neuman, E. A. Abbondanzieri, and S. M. Block, Measurement of the effective focal shift in an optical trap, *Opt Lett* **30**, 1318 (2005).
- [20] Y. Seol, A. E. Carpenter, and T. T. Perkins, Gold nanoparticles: enhanced optical trapping and sensitivity coupled with significant heating, *Opt. Lett.* **31**, 2429 (2006).
- [21] M. D. Wang, H. Yin, R. Landick, J. Gelles, and S. M. Block, Stretching DNA with optical tweezers, *Biophys. J.* **72**, 1335 (1997).
- [22] C. Bouchiat, M. D. Wang, J. Allemand, T. Strick, S. M. Block, and V. Croquette, Estimating the persistence length of a worm-like chain molecule from force-extension measurements, *Biophys. J.* **76**, 409 (1999).
- [23] C. Bustamante, J. F. Marko, E. D. Siggia, and S. B. Smith, Entropic elasticity of l-DNA, *Science* **265**, 1599 (1994).
- [24] J. F. Marko and E. D. Siggia, Stretching of DNA, *Macromol.* **28**, 8759 (1995).
- [25] Y. Seol, J. Li, P. C. Nelson, T. T. Perkins, and M. D. Betterton, Elasticity of Short DNA Molecules: Theory and Experiment for Contour Lengths of 0.6-7 μ m, *Biophys. J.* **93**, 4360 (2007).

- [26] T. Ha, Single-molecule fluorescence resonance energy transfer, *Methods* **25**, 78 (2001).
- [27] S. K. Galasinski, T. N. Lively, A. Grebe de Barron, and J. Goodrich, Acetyl-CoA stimulates RNA polymerase II transcription and promoter binding by TFIID in the absence of histones, *Mol. Cell. Biol.* **20**, 1923 (2000).
- [28] H. J. Metcalf and P. van der Straten, *Laser Cooling and Trapping* (Springer-Verlag, New York, 1999).
- [29] A. Rohrbach and E. H. K. Stelzer, Three-dimensional position detection of optically trapped dielectric particles, *Journal of Applied Physics* **91**, 5474 (2002).
- [30] E. Hecht, *Optics*, 4th ed. ed. (Addison Wesley, San Francisco, 2002).
- [31] K. Svoboda and S. M. Block, Biological Applications of Optical Forces, *Annu. Rev. Biophys. Biomol. Struct.* **23**, 247 (1994).
- [32] A. Rohrbach and E. H. Stelzer, Optical trapping of dielectric particles in arbitrary fields, *J Opt Soc Am A Opt Image Sci Vis* **18**, 839 (2001).
- [33] N. B. Viana, M. S. Rocha, O. N. Mesquita, A. Mazolli, P. A. Maia Neto, and H. M. Nussenzveig, Towards absolute calibration of optical tweezers, *Phys Rev E Stat Nonlin Soft Matter Phys* **75**, 021914 (2007).
- [34] S. A. McKinney, C. Joo, and T. Ha, Analysis of single-molecule FRET trajectories using hidden Markov modeling, *Biophys J* **91**, 1941 (2006).
- [35] M. J. Lang, C. L. Asbury, J. W. Shaevitz, and S. M. Block, An automated two-dimensional optical force clamp for single molecule studies, *Biophys. J.* **83**, 491 (2002).
- [36] L. P. Ghislain, N. A. Switz, and W. W. Webb, Measurement of small forces using an optical trap, *Review of Scientific Instruments* **65**, 2762 (1994).
- [37] I. M. Peters, B. G. d. Grooth, J. M. Schins, C. G. Figdor, and J. Greve, Three dimensional single-particle tracking with nanometer resolution, *Review of Scientific Instruments* **69**, 2762 (1998).
- [38] H. P. Kao and A. S. Verkman, Tracking of single fluorescent particles in three dimensions: use of cylindrical optics to encode particle position, *Biophys J* **67**, 1291 (1994).
- [39] E.-L. Florin, J. K. H. Horber, and E. H. K. Stelzer, High-resolution axial and lateral position sensing using two-photon excitation of fluorophores by a continuous-wave Nd:YAG laser, *Applied Physics Letters* **69**, 446 (1996).
- [40] K. Sasaki, M. Tsukima, and H. Masuhara, Three-dimensional potential analysis of radiation pressure exerted on a single microparticle, *Applied Physics Letters* **71**, 37 (1997).
- [41] A. R. Clapp, A. G. Ruta, and R. B. Dickinson, Three-dimensional optical trapping and evanescent wave light scattering for direct measurement of long range forces between a colloidal particle and a surface, *Review of Scientific Instruments* **70**, 2627 (1999).

- [42] C. Gosse and V. Croquette, Magnetic tweezers: micromanipulation and force measurement at the molecular level, *Biophys. J.* **82**, 3314 (2002).
- [43] A. Rohrbach, H. Kress, and E. H. Stelzer, Three-dimensional tracking of small spheres in focused laser beams: influence of the detection angular aperture, *Opt Lett* **28**, 411 (2003).
- [44] J. K. Dreyer, K. Berg-Sorensen, and L. Oddershede, Improved axial position detection in optical tweezers measurements, *Applied Optics* **43**, 1991 (2004).
- [45] K. C. Neuman, E. A. Abbondanzieri, R. Landick, J. Gelles, and S. M. Block, Ubiquitous transcriptional pausing is independent of RNA polymerase backtracking, *Cell* **115**, 437 (2003).
- [46] C. Deufel and M. D. Wang, Detection of forces and displacements along the axial direction in an optical trap, *Biophys. J.* **90**, 657 (2006).
- [47] E. Schaffer, S. F. Norrelykke, and J. Howard, Surface forces and drag coefficients of microspheres near a plane surface measured with optical tweezers, *Langmuir* **23**, 3654 (2007).
- [48] Y. F. Chen, G. A. Blab, and J. C. Meiners, Stretching submicron biomolecules with constant-force axial optical tweezers, *Biophys J* **96**, 4701 (2009).
- [49] J. Gelles, B. J. Schnapp, and M. P. Sheetz, Tracking kinesin-driven movements with nanometre-scale precision, *Nature* **331**, 450 (1988).
- [50] B. Alberts, A. Johnson, J. Lewis, M. Raff, K. Roberts, and P. Walter, *Molecular Biology of the Cell*, fourth ed. (Garland Science, New York, 2002).
- [51] K. Stott, J. M. Blackburn, P. J. Butler, and M. Perutz, Incorporation of glutamine repeats makes protein oligomerize: implications for neurodegenerative diseases, *Proc Natl Acad Sci U S A* **92**, 6509 (1995).
- [52] M. J. Friedman, A. G. Shah, Z. H. Fang, E. G. Ward, S. T. Warren, S. Li, and X. J. Li, Polyglutamine domain modulates the TBP-TFIIB interaction: implications for its normal function and neurodegeneration, *Nat Neurosci* **10**, 1519 (2007).
- [53] J. Wu, K. M. Parkhurst, R. M. Powell, and L. J. Parkhurst, DNA sequence-dependent differences in TATA-binding protein-induced DNA bending in solution are highly sensitive to osmolytes, *J Biol Chem* **276**, 14623 (2001).
- [54] J. Wu, K. M. Parkhurst, R. M. Powell, M. Brenowitz, and L. J. Parkhurst, DNA bends in TATA-binding protein-TATA complexes in solution are DNA sequence-dependent, *J Biol Chem* **276**, 14614 (2001).
- [55] R. F. Delgadillo, J. E. Whittington, L. K. Parkhurst, and L. J. Parkhurst, The TATA-binding protein core domain in solution variably bends TATA sequences via a three-step binding mechanism, *Biochemistry* **48**, 1801 (2009).

- [56] B. Coulombe, DNA wrapping in transcription initiation by RNA polymerase II, *Biochem Cell Biol* **77**, 257 (1999).
- [57] T. K. Kim, T. Lagrange, Y. H. Wang, J. D. Griffith, D. Reinberg, and R. H. Ebricht, Trajectory of DNA in the RNA polymerase II transcription preinitiation complex, *Proc Natl Acad Sci U S A* **94**, 12268 (1997).
- [58] L. Tora and H. T. Timmers, The TATA box regulates TATA-binding protein (TBP) dynamics in vivo, *Trends Biochem Sci* **35**, 309 .